Quantum Electronic Transport in Mesoscopic Graphene Devices

Quantum Electronic Transport in Mesoscopic Graphene Devices

A dissertation presented

by

Monica Theresa Allen

to

The Department of Physics

in partial fulfillment of the requirements

for the degree of

Doctor of Philosophy

in the subject of

Physics

Harvard University

Cambridge, Massachusetts

April 2016

Dissertation Advisor:

Professor Amir Yacoby

Author:

Monica Theresa Allen

Quantum Electronic Transport in Mesoscopic Graphene Devices

Abstract

Graphene provides a rich platform for the study of interaction-induced broken symmetry states due to the presence of spin and sublattice symmetries that can be controllably broken with external electric and magnetic fields. At high magnetic fields and low temperatures, where quantum effects dominate, we map out the phase diagram of broken symmetry quantum Hall states in suspended bilayer graphene. Application of a perpendicular electric field breaks the sublattice (or layer) symmetry, allowing identification of distinct layer-polarized and canted antiferromagnetic $\nu = 0$ states. At low fields, a new spontaneous broken-symmetry state emerges, which we explore using transport measurements.

The large energy gaps associated with the $\nu = 0$ state and electric field induced insulating states in bilayer graphene offer an opportunity for tunable bandgap engineering. We use local electrostatic gating to create quantum confined devices in graphene, including quantum point contacts and gate-defined quantum dots.

The final part of this thesis focuses on proximity induced superconductivity in graphene Josephson junctions. We directly visualize current flow in a graphene Josephson junction using superconducting interferometry. The key to our approach involves reconstruction of the real-space current density from magnetic interference using Fourier methods. We observe that current is confined to the crystal boundaries near the Dirac point and that edge and bulk currents coexist at higher Fermi energies. These results are consistent with the existence of "fiber-optic" edge modes at the Dirac point, which we model theoret-

ically. Our techniques also open the door to fast spatial imaging of current distributions along more complicated networks of domains in larger crystals.

Contents

List of Figures

List of Tables

Citations to Previously Published Work

Large portions of Chapter 2 have appeared in the following paper:

> "Broken-symmetry states in doubly gated suspended bilayer graphene". R.T. Weitz, M.T. Allen, B.E. Feldman, J. Martin, and A. Yacoby. Science **330**, 812-816 (2010)

Chapter 3 appears in its entirety as

> "Gate-defined quantum confinement in suspended bilayer graphene." M. T. Allen, J. Martin, A. Yacoby. Nature Communications 3:934 (2012).

The material covered in Chapter 4 appears in

> "Spatially resolved edge currents and guided-wave electronic states in graphene." M. T. Allen, O. Shtanko, I. C. Fulga, A. R. Akhmerov, K. Watanabe, T. Taniguchi, P. Jarillo-Herrero, L. S. Levitov, and A. Yacoby. Nature Physics, **12**, 128-133 (2016).

The material covered in Chapter 5 appears in

> "Visualization of phase-coherent electron interference in a ballistic graphene Josephson junction." M. T. Allen, O. Shtanko, I. C. Fulga, J. Wang, D. Nurgaliev, K. Watanabe, T. Taniguchi, A. R. Akhmerov, P. Jarillo-Herrero, L. S. Levitov, and A. Yacoby. arXiv:1506.06734 (2015).

Electronic preprints are available on the Internet at the following URL:

> `http://arXiv.org`

Acknowledgments

First, I would like to thank Amir Yacoby for his scientific guidance, stimulating discussions, and for giving me the freedom and resources to explore of a range of new phenomena in graphene. In addition to having a strong theoretical background, Amir is a creative experimentalist who provided the inspiration behind many of the ideas explored in this thesis. I would also like to thank my thesis committee, Robert Westervelt and Ronald Walsworth, for their advice, support, and interest in my progress.

Leonid Levitov deserves special recognition for his insights on our work on broken symmetry quantum Hall states and theoretical contributions on the induced superconductivity experiments. I am also grateful to Pablo Jarillo-Herrero and Philip Kim and their students for stimulating discussions, particularly regarding hBN device fabrication.

I would like to thank my research collaborators, including Jens Martin, who mentored me as an undergraduate and during the early stages of my PhD, as well as Thomas Weitz and Ben Feldman, who worked closely with me on the investigation of correlated electron states in suspended bilayer graphene devices. I had the privilege of working directly with several theory students and postdocs, including Oles Shtanko, Ion Cosma Fulga, Anton Akhmerov, and Daniyar Nurgaliev. I also appreciate fruitful discussions with Professors Bertrand Halperin, Allan MacDonald, Jay Deep Sau, Dima Abanin, and Rahul Nandkishore.

Within the Yacoby lab, I benefited from the technical expertise of Vivek Venkatachalam, Hendrik Bluhm, and Oliver Dial. I'd also like to thank postdocs Marc Warner, Francesco Casola, Patrick Maletinksy, Toeno van der Sar, Kristaan de Greve, and Lan Luan, as well as graduate students Andrei Levin, Gilad Barak, Gilad Ben-Shach, Sungkun Hong, Tony Zhou, Mike Grinolds, Sandra Foletti, Michael Schulman, Sean Hart, Hechen Ren, Shannon Harvey, Yuliya Dovgenko, Di Wei, Lucas Orona, and Michael Kosowsky. Thanks to Jimmy Williams, Hugh Churchill, Patrick Herring, Yongjie Hu, and Ferdinand

Keummeth from the Marcus lab. I also appreciate discussions with the Kim lab and Jarillo-Herrero lab, especially Patrick Maher, Carlos Forsythe, Xiaomeng Liu, Hadar Steinberg, Javier Sanchez-Yamagishi, Valla Fatemi, Joel Wang, and Britt Baugher. I would also like to acknowledge the important contributions of our boron nitride crystal growers, K. Watanabi and T. Taniguchi.

I extend special thanks to Giorgio Frossati, for his technical expertise and patience when troubleshooting issues with the Frossati dilution refrigerator remotely from the Netherlands. Many thanks to the attentive staff of the Harvard Center for Nanoscale Systems, especially Jiangdong Deng, Yuan Lu, Ling Xie, and Jason Tresback. I am grateful to our administrative staff, including Yacoby lab administrators Carolyn Moore and Hannah Belcher, as well as the physics department graduate administrator Lisa Cacciabaudo.

During graduate school I was generously supported by the Purcell Fellowship at Harvard and the DOE Office of Science Graduate Fellowship (DOE-SCGF).

I'd like to thank everyone who made my graduate school experience more pleasant. I'm grateful to Jen, Van, Mikhail, Kirill, and Nike for many years of friendship and company. Finally, I would like to thank Shrenik, Andrew, and my parents for their love and support.

Chapter 1

Introduction

1.1 Monolayer and bilayer graphene

Monolayer graphene is a two dimensional sheet of carbon atoms arranged in a honeycomb lattice [1,2]. These atoms are connected by hybridized sp^2 orbitals within the plane, while mobile electrons in the out-of-plane p_z orbitals are responsible for the high conductivity of graphene. There are two relevant symmetries for graphene: the conventional spin of electrons and a pseudospin associated with relative weight of the electronic wavefunction on the two sublattices, A and B (see Fig. 1.1). The lattice unit vectors are $\mathbf{a}_1 = \frac{a}{2}(3, \sqrt{3})$ and $\mathbf{a}_2 = \frac{a}{2}(3, -\sqrt{3})$, where $a = 1.42\mathring{A}$ is the distance between nearest-neighbor carbon atoms, and the reciprocal vectors are $\mathbf{b}_1 = \frac{2\pi}{3a}(1, \sqrt{3})$ and $\mathbf{b}_2 = \frac{2\pi}{3a}(1, -\sqrt{3})$. There are two inequivalent Dirac points at the corners of the Brillouin zone in momentum space:

$$\mathbf{K} = \left(\frac{2\pi}{3a}, \frac{2\pi}{3\sqrt{3}a}\right) \quad \text{and} \quad \mathbf{K}' = \left(\frac{2\pi}{3a}, \frac{-2\pi}{3\sqrt{3}a}\right) \tag{1.1}$$

The band structure of monolayer graphene can be derived from a tight-binding calculation that accounts for hopping between both nearest neighbor and next nearest neighbor atoms,

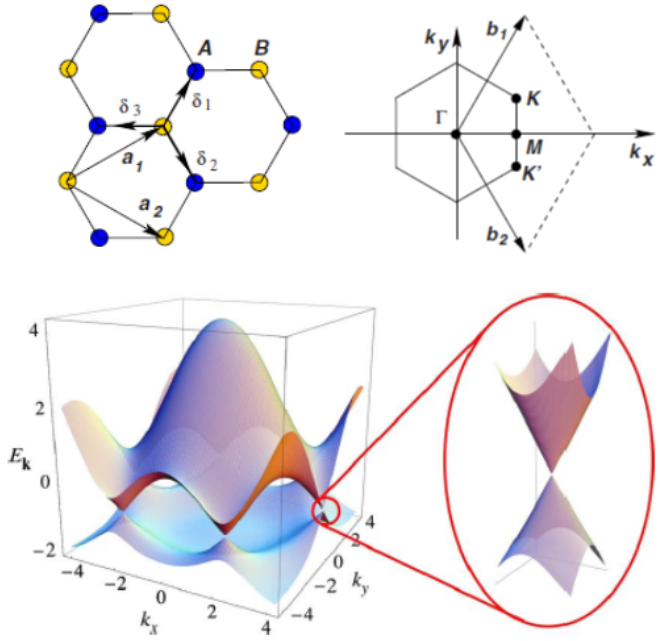

Figure 1.1: The two sublattices of graphene, A and B, and lattice unit vectors $\mathbf{a}_1$ and $\mathbf{a}_2$ are labeled in the schematic. The upper right panel shows the Brillouin zone in momentum space, along with the reciprocal vectors and the $\mathbf{K}$ and $\mathbf{K}'$ points. The bottom panel illustrates the band structure of graphene $E_{\pm}(\mathbf{k})$ obtained from tight binding calculations. At low energies, the linear dispersion relation between energy and momentum gives rise to massless Dirac fermions (inset). Images from A.H. Castro Neto, *et al.*, Rev. Mod. Phys. **81**, 109 - 162 (2009).

which yields the dispersion relation [2]:

$$E_{\pm}(\mathbf{k}) = \pm t\sqrt{3 + 2\cos(\sqrt{3}k_y a) + 4\cos\left(\frac{\sqrt{3}}{2}k_y a\right)\cos\left(\frac{3}{2}k_x a\right)}$$

$$- \mathrm{t}'\left(2\cos(\sqrt{3}k_y a) + 4\cos\left(\tfrac{\sqrt{3}}{2}k_y a\right)\cos\left(\tfrac{3}{2}k_x a\right)\right) \quad (1.2)$$

where $t \sim 2.8$ eV is the nearest neighbor hopping energy and $t' \sim 0.1$ eV is the next nearest neighbor hopping energy. While the band structure is symmetric about zero energy when $t' = 0$, an electron-hole asymmetry can arise in the presence of finite next nearest neighbor hopping. To determine the dispersion at low energies near the Dirac point $\mathbf{K}$, one may

expand the full expression $E_{\pm}(\mathbf{k})$ using $\mathbf{k} = \mathbf{K} + \mathbf{q}$ for $|\mathbf{q}| \ll |\mathbf{K}|$, where $\mathbf{q}$ the momemtum relative to the Dirac point. Upon expanding to first order in $|\mathbf{q}|/|\mathbf{K}|$ and neglecting next nearest neighbor hopping, $E_{\pm}(\mathbf{q}) = \pm v_F|\mathbf{q}|$, where $v_F = 3ta/2 \sim 10^6$ m/s is the Fermi velocity in graphene.

In momentum space, the electronic wavefunction $\psi_{\pm,\mathbf{K}}(\mathbf{k})$ around $\mathbf{K}$ consists of a two component spinor that describes the relative weight of the wavefunction on the two sublattices:

$$\psi_{\pm,\mathbf{K}}(\mathbf{k}) = \frac{1}{\sqrt{2}} \begin{pmatrix} e^{-i\theta_{\mathbf{k}}/2} \\ \\ \pm e^{i\theta_{\mathbf{k}}/2} \end{pmatrix} \quad \text{for} \quad \widehat{H}_K = \hbar v_F \begin{pmatrix} 0 & k_x - ik_y \\ \\ k_x + ik_y & 0 \end{pmatrix} = \hbar v_F \boldsymbol{\sigma} \cdot \mathbf{k} \quad (1.3)$$

where $\theta_{\mathbf{k}} = \arctan(k_x/k_y)$, $\widehat{H}_K$ is the low-energy Hamiltonian near the point $\mathbf{K}$, and

$$\boldsymbol{\sigma} = (\sigma_x, \sigma_y), \quad \text{for} \quad \sigma_x = \begin{pmatrix} 0 & 1 \\ \\ 1 & 0 \end{pmatrix}, \quad \sigma_y = \begin{pmatrix} 0 & -i \\ \\ i & 0 \end{pmatrix} \quad (1.4)$$

Note that states near each Dirac point have a well-defined chirality associated with the locking between pseudospin and momentum, giving rise to a Berry phase of π (illustrated in Fig. 1.2). The eigenenergies of $\widehat{H}$ are $E = \pm v_F k$: this dispersion relation describes electronic charge carriers that behave as massless Dirac fermions. At the other valley $\mathbf{K}'$,

$$\psi_{\pm,\mathbf{K}'}(\mathbf{k}) = \frac{1}{\sqrt{2}} \begin{pmatrix} e^{i\theta_{\mathbf{k}}/2} \\ \\ \pm e^{-i\theta_{\mathbf{k}}/2} \end{pmatrix} \quad \text{for} \quad \widehat{H}_{K'} = \hbar v_F \boldsymbol{\sigma}^* \cdot \mathbf{k} \quad (1.5)$$

Bernal-stacked bilayer graphene has a parabolic dispersion $E = \pm v_F^2 k^2/t_\perp$ (where $t_\perp \sim 0.4$ eV is an interlayer hopping parameter), giving rise to massive charge carriers with effective mass $m^* \sim 0.05 m_e$, where m_e is the mass of the electron [2] (Fig. 1.3). Due

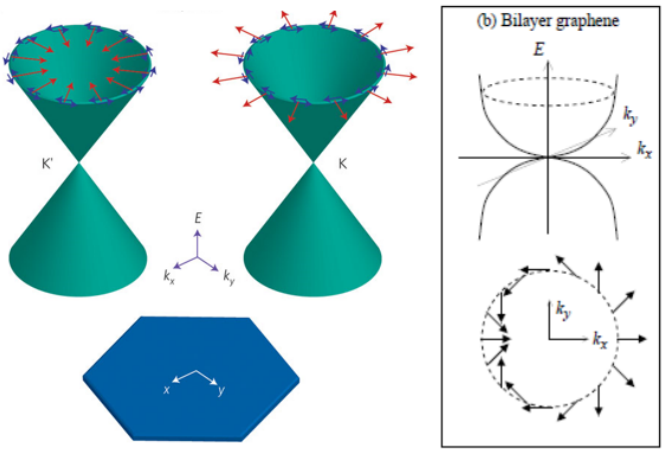

Figure 1.2: The left panel illustrates locking between pseudospin and momentum in opposite valleys **K** and **K′** in monolayer graphene, associated with a Berry's phase of π. The right panel illustrates the winding of pseudospin with momentum near the Dirac point in bilayer graphene, associated with a Berry's phase of 2π. The left image is from A.H. Castro Neto, *et al.*, Rev. Mod. Phys. **81**, 109 - 162 (2009), and the right image is from Park and Mazari, PRB (2011).

to the direct correspondence between layer and sublattice index, application of an electric field perpendicular to the bilayer graphene flake breaks sublattice symmetry and opens an electrostatically tunable bandgap [3–7]. In the presence of an interlayer bias V, the energy of the conduction band becomes: $E = V - 2Vv_F^2k^2/t_\perp + v_F^4k^4/2t_\perp^2V$. Chapter 2 will discuss the experimental observation of an electric field induced bandgap in bilayer graphene in greater detail.

1.2 The quantum Hall effect in graphene and interaction-driven broken symmetry states

When a magnetic field B is applied perpendicular to a two-dimensional electron gas (2DEG), the electronic wavefunctions are solutions to the Hamiltonian $\widehat{H} = (\mathbf{p} - e\mathbf{A})^2/2m$ with Landau gauge $\mathbf{A} = -By\widehat{x}$. The applied B field leads to the formation of a discrete ladder of Landau levels, each carrying a degeneracy $N = eB/h$, with energy spacing $E_n =$

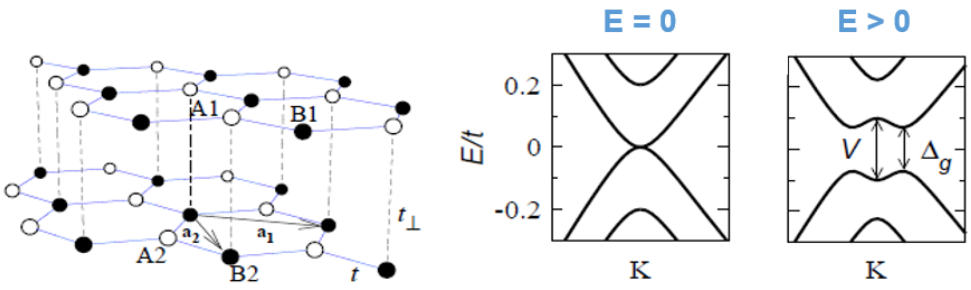

Figure 1.3: Bernal-stacked bilayer graphene has a gapless parabolic dispersion at zero interlayer bias, and charge carriers are massive chiral fermions with effective mass $m^* \sim 0.05m_e$. Application of an electric field perpendicular to the flake breaks layer (or sublattice) symmetry, inducing a gate-tunable bandgap in the density of states. Image: E. V. Castro *et al.*, (2008)

$\hbar\omega_c(n+1/2)$ for $\omega_c = eB/m$ and integer n.

An unconventional quantum Hall effect arises and in monolayer and bilayer graphene, influenced by both the chirality of charge carriers and the band structure [1,2,8–11]. Because monolayer graphene has a linear dispersion, its Landau level energies are different from those in a convention 2DEG. Similar to the above case, one modifies the Hamiltonian $\widehat{H}$ with by replacing $\mathbf{p} \rightarrow \mathbf{p}+e\mathbf{A}$. The electronic wavefunction thus satisfies: $v_F(\mathbf{p}+e\mathbf{A})\cdot\sigma\psi(\mathbf{r}) = E\psi(\mathbf{r})$ with $\mathbf{A} = -By\widehat{x}$. The resulting Landau level energies are: $E_n = \sqrt{2e\hbar v_F^2|n|B}$ (Fig. 1.4). The electronic transport signature of the quantum Hall effect in graphene is a series of quantized conductance plateaus at $\sigma_{xy} = 4(n+1/2)e^2/h = 2, 6, 10 \ldots e^2/h$. The $4e^2/h$ spacing of the plateaus directly reflects the four-fold spin and valley symmetry of graphene. Because bilayer graphene has massive charge carriers and a parabolic dispersion, the Landau levels are equally spaced in energy, similar to the case of the conventional 2DEG: $E_n = \hbar\omega_c\sqrt{n(n-1)}$.

Because Landau levels are highly degenerate flat energy bands with low kinetic energy, the quantum Hall regime provides a natural setting for exploring correlated states that arise from strong interactions between electrons [12–14]. Coulomb repulsions between

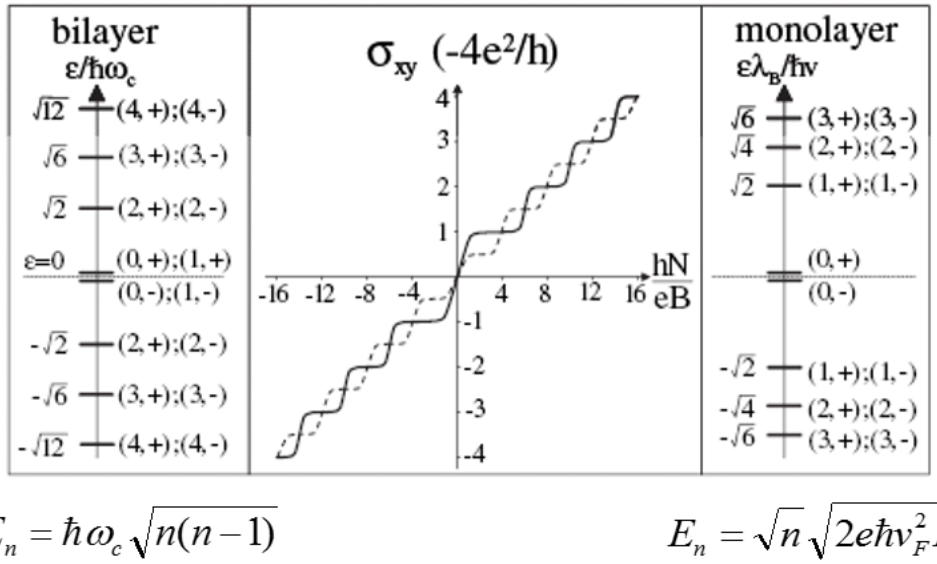

$$E_n = \hbar\omega_c\sqrt{n(n-1)} \qquad E_n = \sqrt{n}\sqrt{2e\hbar v_F^2 B}$$

Figure 1.4: The linear and parabolic band structures of monolayer and bilayer graphene give rise to quadratic and linear Landau level energy spacings, respectively. In monolayer graphene, the quantum Hall effect is manifested as a sequence of plateaus in transverse conductivity, $\sigma_{xy} = \pm 4(n+1/2)e^2/h = \pm 2, 6, 10 \ldots e^2/h$. In bilayer graphene, the sequence is $\sigma_{xy} = \pm 4(n+1)e^2/h = \pm 4, 8, 12 \ldots e^2/h$. In both cases, the $4e^2/h$ spacing of the plateaus is a result of the four-fold spin and valley symmetry; however, there is an eightfold degeneracy in the lowest Landau level in bilayer graphene due to an additional orbital degeneracy. Image adapted from McCann and Falko (2006).

carriers are particularly relevant when the kinetic energy E_{KE} of electrons is substantially weaker than their interaction energy $E_{e-e} = \frac{e^2}{\varepsilon r}$ for dielectric constant ε. For example, at zero magnetic field $E_{e-e} = \frac{e^2}{\varepsilon}\sqrt{n}$, with carrier density $n \propto g k_F^d$, dimensionality d, and degeneracy g. When considering free electrons, $E_{e-e}/E_{KE} \propto gm/\varepsilon\sqrt{n}$, indicating that large electron-electron interaction strength is favored by massive carriers, large degeneracy, low carrier density, and a weak dielectric environment. In the quantum Hall regime, the magnetic length $l_B = \sqrt{\hbar/eB}$ defines the relevant inter-particle spacing and so the interaction energy $E_{e-e} \propto 1/l_B \sim \sqrt{B}$ becomes important at high magnetic fields.

Quantum Hall ferromagnetism is one example of a many-body phenomenon that emerges in graphene devices at high magnetic fields. Due to the Pauli exclusion principle,

repulsions between electrons favor spontaneous spin and/or valley polarization (or combinations of those), resulting in Landau level energy gaps that far exceed the Zeeman energy. For example, in the spin-polarized quantum Hall ferromagnetic state $|\psi\rangle = \varphi(r_1, r_2, \ldots, r_n)|\uparrow\uparrow \ldots \uparrow\rangle$, the orbital part $\varphi(r_1, r_2, \ldots, r_n)$ must be exchange antisymmetric and vanishes as particles approach each other, thus lowering the Coulomb interaction energy. The experimental manifestation of quantum Hall ferromagnetism in graphene is the emergence of broken-symmetry conductance plateaus at all integer multiples of e^2/h in electronic transport measurements [15–19]. Chapter 2 provides a detailed discussion of experiments that control spin- and layer-polarized quantum Hall ferromagnetic states in bilayer graphene. Use of a dual-gated approach enables independent control over the layer pseudospin and the carrier density, which allows one to map out a phase diagram of competing spin and valley ordered states in bilayer graphene as a function of electric and magnetic fields.

1.3 Proximity induced superconductivity in a graphene Josephson junction

The Josephson effect

When two superconducting electrodes are coupled to a graphene sheet to form a Josephson junction, a dissipationless supercurrent can flow through the device mediated by Andreev reflection at the superconductor-graphene interfaces [20–22]. When an electron in the graphene is incident on this interface, it can be Andreev reflected as a hole with opposite spin and valley (necessary to preserve the singlet pairing and zero total momentum of the Cooper pair), as illustrated in Fig. 1.5. The Josephson effect can be summarized by the two Josephson relations: $I = I_c \sin\gamma$ (DC Josephson effect) and $\frac{d\gamma}{dt} = \frac{2eV}{\hbar}$ (AC Josephson effect), where γ is the phase difference across the junction, I_c is the critical current, and V

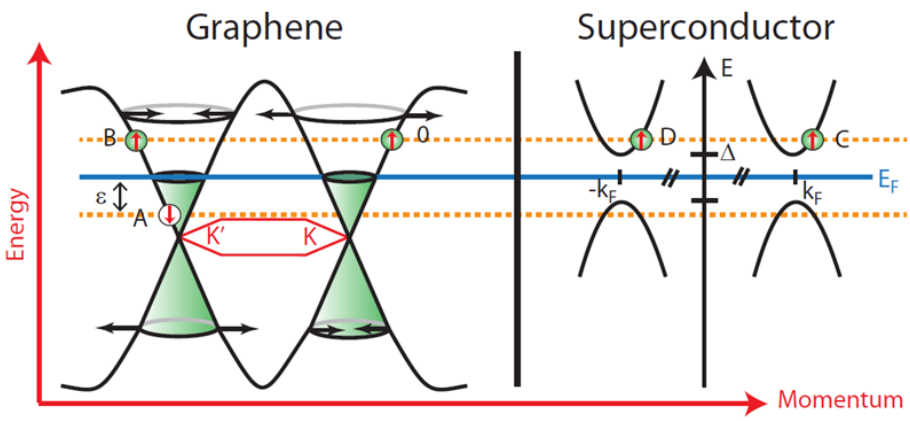

Figure 1.5: Andreev reflection switches both spin and valley to preserve singlet pairing and zero total momentum of the Cooper pair. The the diagram, **0** is the incoming electron, **A** is the Andreev retroreflected hole with opposite spin and valley, **B** is an ordinary reflected electron, and C and **D** indicate transmission through the interface on different sides of the Fermi surface.

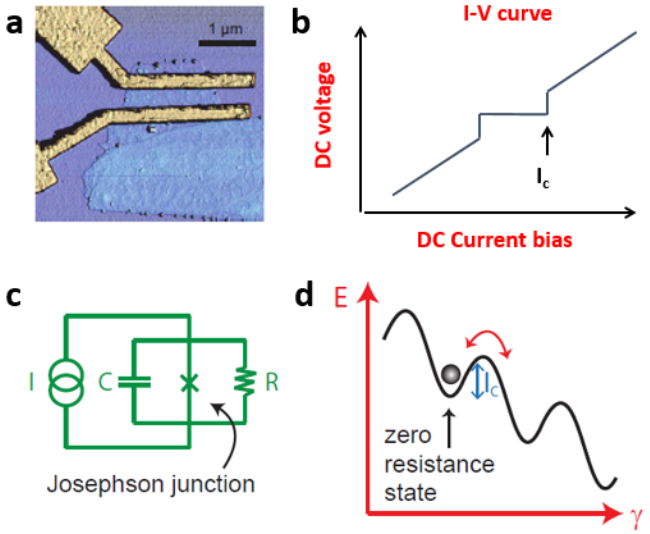

Figure 1.6: **(a)** Atomic force micrograph of a graphene Josephson junction (from Heersche *et al.* Nature (2007)). **(b)** I-V curve of a Josephson junction, where critical current I_c marks the transition between normal and superconducting regimes. **(c)** Circuit for modeling the electrodynamics of a Josephson junction, consisting of a junction in parallel with a resistor and capacitor. **(d)** Tilted washboard model: superconducting state corresponds to a particle with mass $(\hbar/2e)^2C$ trapped in a well in an effective potential $U(\gamma) = -E_J \cos\gamma - \frac{\hbar I}{2e}\gamma$.

is the voltage drop [23]. To understand the electrodynamics of a Josephson junction, we consider a circuit consisting of a junction in parallel with both a shunting resistor R and capacitor C (Fig. 1.6). Express the DC current bias as: $I = I_c \sin\gamma + V/R + C \cdot dV/dt$. Defining the Josephson energy as $E_J = \hbar I_c/2e$ and an "effective mass" $m = (\hbar/2e)^2 C$:

$$m\frac{d^2\gamma}{dt^2} = E_J \sin\gamma + \frac{\hbar I}{2e} + \frac{-1}{R}\left(\frac{\hbar}{2e}\right)^2 \frac{d\gamma}{dt} \tag{1.6}$$

This is the equation of motion of a particle with mass $(\hbar/2e)^2 C$ moving in an effective potential $U(\gamma)$ and subject to a drag force F with a damping coefficient proportional to $1/R$ (tilted washboard picture):

$$m\frac{d^2\gamma}{dt^2} = \frac{-dU}{d\gamma} + F \quad \text{where} \quad U(\gamma) = -E_J\cos\gamma - \frac{\hbar I}{2e}\gamma \quad \text{and} \quad F = -c\frac{d\gamma}{dt} \propto \frac{1}{R}\frac{d\gamma}{dt} \tag{1.7}$$

The superconducting state of the junction corresponds to one in which the "massive particle" is trapped in an energy minimum of the periodic potential, in which the energy barrier heights are proportional to the critical current I_c. The average slope of the potential is defined by the applied DC current bias I. When $I > I_c$, the particle will begin moving down the hill because the slope at every point is negative, eventually reaching an average velocity that is analogous to the DC voltage $V \propto d\gamma/dt$. In a scenario with small damping, hysteresis is expected upon changing the value of applied current bias.

Spatial visualization of current flow using superconducting interferometry

One can obtain information on the spatial distribution of current within a Josephson junction by applying a magnetic flux Φ through the junction area, which induces a position-dependent superconducting phase difference parallel to the graphene/contact interface [23]. As a result, the critical current I_c exhibits interference fringes in B field, given

by:

$$I_c(B) = |\mathcal{I}_c(B)| = \left| \int_{-\infty}^{\infty} J(x) \exp(2\pi i(L + l_{Al})Bx/\Phi_0) dx \right| \tag{1.8}$$

where x is the dimension along the graphene/superconductor interface, L is the distance between contacts, l_{Al} is the magnetic penetration length scale (determined by the London penetration depth of the superconductor and flux focusing), and $\Phi_0 = h/2e$ is the flux quantum. This integral expression applies in the narrow junction limit where $L \ll W$, relevant for our system.

Observing that $\mathcal{I}_c(B)$ represents the complex Fourier transform of the current density distribution $J(x)$, one can apply Fourier methods to extract the spatial structure of current-carrying electronic states [24]. Because the antisymmetric component of $J(x)$ vanishes in the middle of the junction, the relevant quantity for analyzing edge versus bulk behavior is the symmetric component of distribution. By reversing the sign of $I_c(B)$ for alternating lobes of the superconducting interference patterns, we reconstruct $\mathcal{I}_c(B)$ from the recorded critical current. One can determine the real-space current density distribution across the sample by computing the inverse Fourier transform:

$$J_s(x) \approx \int_{-\infty}^{\infty} \mathcal{I}_c(B) \exp(2\pi i(L + l_{Al})Bx/\Phi_0) dB \tag{1.9}$$

We employ a raised cosine filter to taper the window at the endpoints of the scan in order to reduce convolution artifacts due to the finite scan range $B_{min} < B < B_{max}$. This the explicit expression used is:

$$J_s(x) \approx \int_{B_{min}}^{B_{max}} \mathcal{I}_c(B) \cos^n(\pi B/2L_B) \exp(2\pi i(L + l_{Al})Bx/\Phi_0) dB \tag{1.10}$$

where $n = 0.5 - 1$ and $L_B = (B_{max} - B_{min})/2$ is the magnetic field range of the scan. Chap-

ters 4 and 5 employ Fraunhofer interferometry to provide spatial visualization of current flow in graphene Josephson junctions.

1.4 Outline of this thesis

This work explores low-dimensional physics in graphene, especially in regimes where electron interactions or the wavelike nature of particles plays a dominant role, including (1) correlated states that arise from interacting electrons in two dimensions, (2) single electron tunneling in quantum dots, and (3) electronic waveguiding via one-dimensional potentials along the edges of a crystal. The organization of the rest of this thesis is as follows:

- **Chapter 2: Broken-symmetry states in suspended bilayer graphene**. When a large magnetic field is applied in a direction perpendicular to a two-dimensional electron system, Coulomb forces between electrons exceed their kinetic energy, leading to the emergence of collective states that cannot be described by a single-particle picture. Bilayer graphene provides a rich platform for investigation of broken-symmetry states due to the presence of both spin and valley symmetries, which can be controllably broken with external magnetic and electric fields, respectively. We map out the phase diagram of competing ordered states for the $\nu = 0$ quantum Hall ferromagnet and observe a phase transition between high field (valley-polarized) and low field (later revealed to be canted antiferromagnetic) states. This chapter also describes observation of a spontaneous gapped state at low fields near the charge neutrality point.

- **Chapter 3: Gate-defined quantum confinement in suspended bilayer graphene**. Quantum-confined devices that manipulate single electrons in graphene provide an appealing platform for spin-based quantum computing, but the gapless dispersion

of graphene poses a obstacle for confinement of electrons. Here we report quantum confinement in bilayer graphene via local band structure control and observe single electron tunneling in two regimes: at zero magnetic field using the electric field induced gap and at finite magnetic fields using Landau level confinement. The observed Coulomb blockade periodicity agrees with electrostatic simulations based on local top-gate geometry.

- **Chapter 4: Spatially resolved edge currents in graphene**. Graphene provides a platform to explore electronic analogs of optical effects due to the nonclassical nature of ballistic charge transport. Inspired by guiding of light in fiber optics, we demonstrate a means to guide the flow of electrons at the edges of a graphene crystal near charge neutrality. To visualize these states, we employ superconducting interferometry in a graphene Josephson junction and reconstruct the real-space supercurrent density using Fourier methods. We present a model that interprets the observed edge currents as guided-wave states, confined to the edge by natural band bending and transmitted as plane waves.

- **Chapter 5: Visualization of electron interference in a ballistic graphene Josephson junction**. The final part of this thesis focuses on exploring new regimes of superconducting transport in graphene Josephson junctions, in which the wavelike nature of electrons is a dominant feature. The microscopic role of boundaries on wave interference in graphene is an unresolved question due to the challenge of detecting charge flow with submicron resolution. We apply Fraunhofer interferometry to achieve real-space imaging of cavity modes in a graphene Fabry-Pérot resonator, providing evidence of separate interference conditions for edge and bulk currents. We also observe modulation of the multiple Andreev reflection amplitude on and off resonance,

a direct measure of cavity transparency.

Chapter 2

Broken symmetry states in dual-gated suspended bilayer graphene

2.1 Overview

The single-particle energy spectra of graphene and its bilayer counterpart exhibit multiple degeneracies that arise through inherent symmetries. Interactions among charge carriers should spontaneously break these symmetries and lead to ordered states that exhibit energy gaps. In the quantum Hall regime, these states are predicted to be ferromagnetic in nature, whereby the system becomes spin polarized, layer polarized, or both. The parabolic dispersion of bilayer graphene makes it susceptible to interaction-induced symmetry breaking even at zero magnetic field. We investigated the underlying order of the various broken-symmetry states in bilayer graphene suspended between top and bottom gate electrodes. We deduced the order parameter of the various quantum Hall ferromagnetic states by con-

trollably breaking the spin and sublattice symmetries. At small carrier density, we identified three distinct broken-symmetry states, one of which is consistent with either spontaneously broken time-reversal symmetry or spontaneously broken rotational symmetry

2.2 Degeneracies in monolayer and bilayer graphene

In mono- and bilayer graphene, an unconventional quantum Hall effect arises from the chiral nature of the charge carriers in these materials [1, 2, 8–11]. In monolayers, the sequence of Hall plateaus is shifted by a half integer, and each Landau level (LL) is fourfold degenerate due to spin and valley degrees of freedom. The latter valley degree of freedom refers to the conduction and valence bands in single-layer graphene forming conically shaped valleys that touch at two inequivalent Dirac points. In bilayer graphene, an even richer picture emerges in the lowest LL caused by an additional degeneracy between the zeroth and first orbital LLs, giving rise to an eightfold degeneracy. Systems in which multiple LLs are degenerate give rise to broken-symmetry states caused by electron-electron interactions [12]. Such interaction-induced broken-symmetry states in the lowest LL of bilayer graphene have been theoretically predicted [13, 14] and experimentally observed [15–19], but the nature of their order parameters is still debated. For example, two possible order parameters that have been suggested for the gapped phase at filling factor $\nu = 0$ at large magnetic fields are either layer or spin polarization [14]. Moreover, recent theoretical studies predict that even in the absence of external magnetic and electric fields, the parabolic dispersion of bilayer graphene can lead to broken-symmetry states that are induced by interactions among the charge carriers [25–32]. In this work, we map out the various broken-symmetry states as a function of external magnetic and electric field. The nature of these phases can be deduced by investigating their stability under the variation of these symmetry-breaking fields.

2.3 Electric field tunable gap in suspended bilayers

The observation of broken-symmetry states driven by effects of interaction is hampered by the presence of disorder and requires high sample quality. We have developed a method in which bilayer graphene is suspended between a top gate electrode and the substrate. This approach allows us to combine the high quality of suspended devices with the ability to independently control electron density and perpendicular electric field E_{perp}.

A false-color scanning electron micrograph of a typical device is shown in Fig. 2.1a. The suspended graphene (red) is supported by gold contacts (yellow). Suspended top gates (blue) can be designed to cover only part of the graphene (left device) or to fully overlap the entire flake (right device), including part of the contacts. We have investigated both types of devices, which show similar characteristics. The fabrication of such two-terminal devices is detailed in the final section of the chapter (Device Fabrication) and is schematically illustrated in Fig. 2.1a. To improve sample quality, we current anneal [33, 34] our devices in vacuum at 4 K before measurement.

The high quality of our suspended flakes is evident from the dependence of resistance versus applied electric field at zero magnetic field. As theoretically predicted [3–5] and experimentally verified in transport [6, 7] and optical [6, 35, 36] experiments, an applied perpendicular electric field E_{perp} opens a gap $\Delta \sim dE_{perp}/k$ in the otherwise gapless dispersion of bilayer graphene, as schematically shown in the lower left inset to Fig. 2.1b. Here, d is the distance between the graphene sheets and k is a constant that accounts for imperfect screening of the external electric field by the bilayer [3, 5, 29]. The conductance of our suspended bilayer graphene sheet at 100 mK as a function of back (V_b) and top gate (V_t) voltage is shown in Fig. 2.1b. The opening of a field-induced band gap is apparent from the decreased conductance at the charge neutrality point with increasing applied electric

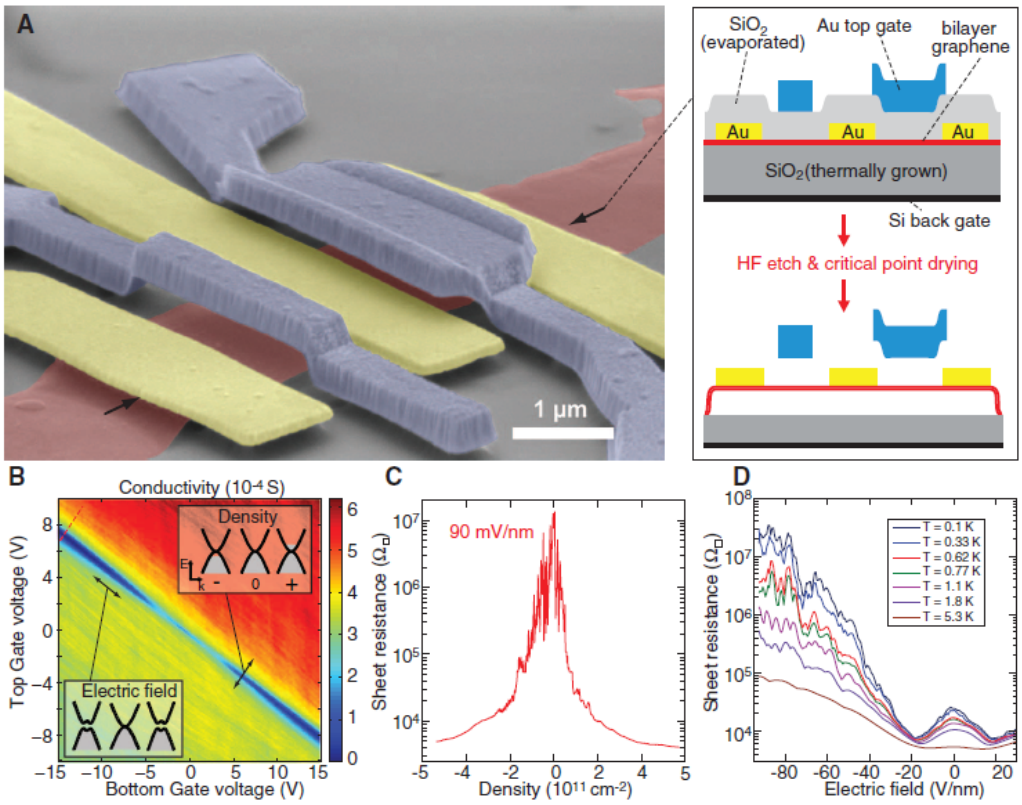

Figure 2.1: **(a)** False-color scanning electron micrograph of a bilayer graphene flake suspended between Cr/Au electrodes with suspended Cr/Au top gates. A schematic of a cross section along a line marked by the two arrows is shown on the right, including a brief depiction of the sample fabrication. We used a threestep electron-beam lithography process in which Cr/Au contacts are first fabricated on the bilayer graphene, followed by deposition of a SiO_2 spacer layer on top of the flake and finally the structure of a Cr/Au topgate above the SiO_2 layer. Subsequent etching of part of the SiO_2 leaves the graphene bilayer suspended between the top and bottom gate electrodes. **(b)** Conductance map as function of top and bottom gate voltage at T = 100 mK of a suspended bilayer graphene flake. **(c)** Line trace along the dashed lines in (b) showing the sheet resistance as a function of charge carrier density at constant electric field. **(d)** Traces of the maximal sheet resistance at the charge neutrality point as a function of applied electric field at different temperatures.

field $E_{perp} = (\alpha V_t - \beta V_b)/2e\varepsilon_0$. Here, α and β are the gate coupling factors for V_t and V_b, respectively, which we determine from the Landau fan in the quantum Hall regime, e is the electron charge, and ε_0 is the vacuum permittivity.

The presence of an energy gap is also illustrated by the line cut in Fig. 2.1c, which shows the resistance at constant E_{perp} as a function of total density $n = (\alpha V_t + \beta V_b)$.

By varying the density, the resistance can be changed by a factor 10^3. Line traces of the maximum sheet resistance as a function of E_{perp} at various temperatures (Fig. 2.1d) illustrate the exponential dependence of the resistance on electric field, as well as a decrease in resistance with temperature. The sheet resistance at 100 mK increases by more than a factor of 2×10^3 (from 8 kΩ per square to 20 MΩ per square) for E_{perp} between 20 and 90 mV/nm. Compared to previous measurements of dually gated graphene bilayers embedded in a dielectric [6], our measurements show an increase by a factor of 10^3 in resistivity at the same electric field, which is the result of the high quality of our flakes. The unexpected finding of a nonmonotonous dependence of the resistance at small applied electric field will be discussed below. The oscillations in the conductance traces shown in Fig. 2.1c are repeatable and result from mesoscopic conductance fluctuations.

2.4 Evolution of Landau levels in electric field

The evolution of different LLs in our samples at nonzero magnetic field was revealed by measuring conductance as a function of E_{perp}. The two-terminal conductance as a function of density and electric field at various different magnetic fields (Fig. 2.2a-d) shows the previously reported eightfold degeneracy of the lowest LL, which is fully lifted because of electron-electron interactions [15, 16, 19]. Plateaus at $\nu = 0, \pm 1, \pm 2, \pm 3$ can be identified by their slope in a fan diagram. Vertical line cuts that correspond to a constant filling factor show that the conductance is quantized except at particular values of electric field, denoted by stars or dots in Fig. 2.2a-d. The $\nu = 0$ state is quantized except near two values of the applied electric field (marked with dots). This value of electric field increases as the magnetic field B increases. The $\nu = \pm 2$ state is quantized for all electric fields except near $E_{perp} = 0$; finally, the $\nu = \pm 4$ state is quantized for all electric fields.

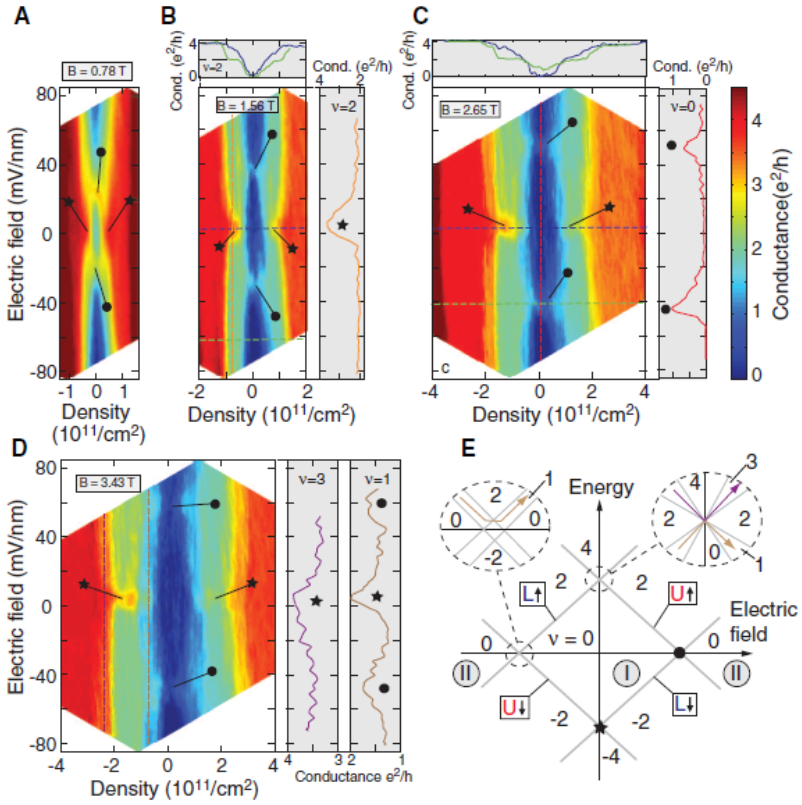

Figure 2.2: **(a)** to **(d)** Maps of the conductance in units of e^2/h as a function of applied electric field E_{perp} and density n at various constant magnetic fields at T = 60 mK. Line traces are taken from the data along the dashed lines. Horizontal line traces correspond to cuts at constant electric field; vertical line cuts correspond to cuts along constant filling factor. In (b), the orange line cut corresponds to the electric field dependence of $\nu = 0$ and the vertical line cuts to the density dependence of the conductance at two constant electric fields showing the emergence of $\nu = 2$ at large electric fields. In (c), the red vertical line cut corresponds to the electric field dependence of $\nu = 0$. The horizontal line cuts in green and blue show the density dependence of the conductance at two different electric fields showing the suppression of the $\nu = 0$ state at a finite electric field. In (d), the brown (violet) line cut shows the conductance as function of electric field at $\nu = 1$ ($\nu = 3$). **(e)** Schematic diagram of the energetic position of the lowest LL octet (gray lines) as a function of E_{perp}. The quantum numbers U, L, ↑, and ↓ of the LLs are indicated in the squares. The respective filling factors ν are indicted in black numbers. The LLs in the main scheme are all doubly degenerate in orbital quantum numbers. The effect of the electric field on the orbital LLs is shown in the two insets. The two different $\nu = 0$ states are marked with Roman numerals. In all images, the crossing of LLs at zero electric field is marked with a star and the crossing at zero energy is marked with a dot.

A qualitative understanding of this phenomenology can be gained from a simplified scheme of the LL energies as a function of electric field (Fig. 2.2e, gray lines) for nonzero magnetic field. We start by neglecting the breaking of the orbital degree of freedom so that the LLs are each doubly degenerate [11]. We assume, in accordance with theoretical predictions, that at $E_{perp} = 0$ only the spin degeneracy is lifted, giving rise to a spin-polarized $\nu = 0$ quantum Hall ferromagnetic state [14, 29]. In the lowest LL, the layer and valley index are equivalent [11] so that an electric field that favors one of the layers directly controls the valley-pseudospin. As a result, LLs of quantum number U (upper layer) or L (lower layer) are expected to have different slopes in electric field. At several points, marked by dots or stars in the schematic of Fig. 2.2e, LL crossings occur. A LL crossing is seen at $E_{perp} = 0$ for both $\nu = 2$ and $\nu = -2$, and two LL crossings are seen for $\nu = 0$ at nonzero E_{perp}. We hypothesize that these crossings are responsible for the increased conductance in our transport experiments [37]. Figure 2.2e shows the LL energy, whereas we have direct control over the density of the bilayer rather than its chemical potential. However, on a quantum Hall plateau, the chemical potential lies between two LL energies, which enables us to relate our scheme in Fig. 2.2e to our transport data as detailed below.

The LL crossings at zero average carrier density are marked by dots in Fig. 2.2. In our proposed scheme, these transitions separate a spin-polarized $\nu = 0$ state at low electric fields (I) from two layer-polarized $\nu = 0$ states at large electric fields (II) of opposite layer polarization. The line cut in Fig. 2.2c at constant filling factor shows that insulating $\nu = 0$ states are well developed at zero electric field and at large electric fields, but the crossover between these states is marked by a region of increased conductance. The experimentally observed large resistance of the phase at $E_{perp} = 0$ [15, 16] is at variance with the theoretical prediction of percolating edge modes [38] in the case of a spin-polarized $\nu = 0$ state. A possible reason for this discrepancy is the mixing of counterpropagating edge modes and

subsequent opening of a gap [39].

The LL crossings at $\nu = \pm 2$ near zero electric field are marked by stars in Fig. 2.2. An example of such a crossing is apparent in the vertical line cut shown in Fig. 2.2b. There, the conductance at $\nu = \pm 2$ increases near zero electric field, which is explained in our scheme by a crossing between two LLs of identical spin polarization but opposite layer polarization. The consequence of these crossings is that only $\nu = 0$ and $n = \pm 4$ states occur at zero electric field, whereas layer-polarized $n = \pm 2$ states emerge only at finite electric field, as is apparent in the horizontal line cuts of Fig. 2.2b.

Assuming that the $\nu = \pm 1$ and ± 3 states are partially layer polarized [14], the electric field should also induce a splitting at these filling factors (inset to Fig. 2.2e) that is, however, more fragile and only seen at higher magnetic fields. Our simple model predicts that the $n = \pm 3$ state will have a crossing at zero electric field, and we attribute the increase in conductance at $E_{perp} = 0$ in the left line cut in Fig. 2.2d to be a signature of this crossing. The $n = \pm 1$ state is expected to have three crossings: one at zero electric field and two near the same nonzero electric field at which the transition between the $\nu = 0$ states is observed. All three of these crossings are apparent from the regions of increased conductance in the right line cut in Fig. 2.2d. The observation that $n = \pm 1$ and ± 3 states are enhanced with electric field is an indication of their partial layer polarization. Theory nonetheless predicts that $n = \pm 1, \pm 2, \pm 3$ should also be seen at $E_{perp} = 0$ [14]. However, the predicted energy gaps of these states are expected to be considerably smaller than that of $\nu = 0$ and hence visible only at large magnetic field. Indeed, for $B > 4$ T, these broken symmetry states at $E_{perp} = 0$ can also be observed in our data.

2.5 Phase diagram of the $\nu = 0$ state

When we examine the conductance at the charge neutrality point as a function of electric and magnetic field (Fig. 2.3a) in more detail, we observe that regions of high conductance mark the transition between the low- and high-field $\nu = 0$ states (highlighted with dots in Fig. 2.2). The transition moves out to larger electric fields as the magnetic field is increased, which implies that phase I is stable at large magnetic fields and is destabilized by an electric field. This observation is also consistent with our energy diagram (Fig. 2.2e), which predicts that the $\nu = 0$ LL crossing will move out to higher electric fields when the magnetic field increases. The increased stability of this phase at higher magnetic fields reconfirms our initial assumption that phase I is spin polarized. In contrast, the phase at large electric fields (phase II) is stabilized by an electric field, consistent with it being layer polarized.

The dependence of the transition region between the two phases on electric and magnetic field is shown more clearly in Fig. 2.3b, where we have extracted the maximum conductance in Fig. 2.3a for all positive values of electric field. At large magnetic field, the transition line is linear and is independent of sample quality and temperature (we have investigated a total of five samples at temperatures between 100 mK and 5 K). At magnetic fields below about 2 T, however, the transition line is linear only in the highest quality sample and at low temperatures (inset to Fig. 2.3a and dashed line in Fig. 2.3b). A surprising observation is that the extrapolation of the linear dependence from high B down to B = 0 results in a crossing at a nonzero electric field, E_{off}. Moreover, the slope and E_{off} that characterize the large B behavior seem to have no systematic dependence on sample quality or temperature T (Fig. 2.3c-d). The conductance at the transition between the $\nu = 0$ phases decreases both with increasing B as well as with decreasing T [see Fig. S5

(23)]. Such behavior is qualitatively expected given that LL mixing at these crossing points can lead to the opening of gaps in the spectrum.

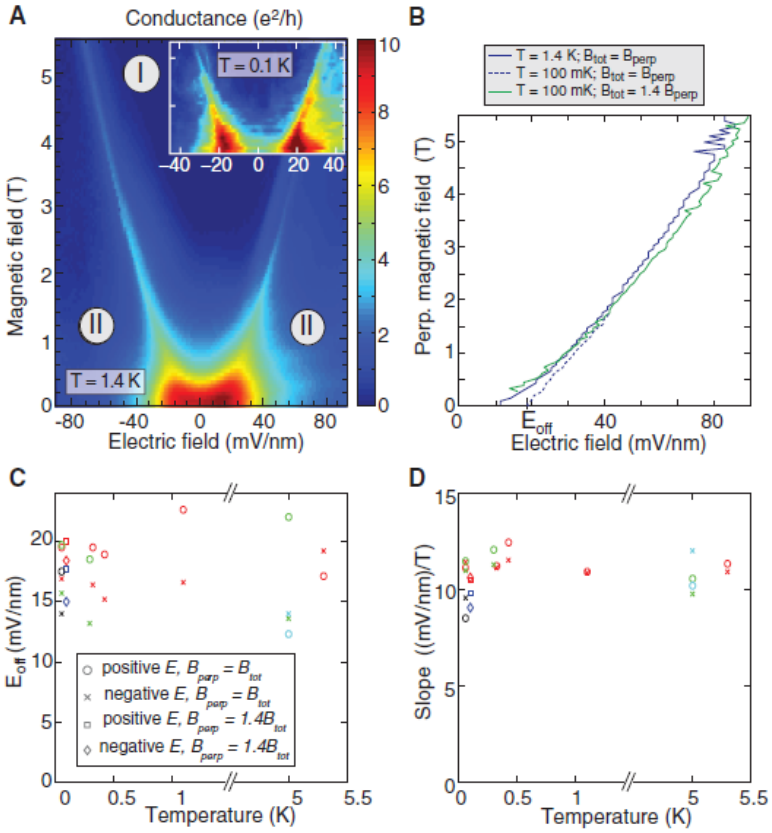

Figure 2.3: **(a)** Conductance in units of e^2/h as a function of applied electric and magnetic fields at zero average carrier density at 1.4 K. The transition between different $\nu = 0$ states is characterized by a region of increased conductance. (Inset) Measurement taken at 100 mK when the sample has been tilted with respect to the magnetic field, plotted against the perpendicular component of the magnetic field after thermal cycling. The color scale of the inset ranges from 0 (blue) to 4.5 (red) e^2/h. The y axis of the inset ranges from 0 to 1.3 T. **(b)** Comparison of the slope of the transition line when the sample is perpendicular to the magnetic field and at a 45 degree angle. **(c)** and **(d)** Comparison of the E_{off} and high magnetic field slope of the transition line for different temperatures. Different colors correspond to different samples.

To further elucidate the nature of the transition, we investigated the role of the Zeeman energy E_z across the $\nu = 0$ transition in detail. We tilted the sample with respect to the magnetic field, which altered E_z but left all interaction-dependent energy scales the

same. Figure 2.3b shows both measurements under titled magnetic field (green line) and data taken in purely perpendicular field (blue line). The two transition lines have similar slopes, which indicates that E_z is negligible and the transition predominantly depends on the perpendicular component of the magnetic field, underscoring that exchange effects and the LL degeneracies play an important role. However, this explanation does not account for the B = 0 offset.

The crossover between two phases with the application of an electric field has also been predicted theoretically by Gorbar *et al.* [40] and Nandkishore and Levitov [29]. Gorbar *et al.* [40] predict a transition from a quantum Hall ferromagnetic state at low electric fields to an insulating state dominated by magnetic catalysis with a slope of about 2 mV nm^{-1} T^{-1}. Nandkishore and Levitov [29] predict a transition from a quantum Hall ferromagnetic state to a layer insulating state at large electric fields, with a slope of 34 mV nm^{-1} T^{-1}. Our measured slope is about 11 mV nm^{-1} T^{-1}. A qualitative comparison between the experimentally obtained values and the theory is difficult because of the lack of knowledge of the screening that the bilayer provides to the applied electric field once LLs are formed.

2.6 Spontaneous gapped phase in bilayer graphene at zero field

A notable feature seen in the inset to Fig. 2.3a and in Fig. 2.3b is that the transition line appears to have a nonzero offset in electric field, $E_{off} \sim 20$ mV/nm. The B = 0 offset coincides with the extrapolated one from high fields when the sample quality is high and the temperature is low. This result suggests that the transition from a spin- to a layer-polarized phase persists all the way down to B = 0, but careful measurements near B = 0 and $E_{perp} = 0$ (Fig. 2.4a) show that this conclusion is incorrect. We will discuss

possible origins for Eoff in the remainder of this manuscript.

The conductance close to the charge neutrality point at small electric and magnetic fields is shown in Fig. 2.4a. The conductance at B = 0 and $E_{perp} = 0$ exhibits a local minimum and increases upon increase of E_{perp} and B. The electric field value at which the conductance reaches a maximum coincides with E_{off}. Together with observation of a maximum of the conductance at a finite value $B_{off} = \pm 50$ mT, our observations suggest that neither the spin-polarized phase I nor the layer-polarized phase II extend down to B = 0 and $E_{perp} = 0$. Instead, our measurements are consistent with the presence of a third phase at small electric and magnetic fields. The electric field dependence of the resistance is at variance with simple calculations of the band structure of bilayer graphene. In a tight binding model, bilayer graphene is expected to evolve from a gapless semimetal to a gapped semiconductor whose gap magnitude depends monotonically on electric field [3]. However, our measurements show that the conductance does not decrease monotonically with electric field, instead exhibiting a local maximum at about ±20 mV/nm (Fig. 2.4b). The maximum resistance at B = 0 and close to zero carrier density as a function of E_{perp} for different temperatures increases as T decreases [see Fig. 2.1d], reaching 20 kΩ at the lowest temperature of 100 mK. It therefore strongly suggests that the neutral bilayer graphene system is already gapped at $E_{perp} = 0$ and B = 0 and that fields larger than E_{off} or B_{off} transfer the system into the layer- or spin-polarized phases (Fig. 2.4a). In Fig. 2.4b, the dependence of the conductance as a function of density and electric field at B = 0 is shown. Also in this case, a minimum of the conductance at small electric field and density can be discerned, indicating that the spontaneous phase is unstable away from the charge neutrality point. The temperature dependence at the crossover field of $E_{perp} = \pm 20$ mV/nm is weak (Fig. 2.1d), consistent with the closure of a gap. Our observations cannot be explained with known single-particle effects.

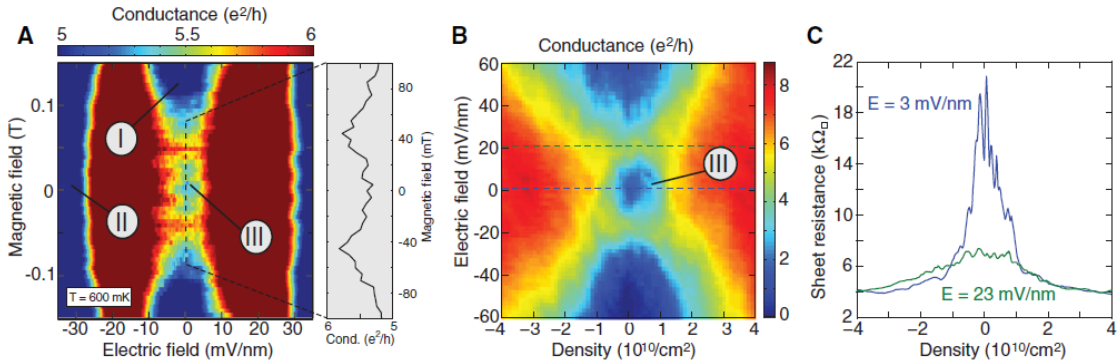

Figure 2.4: **(a)** Detailed view of the conductivity at small electric and magnetic fields and zero average carrier density. The color scale has been restricted to between 5 and 6 e^2/h to highlight the observed effect. **(b)** Conductivity as a function of electric field and density at zero magnetic field. **(c)** Two linecuts showing the resistivity at E = 0 and E_{off} are also shown. The scans in (b) and (c) were taken after thermal cycling of the sample, hence the difference in the minimal conductance at zero magnetic and electric field with respect to (a).

It has been pointed out theoretically [25–32] that electron-electron interactions can open a spontaneous gap in bilayer graphene near the charge neutrality point at zero electric and magnetic fields. Several different phases have been proposed, and our experimental observations considerably restrict the various possible theoretical explanations to two prevailing theories. The first theory [29] predicts a phase diagram very similar to what we measure. Within this theory, phase III is associated with an anomalous quantum Hall insulating state that spontaneously breaks time-reversal symmetry. This state is characterized by an antiferromagnetic ordering in the pseudospin (layer). In this phase, electrons from one valley occupy one of the layers, whereas electrons from the other valley occupy the other layer. An important feature of this state is that it supports topologically protected current-carrying edge modes and is therefore predicted to have a finite conductance. This prediction is consistent with our observations of a nondiverging resistance at B = 0 and $E_{perp} = 0$ as T is lowered. Although our observed phase diagram agrees qualitatively with that predicted in [29], we find a quantitative disagreement between the measured and predicted E and B

transition values. We find that the magnetic field at which the spontaneous phase breaks down is about 50 mT, an order of magnitude smaller than the theoretically predicted value of 500 mT [29]. An applied electric field of about $E_{off} = 20$ mV/nm quenches the spontaneous gap, compared to the predicted value of 26 mV/nm for the screened electric field. Notably, we need to scale our measured E_{off} by the screening constant k, which means that our values differ by roughly a factor $k = 3$ from the theory [29]. A second prevailing theory for the observed behavior stems from symmetry breaking, which results in the lowering of the density of states at the charge neutrality point. One such example is the nematic state that stems from the breaking of rotational symmetry due to electron-electron interactions. This phase has been predicted to lead to a decreased density of states at the charge neutrality point due to the breaking of the system into two Dirac cones [31,32], consistent with our measured decrease in conductance at small densities. Further experimental support for the above two scenarios is given in [18], where it is shown that known single-particle effects cannot explain the observed behavior.

2.7 Device fabrication

Substrate cleaning and graphene deposition are performed similar procedure to that described by Feldman *et al.* [15]. Graphene bilayers are identified by their contrast in an optical microscope and their characteristic quantum Hall effect. Suitable flakes are contacted with Cr/Au contacts (3 nm/100 nm) by standard electron beam lithography, thermal metal evaporation and lift-off in acetone. Silicon dioxide is structured on top of graphene bilayers in a second electron beam lithography step, followed by electron beam evaporation of silicon dioxide and lift off. The silicon dioxide is used as a spacer layer to separate the top gate from the flake. A final electron beam lithography step is used to

pattern top gates that are suspended above the substrate in the areas that the silicon oxide had been evaporated. Finally, the device is immersed into 5:1 buffered oxide etch for 90s and dried in methanol in a critical point dryer.

Chapter 3

Gate defined quantum confinement in suspended bilayer graphene

3.1 Overview

Quantum confined devices that manipulate single electrons in graphene are emerging as attractive candidates for nanoelectronics applications. Previous experiments have employed etched graphene nanostructures, but edge and substrate disorder severely limit device functionality. Here we present a technique that builds quantum confined structures in suspended bilayer graphene with tunnel barriers defined by external electric fields that open a bandgap, thereby eliminating both edge and substrate disorder. We report clean quantum dot formation in two regimes: at zero magnetic field B using the energy gap induced by a perpendicular electric field and at $B > 0$ using the quantum Hall $\nu = 0$ gap for confinement. Coulomb blockade oscillations exhibit periodicity consistent with electrostatic simulations based on local top gate geometry, a direct demonstration of local control over the band structure of graphene. This technology integrates single electron transport

with high device quality and access to vibrational modes, enabling broad applications from electromechanical sensors to quantum bits.

3.2 Quantum confinement in graphene

Nanopatterned graphene devices, from field-effect transistors to quantum dots [9, 41, 42], have been the subject of intensive research due to their novel electronic properties and two-dimensional structure [1, 2]. For example, nanostructured carbon is a promising candidate for spin-based quantum computation [43] due to the ability to suppress hyperfine coupling to nuclear spins, a dominant source of spin decoherence [44–46], by using isotopically pure ^{12}C. Graphene is a particularly attractive host for lateral quantum dots since both valley and spin indices are available to encode information, a feature absent in GaAs [47–49]. Yet graphene lacks an intrinsic bandgap [2], which poses a serious challenge for the creation of such devices. Transport properties of on-substrate graphene nanostructures defined by etching [9, 42] are severely limited by both edge disorder and charge inhomogeneities arising from ionized impurities in gate dielectrics [50, 51]. The absence of spin blockade in etched double dots is perhaps symptomatic of these obstacles [52, 53]. Unzipping carbon nanotubes yields clean nanoribbon dots, but this approach cannot produce arbitrarily shaped nanostructures with tunable constrictions [54]. However, local bandgap engineering in bilayer graphene enables production of tunable tunnel barriers defined by local electrostatic gates [55], thus providing clean electron confinement isolated from edge disorder.

Bernal stacked bilayer graphene is naturally suited for bandgap control because of its rich system of degeneracies that couple to externally applied fields. At $B = 0$, breaking layer inversion symmetry opens an energy gap tunable up to 250 meV with an external

perpendicular electric field E [4,6,7,11,56–58] that can be used for confinement. In devices with low disorder and at high magnetic fields, gapped states emerge from Coulomb-driven effects that break its eightfold degeneracy (spin, valley, and orbital), resulting in quantum Hall plateaus at all integer multiples of e^2/h for electron charge e and Planck's constant h [59]. Due to the Pauli exclusion principle, Coulomb repulsions between electrons favor spontaneous spin and/or valley polarization (or combinations of those), known as quantum Hall ferromagnetism, resulting in a gap at zero carrier density that far exceeds the Zeeman splitting energy $g\mu_{\mathrm{B}}B$ [15,16]. The large exchange-enhanced energy gap of $\Delta = 1.7$ meV/T measured for the $\nu = 0$ state is ideally suited for quantum confinement [18]. Because valley and layer indices are identical in the lowest Landau level, one may additionally induce a tunable valley gap in the density of states by applying a perpendicular E field that breaks layer inversion symmetry [60]. This coupling of valley index to E field is the key property that enables direct experimental control of the relative spin and valley gap sizes in magnetic field.

Here we demonstrate a technology that enables microscopic bandgap control in graphene for the first time. We report fully suspended quantum dots in bilayer graphene with smooth, tunable tunnel barriers defined by local electrostatic gating. Local gap control in graphene opens an avenue to explore a variety of intriguing systems, including spin qubits [43], topological confinement and valleytronics [61], quantum Hall edge modes in an environment well-isolated from edge disorder, gate-controlled superconductivity, and many more. While not the sole use for this technology, quantum dots provide a good experimental platform to rigorously demonstrate local bandgap engineering due to the precise quantitative relationship between dot area and quantized charge tunneling periodicity. Our technique, which artificially modifies the bandgap of bilayer graphene over nanometer scales, achieves clean electron confinement isolated from both edge and substrate disorder.

3.3 Device overview

We fabricate fully suspended quantum dots with 150 to 450 nm lithographic diameters as illustrated schematically in Fig. 3.1a following the procedure described in the Methods. Graphene is suspended between two Cr/Au electrodes and sits below suspended local top gates (Fig. 3.1b and Supplementary Fig. A.1). Before measurement, the devices are current annealed in vacuum to enhance quality. The high quality of our suspended flakes is evident from the full lifting of the eightfold degeneracy in the quantum Hall regime (Supplementary Fig. A.2) [60] and large resistances attained by opening the E field induced gap at $B = 0$ and $E = 90\text{V/nm}$, a hundred times greater than reported for on-substrate bilayers at similar electric fields [6, 60]. Measurements are conducted in a dilution refrigerator at an electron temperature of 110 mK, as determined from fits to Coulomb blockade oscillations.

3.4 Quantum confinement at zero magnetic field

At $B = 0$, the electric field effect in bilayer graphene enables the production of quantum confined structures with smooth, tunable tunnel barriers defined by local gating [47], thus avoiding disorder arising from the physical edge of the flake. Broken layer inversion symmetry opens a bandgap $\Delta \propto E = (\alpha V_\text{t} - \beta V_\text{b})/2e\varepsilon_0$, where V_t and V_b are top and back gate voltages with coupling factors α and β, respectively, and ε_0 is vacuum permittivity. Coupling to the back gate β is extracted from Landau fans in the quantum Hall regime and the relative gate coupling α/β can be determined from the Dirac peak slope in a V_t vs. V_b plot of conductance at $B = 0$. Properties of individual quantum point contacts are described in greater detail in Supplementary Figs. A.3 and A.4, where pinch-off and behavior consistent with conductance quantization are observed. Quantum dot formation

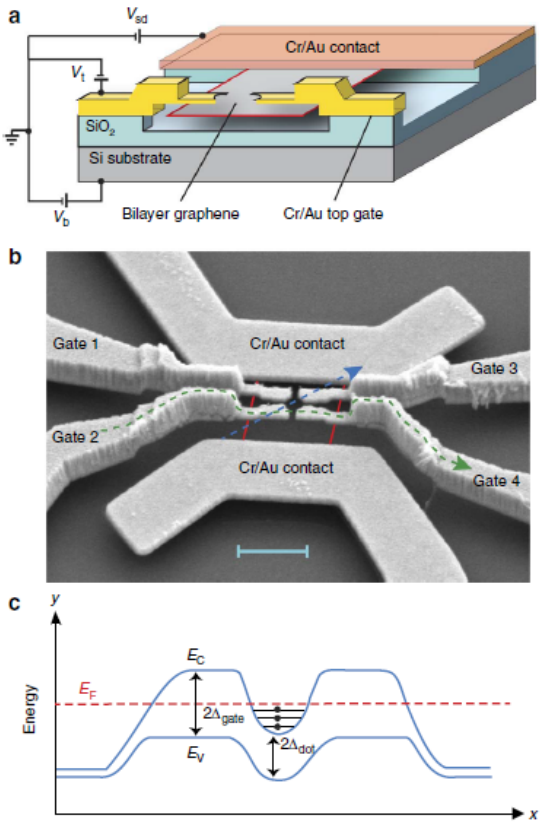

Figure 3.1: **(a)** Schematic cross-section of a suspended gate-defined bilayer graphene quantum dot. The electric field and carrier density profiles are controlled with back and top gate voltages V_b and V_t, while application of a bias V_{sd} across the electrodes enables transport measurements. **(b)** Scanning electron micrograph of quantum dot device similar to D4 (see Methods for sample labeling key). Bilayer graphene (not visible) is suspended between two electrodes below local top gates. Green and blue lines indicate cross-sectional cuts in (a) and (c), respectively. Red lines mark the estimated graphene boundaries. The scale bar represents $1\mu m$. **(c)** Quantum dot formation at $B = 0$, illustrated in a cross-sectional cut of energy vs. position. E_C and E_V mark the edges of the conductance and valence bands. Tunnel barriers are formed by inducing a bandgap with an external E field while fixing V_t and V_b at a ratio that places the Fermi energy E_F within the gap. Uncompensated back gate voltage in the non top-gated regions enables charge accumulation in the dot and leads.

at $B = 0$ is illustrated schematically in Fig. 3.1c. To create tunnel barriers beneath the top gates, we induce a bandgap by applying a field E while fixing V_t and V_b at a ratio that maintains zero carrier density n, where $n = \alpha V_t + \beta V_b$. In the non top-gated regions, there is a finite charge accumulation due to an uncompensated back gate voltage. For gates

in a quantum dot geometry, this restricts electron transport to resonant tunneling events through the constrictions.

Periodic Coulomb blockade oscillations are observed at $B = 0$ which couple to both top and back gates (Fig. 3.2a). A peak in the 2D Fourier transform corresponding to an oscillation spacing of ~ 11mV in V_{b} reflects this strong periodicity (Fig. 3.2b), and the appearance of higher harmonics reveals the non-sinusoidal nature of the Coulomb blockade peaks when $k_{\mathrm{B}}T \ll E_{\mathrm{C}}$, where k_{B} is Boltzmann's constant, T is temperature, and E_{C} is the dot charging energy. Coulomb diamonds shown in Fig. 3.2c have symmetric structure that suggests equal tunnel coupling to both the source and drain leads. The dot charging energy extracted from the DC bias data is $E_{\mathrm{C}} \approx 0.4$ meV. Fig. 3.2d indicates that the periodic Coulomb blockade oscillations have comparable capacitive coupling to each pair of top gates. Furthermore, an even-odd effect is visible in a Coulomb blockade plot as a function of V_{t12} at fixed $V_{\mathrm{t34}} = 9.27$ V and $V_{\mathrm{b}} = -10.7$ V (Supplementary Fig. A.5), consistent with the presence of a two-fold degeneracy. The conductance modulations that couple exclusively to the back gate in Fig. 3.2a likely result from weak parallel conductance channels under gates 3 and 4 (as labeled in Fig. 3.1b) and are unrelated to the central gate-defined quantum dot formation because capacitive coupling to V_{t12} is absent. The horizontal modulations in Fig. 3.2d couple only to V_{t34} but not V_{t12} and are thus expected to have similar origins. Because these features are sparse and aperiodic in nature, we expect that they are not generated by random dot formation in the constrictions or under the local gates. We note that the highly resistive $\nu = 0$ gap in the quantum Hall regime enables more robust confinement than the electric field induced gap, and we demonstrate that all background conductance fluctuations are completely eliminated in Fig. 3.3.

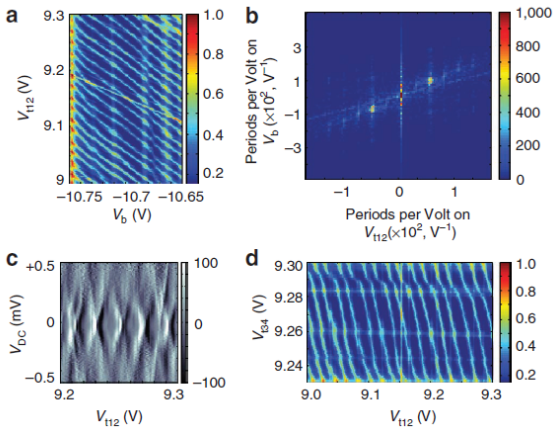

Figure 3.2: **(a)** Conductance map (units of e^2/h) of Coulomb blockade oscillations as a function of back gate voltage (V_b) and the voltage on top gates 1 and 2 (V_t12) at $T = 110$ mK in a four gate dot (device D4). The voltage on top gates 3 and 4 is fixed at $V_\mathrm{t34} = 9.27$ V. **(b)** 2D fast Fourier transform (units of $e^2/h \cdot V$) of (a) reveals the periodic structure. A peak corresponding to an oscillation spacing of ~ 11mV in V_b reflects strong periodicity, while the appearance of higher harmonics reveals the non-sinusoidal nature of the Coulomb blockade peaks when $k_\mathrm{B}T \ll E_\mathrm{C}$. **(c)** Coulomb diamonds are shown in a plot of $\Delta G/\Delta V_\mathrm{t12}$as a function of V_t12 and V_DC, where G is conductance in units of e^2/h and V_DC is the DC bias across the electrodes. The voltages $V_\mathrm{b} = -10.7$V and $V_\mathrm{t34} = 9.27$ V are held constant. Symmetric Coulomb diamonds suggests equal tunnel coupling to source and drain leads. The dot charging energy is $E_\mathrm{C} \approx 0.4$ meV. **(d)** Conductance map (units of e^2/h) of Coulomb blockade oscillations as a function of V_t12 and V_t34 at fixed back gate voltage $V_\mathrm{b} = -10.7$V.

3.5 Coulomb blockade in the quantum Hall regime

Coulomb blockade oscillations can also be generated at finite B field using the exchange-enhanced $\nu = 0$ gap. Here the bilayer is naturally in a gapped quantum Hall state at zero density, where high resistances due to quantum Hall ferromagnetism make this system ideal for confinement. An isolated puddle of charge is created by fixing the Fermi energy in the top-gated regions at the middle of the $\nu = 0$ gap while allowing occupation of higher Landau levels elsewhere, shown schematically in Fig. 3.3a. It should be noted that measurements in the quantum Hall regime are conducted in the valley-polarized $\nu = 0$ state, far from the transition to the spin-polarized phase [60]. Fig. 3.3b shows over forty consecutive Coulomb blockade oscillations generated at 5.2 T in a 2-gate dot with a 400

nm lithographic diameter. The slopes of the resonances indicate symmetric coupling to the two top gates, as expected for a centrally located dot. As top gate voltages are swept to more positive values, peak amplitude is suppressed, revealing moderate tunnel barrier tunability. Also seen in Fig. 3.3b are interruptions in the conductance resonances (vertical and horizontal features) that couple exclusively to a single top gate; due to their sparse and aperiodic nature, we believe that they represent charging events below the gates. Coulomb blockade oscillations are robust over a wide voltage range: Fig. 3.3c shows an additional forty peaks generated under new gate conditions. The Coulomb diamonds exhibit symmetric tunnel coupling to source and drain leads and a dot charging energy of $E_{\mathrm{C}} \approx 0.4$ meV. The strongly periodic nature of the oscillations is evident in the Fourier transform of the data (Fig. 3.3d). See Supplementary Fig. A.6 for additional Coulomb blockade data.

3.6 Geometric control over Coulomb blockade period

To demonstrate geometric control over dot size, we examine the correspondence between top gate dimensions and Coulomb blockade peak spacing. Measurements were performed on five dots with lithographic diameters ranging from 150-450 nm at magnetic fields of 0 to 7 T. The ability to decrease peak spacing by increasing lithographic dot size is illustrated in Fig. 3.4a-c. Fig. 3.4a and 3.4b show Coulomb blockade peak conductance as a function of back gate voltage V_{b} observed in device D1 at $B = 5.2$ T, and D2 at $B = 7$ T, respectively (see Methods for sample labeling key). Black points represent data and the red lines are fits used to extract peak positions. Fig. 3.4c shows relative peak position, $V(p) - V_0$, plotted as a function of peak number p for the first 10 peaks of Fig. 3.4a and 3.4b, where $V(p)$ is the position of peak p in back gate voltage, and V_0 is the position of the first peak. Each data set is accompanied by a corresponding plot of $y(p) = [\frac{1}{9}\sum_{q=0}^{8} V(q+1) - V(q)]p$, where

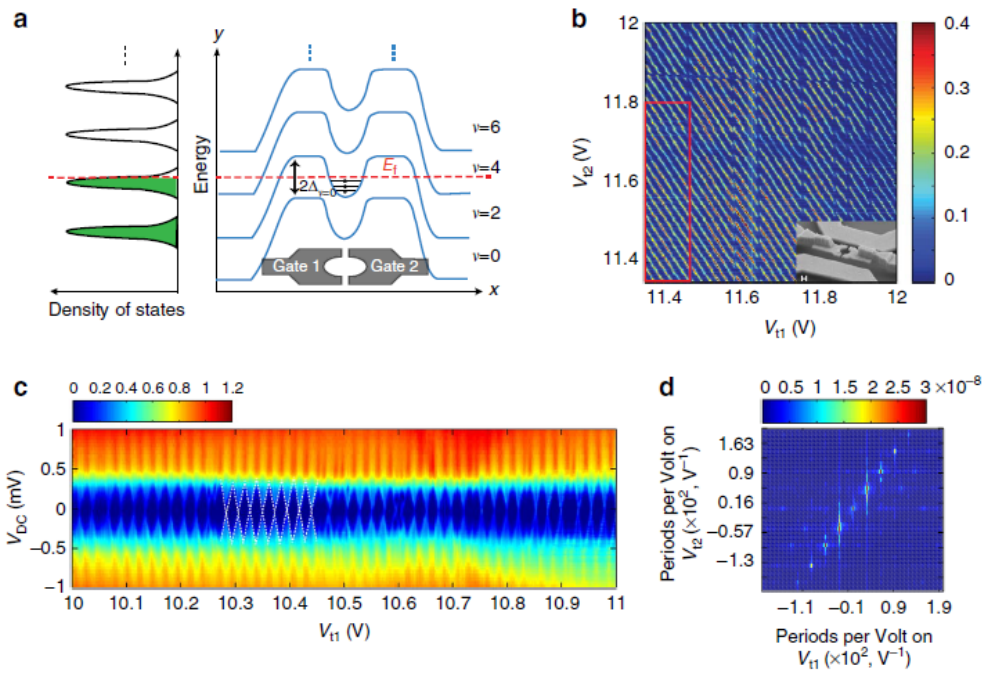

Figure 3.3: **(a)** Quantum dot formation at $B > 0$, illustrated in a cross-sectional cut of energy vs. position. Tunnel barriers are formed using the exchange-enhanced $\nu = 0$ gap, where high resistances due to quantum Hall ferromagnetism are ideal for confinement. An isolated puddle of charge is created by fixing the Fermi energy in the top-gated regions at the middle of the $\nu = 0$ gap while allowing occupation of higher Landau levels elsewhere. *Inset*: Schematic illustration of the top gate geometry for device D1. **(b)** Conductance map (units of e^2/h) of Coulomb blockade oscillations as a function of V_{t1} and V_{t2} in a two top-gate dot (device D1), at fixed back gate voltage $V_b = -15.4$V and $T = 110$ mK. The slopes of the resonances indicate symmetric coupling to the two top gates, as expected for a centrally located dot. As top gate voltages are swept to more positive values, peak amplitude is suppressed, revealing moderate tunnel barrier tunability. *Inset*: Scanning electron micrograph of a device similar to D1. **(c)** Coulomb diamonds are shown in a plot of conductance (units of e^2/h) as a function of V_{t1} and DC bias V_{DC}, where $V_{t2} = 11$ V and $V_b = -14.4$ V are fixed. Symmetric Coulomb diamonds suggests equal tunnel coupling to source and drain leads. The dot charging energy is $E_C \approx 0.4$ meV. **(d)** 2D fast Fourier transform (units of $e^2/h \cdot V$) of the boxed region in (b), revealing the strongly periodic nature of the oscillations and higher harmonics.

p and q are peak index numbers, representing the average peak spacing (black lines in Fig. 3.4c). The dot area extracted from quantized charge tunneling is given by $A = 1/(\beta \cdot \Delta V_b)$, where ΔV_b is the back gate voltage needed to increase dot occupation by one electron (Table 3.1). A comparison of measured dot diameter, $d = 2\sqrt{A/\pi}$, with effective lithographic

diameter, $d_{\text{lith}} = 2\sqrt{A_{\text{lith}}/\pi}$, indicates that d generally exceeds d_{lith}. This is contrary to the reduced dimensions observed in GaAs dots, where smaller dimensions are observed due to depletion [62].

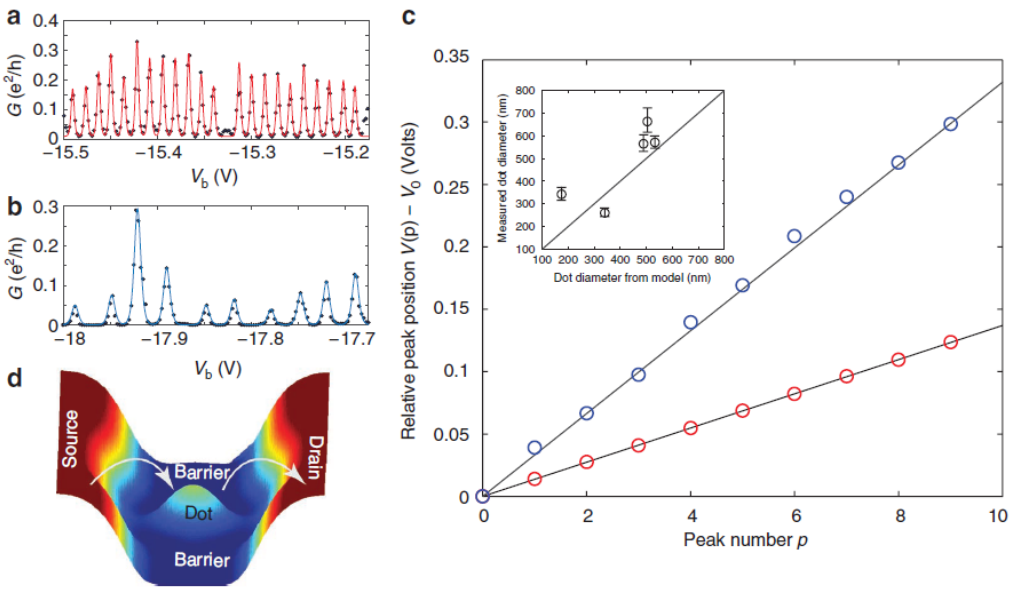

Figure 3.4: **(a)** Coulomb blockade peak conductance as a function of back gate voltage V_{b} observed in device D1 at $B = 5.2$ T. Black points represent data and the red line indicates a functional fit used to extract peak positions. The top gate voltages are fixed at $V_{\text{t1}} = 11.402$ V and $V_{\text{t2}} = 12$ V.**(b)** Coulomb blockade in device D2 at $B = 7$ T. The top gate voltages are fixed at $V_{\text{t1}} = V_{\text{t3}} = 13$ V and $V_{\text{t2}} = V_{\text{t4}} = 12$ V. **(c)** Relative peak position, $V(p) - V_0$, plotted as a function of peak number p for the first 10 peaks of (a) and (b). $V(p)$ is the position of peak p in back gate voltage V_{b}, and V_0 is the position of the first peak ($V_0 = -15.4907$ V and -17.9875 V for plots (a) and (b), respectively). Each black line is a plot of $y(p) = [\frac{1}{9}\sum_{q=0}^{8} V(q+1) - V(q)]p$, where p and q are peak index numbers, representing the average peak spacing for the particular data set. *Inset*: Simulated dot size versus measured size. Error bars represent the range of diameters expected for measured Coulomb blockade peak spacings within one standard deviation of the mean. **(d)** COMSOL simulation of density profile (in arbitrary units) for the lithographic gate pattern of device D4 for top gate voltage $V_{\text{t1}} = V_{\text{t2}} = 12$ V. Electron transport is restricted to resonant tunneling events through the constrictions, indicated by the arrows.

To obtain a better quantitative understanding of the discrepancy between lithographic and measured dot sizes, we use a commercial finite element analysis simulation tool (COMSOL) to calculate the expected dot area for each top gate geometry. The spatial

Table 3.1: Measured quantum dot sizes from Coulomb blockade fits

Device	β, $m^{-2}V^{-1}$	$\langle\Delta V_b\rangle$, mV	St. deviation of ΔV_b	Diameter, $d = 2\sqrt{A/\pi}$
D1	2.85×10^{14}	14.0	1.8	$565(+40/-34)$ nm
D2	3.19×10^{14}	34.1	5.3	$342(+30/-24)$ nm
D3	3.05×10^{14}	68.8	4.2	$260(\pm 8)$ nm
D4	2.71×10^{14}	10.7	1.7	$663(+60/-47)$ nm
D5	2.85×10^{14}	13.7	1.3	$571(+29/-26)$ nm

β: density at 1 V on the back gate. $\langle\Delta V_b\rangle$: average peak spacing. Dot diameter: $d = 2\sqrt{A/\pi}$ for area $A = 1/(\beta \cdot \Delta V_b)$. Error bars in the last column: range of diameters for CB peak spacings within one standard deviation of the mean. See Fig. 3.4a.

carrier density profile is modeled for a fixed top gate potential by solving the Poisson equation assuming a metallic flake in free space (Fig. 3.4d and Supplementary Fig. A.7). This assumption is justified by local compressibility measurements of the $\nu = 0$ state yielding $d\mu/dn = 2 \times 10^{-17} eVm^2$ at 2 T, which translates to a screening of 99% of the applied V_b voltage by the bilayer [18]. Remarkably, one may calculate dot size purely from gate geometry without relying on measured gap parameters. Assuming that charge accumulation in the quantum dot occurs when the carrier density exceeds a fixed cutoff d_0, the dot size is defined as the area bounded by the intersection with the density distribution $f(x, y)$ with the cutoff. Here the cutoff d_0 is placed at the saddle points of the simulated density profile within the constrictions. This condition enables maximal tunneling without loss of confinement, assuming that the tunneling probability into the dot decays exponentially with barrier width. Moving the cutoff to densities far greater than d_0 would pinch off the constrictions and suppress tunneling, while placement far below d_0 would lead to high barrier transparency and eventual loss of confinement. The simulated dot area from this method, plotted in Fig. 3.4c (inset), is simply the area bounded by the closed contour of $f(x, y)$ at fixed density d_0 (Supplementary Fig. A.7). Alternatively, one may calculate dot size by imposing a cutoff equaling the measured gap width (Table 3.2) and accounting for density

offsets due to a displacement of the measurement voltage from the charge neutrality point (see Extended Discussion). The cutoffs extracted by these two models are equivalent to within $\delta n \sim 10^{10}\text{cm}^{-2}$, the carrier density fluctuations due to disorder in our suspended bilayers (Supplementary Fig. A.7) [15].

Table 3.2: Simulated dot sizes obtained from Models 1 and 2

Device	d_0, m^{-2}	d_1, m^{-2}	Diameter (Model 1)	Diameter (Model 2)
D1	7.87×10^{14}	6.81×10^{14}	489 nm	564 nm
D2	1.85×10^{14}	1.45×10^{14}	170 nm	204 nm
D3	7.59×10^{14}	8.34×10^{14}	340 nm	300 nm
D4	4.29×10^{14}	3.90×10^{14}	504 nm	537 nm
D5	6.96×10^{14}	6.59×10^{14}	533 nm	562 nm

Densities d_0 and d_1: cutoff values above which charge accumulation begins in Models 1 and 2. Dot diameter: $d = 2\sqrt{A/\pi}$ for area A. Diameters from Model 2 were computed at maximum offset $d_{offset} = (V_{meas} - V_{CNP})\beta$. See Fig. A.7.

Our model establishes a quantitative link between measured dot size and lithographic geometry and therefore may serve as a design tool for future bilayer nanodevices requiring submicron spatial control. These include double dot systems which form the basis of a spin-based quantum computer [43]. The production of suspended graphene quantum dots also enables study of coupling between quantized electronic and vibrational degrees of freedom [63, 64], with potential applications to nanoelectromechanical devices and the detection of quantized mechanical motion in a membrane [65–68]. Furthermore, the combination of high sample quality with local gating enables study of edge modes that emerge at the interface of broken symmetry quantum Hall states in an environment well-isolated from edge disorder (Supplementary Fig. A.2).

3.7 Methods

Device fabrication

Following mechanical exfoliation of highly oriented pyrolytic graphite crystals, graphene is deposited on a 300 nm thermally grown SiO_2 layer, which covers a doped silicon substrate functioning as a global back gate. Bilayer flakes are identified based on contrast to the substrate with an optical microscope and later verified through quantum Hall data. Cr/Au (3/100 nm) electrodes are defined on selected bilayers using electron beam (ebeam) lithography, thermal evaporation, and liftoff in acetone. A SiO_2 spacer layer approximately 150 nm thick is deposited with ebeam evaporation after a second lithography step. Local top gates are placed over the SiO_2 spacers in a two step ebeam lithography process. First small features that define the tunnel barriers and constrictions are patterned using Cr/Au of thickness 3/75 nm, and thicker support structures constructed of 3/300 nm of Cr/Au that traverse the evaporated SiO_2 step are deposited immediately afterwards. The devices are immersed in 5:1 buffered oxide etch for 90 s and dried in a critical point dryer, which leaves both the graphene and the top gates suspended.

Dot geometries and measurement conditions

We analyze five fully suspended quantum dots with lithographic diameters, $d_{\mathrm{lith}} = 2\sqrt{A_{\mathrm{lith}}/\pi}$, of 150 to 450 nm. Listed here are details on individual sample geometries and measurement conditions. Device D1 is a circular two gate dot with $d_{\mathrm{lith}} = 400$ nm measured at $B = 5.2$ T with the valley polarized $\nu = 0$ gap used for confinement. Device D2 is a circular dot with d_{lith} =150 nm consisting of three main gates with a plunger gate suspended above (see Supplementary Figure A.1). Measurements were conducted at $B = 0$ and 7 T with the E field induced and $\nu = 0$ gaps used for confinement, respectively. Device

D3 is a circular four gate dot with $d_{\text{lith}} = 300$ nm measured at $B = 7$ T. Device D4 is a circular four gate dot with $d_{\text{lith}} = 400$ nm measured at $B = 0$ and 3 T. Device D5 is a two gate elliptical dot with cross sectional lengths of 200 and 250 nm measured at $B = 5$ T. Additional scanning electron microscope (SEM) images of locally gated quantum dot devices are provided in Supplementary Fig. A.1. Top gate labeling for devices D2 and D4 is provided in Supplementary Fig. A.1 and Fig. 3.1, respectively. All measurements are conducted using standard Lockin techniques in a Leiden Cryogenics Model Minikelvin 126-TOF dilution refrigerator. A voltage bias setup is used, where AC excitations ranging from $4 - 80\mu V$ are applied at a frequency of 35.35 Hz with a 100 ms time constant. An electron temperature of $T = 110$ mK is extracted from Coulomb blockade fits.

Despite the complex fabrication process required to make local gated devices, the graphene exhibits high quality as evidenced by symmetry breaking in the quantum Hall regime. Supplementary Fig. A.2 contains Landau fans (measured in device D4 and in a two gate split-gate device) plotted as conductance as a function of back gate voltage V_{b} and magnetic field B, with zero voltage on the top gates. In the split gate device, a map of quantized conductance as a function of the voltages on each split top gate is provided in Supplementary Fig. A.2, where the voltage $V_{\text{b}} = -3$V and field $B = 4$T are held constant. This provides evidence of local control over broken symmetry quantum Hall states in suspended bilayer graphene.

Measured dot size extracted from Coulomb blockade fits

The dot area extracted from quantized charge tunneling is given by $A = 1/(\beta \cdot \Delta V_{\text{b}})$, where ΔV_{b} is the back gate voltage needed to increase dot occupation by one electron and β is the carrier density induced by 1 V on the back gate. The global density to voltage conversion is obtained by fitting Landau level filling factors $\nu = nh/eB$ from bulk quantum

Hall data. The peak spacing $\Delta V_{\mathrm{b}} \equiv V_{\mathrm{b,res}}^{i+1} - V_{\mathrm{b,res}}^{i}$ of a given data set is extracted by fitting each Coulomb blockade oscillation to the conductance expression:

$$G(V_{\mathrm{b}}) = A \cdot \cosh\left(\frac{ea|V_{\mathrm{b}} - V_{\mathrm{b,res}}|}{2.5k_{\mathrm{B}}T}\right)^{-2} \tag{3.1}$$

where e is the electron charge, k_{B} is Boltzmann's constant, T is temperature, A is peak amplitude, $V_{\mathrm{b,res}}$, is the back gate voltage at resonance, and $a = C_{\mathrm{g}}/(C_{\mathrm{l}} + C_{\mathrm{r}} + C_{\mathrm{g}})$ is determined from the slopes of the Coulomb diamonds (C_{g} is capacitance to the back gate and C_{l} and C_{r} are capacitances across the left and right tunnel barriers, respectively). This expression is valid in the regime $\Delta E \ll k_{\mathrm{B}}T \ll e^2/C$, where ΔE is the single particle level spacing. This functional fit to the data is shown explicitly in Fig. 3.4a,b. Coulomb blockade data from an additional device is provided in Supplementary Figure A.4.

3.8 Extended Discussion

Even-odd effects

At zero magnetic field, the presence of a four-fold degeneracy due to spin and valley symmetries may affect the Coulomb blockade periodicity (at high electric fields in the quantum Hall regime, both spin and valley degeneracies should be broken). In device *D4*, an even-odd effect is visible in a Coulomb blockade plot as a function of V_{t12} at fixed $V_{t34} = 9.27\mathrm{V}$ and $V_b = -10.7\mathrm{V}$ (Supplementary Fig. A.5). This is consistent with the presence of a two-fold degeneracy, where the constant interaction model yields electron addition energy $E_{add} = E_C$ for N odd and $E_{add} = E_C + \Delta E$ for N even (for charging energy E_C and orbital energy spacing ΔE) because electrons of opposite index can occupy a single orbital state [40, 41]. Although the application of a large electric field breaks sublattice symmetry, spin and valley degeneracies remain intact, so an explanation of our observation

of a two-fold rather than four-fold effect remains an open question. Also, the theoretical estimate of ΔE based on device geometry is larger than the measured value; this discrepancy cannot be explained by a single particle picture and requires further investigation.

Model 1: Cutoff defined by constriction saddle points

We first discuss simulation of the spatial density profile for each quantum dot, as shown in Fig. 3.4d, which is relevant to the final two sections of the Extended Discussion. COMSOL Multiphysics, a commercial finite element analysis simulation tool, is used to model the spatial carrier density profile for a fixed top gate potential by solving the Poisson equation, $\nabla^2 V = -\rho/\varepsilon_0$. First the lithographic top gate pattern, designed using TurboCAD, is imported into COMSOL and placed in a parallel plane defined 150 nm above the graphene flake. The flake is assumed to be a two dimensional metallic plate, which is justified by local compressibility measurements of the $\nu = 0$ state yielding $d\mu/dn = 2 \times 10^{-17} eVm^2$ at 2 T, which translates to a screening of 99% of the applied V_b voltage by the bilayer (for $dn = 1.5 \times 10^9\ cm^{-2}$) [42]. A fixed potential matching the experimental value at which Coulomb blockade oscillations appear is assigned to the top gates, while the flake is grounded. The perpendicular electric field component, $E_z(x, y)$, is solved in a plane 5 nm above the flake. The approximate carrier density profile is given by the function $f(x, y) = e \cdot E_z(x, y)/\varepsilon_0$ up to a constant offset. This is because the graphene screens all in-plane electric fields. A contour plot representing the simulated spatial density profile in device *D4* at a top gate voltage of 12 V is presented in Supplementary Figure A.7.

In the first modeling approach, whose results are presented in Fig. 3.4c, one may calculate dot size purely from gate geometry without relying on measured gap parameters. Assuming that charge accumulation in the quantum dot occurs when the carrier density exceeds a fixed cutoff d_0, the dot size is defined as the area bounded by the intersection with

the density distribution $f(x, y)$ with the cutoff. Here the cutoff d_0 is placed at the saddle points of the simulated density profile within the constrictions. This condition enables maximal tunneling without loss of confinement, assuming that the tunneling probability into the dot decays exponentially with barrier width. Thus, the simulated dot area computed by this method is simply the area bounded by the closed contour of $f(x, y)$ at fixed density d_0 (Supplementary Fig. A.7a).

The model is used to estimate the extent to which dot size should change in response to a changing top gate voltage. The dot diameter, $d = 2\sqrt{A/\pi}$, for sample *D2* is computed to be 170 nm at top gate voltage $V_t = 9$ V and 173.5 nm at $V_t = 13$V. This 3.5 nm increase in diameter, a 2 percent change, over a 4 V range is substantially smaller than the experimental error bars due to fluctuations in peak spacing (Fig. 3.4). This prediction is consistent with the overall experimental observation of an approximately constant dot size over the measurement ranges presented in this paper.

Model 2: Cutoff determined from measured $\nu = 0$ gap and offset from charge neutrality point

In the second modeling approach, we determine quantum dot dimensions using both the simulated density distribution and experimental gap measurements. First the spatial density profile induced by the top gates, $f(x, y)$, is modeled using COMSOL following the procedure described in the preceding section of the Extended Discussion. To determine the quantum dot size from the density profile, we impose a cutoff d_1 determined by the width of the gap ($\nu = 0$ or E field induced) above which charge accumulation begins. Explicitly, $d_1 = (V_+ - V_-)\beta$, where V_+ and V_- are the positive and negative back gate voltages at which a plot of conductance versus V_b intersects $1e^2/h$. Additionally we account for overall offsets in density due to a displacement of the measurement voltage from the

charge neutrality point. This offset is given by $d_{offset} = (V_{meas} - V_{CNP})\beta$, where V_{meas} is the measured back gate voltage at which Coulomb blockade oscillations appear, and V_{CNP} is the measured back gate voltage at which the charge neutrality point appears at $B = 0$ when the top gates are fixed at the potential defined in the density profile simulation. Thus, the spatial density profile with proper offsets included is $g(x, y) = f(x, y) - d_{sat} + d_{offset}$, where d_{sat} is the saturating value of $f(x, y)$ deep within the tunnel barriers defined by the top gates. Physically d_{sat} is the offset in carrier density induced by the back gate that places the Fermi energy at the center of the bandgap. Similar to Model 1, the simulated dot area computed by this method is the area bounded by the contour lines of $g(x, y)$ at fixed density d_1. Results of Models 1 and 2 are presented in Table 3.2 and Supplementary Figure A.7.

Chapter 4

Spatially resolved edge currents in monolayer and bilayer graphene

4.1 Overview

Extreme nonclassical forms of electronic transport realized in graphene by exploiting the light-like properties of carriers in this material are of keen interest for nanoscience research [69–76]. In this vein, finding ways to confine and direct electronic waves through nanoscale streams and streamlets, unimpeded by the presence of other carriers, has remained a grand challenge [77–80]. Inspired by guiding of light in fiber optics, here we demonstrate a route to engineer such a flow of electrons using a new technique for mapping currents at submicron scales. We employ real-space imaging of current flow in graphene to provide direct evidence of confinement of electron waves at the edges of a graphene crystal near charge neutrality. This is achieved by using superconducting interferometry in a graphene Josephson junction and reconstructing the spatial structure of conducting pathways using Fourier methods [24]. The observed edge currents arise from coherent guided wave states,

confined to the edge by band bending and transmitted as plane waves. As an electronic analog of photon guiding in optical fibers, the observed states afford new nonclassical means for information transduction and processing at the nanoscale.

4.2 Guided-wave electronic states in graphene

Electrons in Dirac materials such as graphene can be manipulated using external fields that control electron refraction and transmission in the same way that lenses and optical elements manipulate light [69, 70, 74, 75]. Several of the key ingredients, including phase-coherent Klein transmission and reflection [71–73], ballistic transport [76] and transverse focusing on micrometer scales [81], have already been established. One promising yet unexplored direction, which we investigate here, is the quasi-1D confinement of electrons in direct analogy to refraction-based confinement of photons in optical fibers. Electronic guided modes formed by a line gate potential, while discussed in the literature [77–80], have so far evaded direct experimental realization. Extending the fiber optics techniques to the electronic domain is key for achieving control of electron waves at a level comparable to that for light in optical communication systems.

Rather than pursuing the schemes discussed in Refs. [77–80], here we explore modes at the graphene edges. The atomically sharp graphene edges provide a natural vehicle for band bending near the boundary which then confines the electronic waves in the direction transverse to the edge. The resulting guided "fiber-optic" modes are situated outside the Dirac continuum (see Fig. 4.1a,b), propagating along crystal edge as plane waves and decaying into the bulk as evanescent waves. This approach to carrier guiding is particularly appealing because of the ease with which band bending at the graphene edge can be realized, as well as because there is no threshold for fiber-optic states to occur:

they are induced by an edge potential of either sign, positive or negative, no matter how weak (see discussion below and in the Extended Discussion). The presence of such guided modes enhances the density of current-carrying states at the edge. The effects of electron confinement and guiding are strongest near charge neutrality where the edge potential is unscreened, while uniform behavior is recovered away from neutrality (see Fig. 4.1c and Fig. 4.5).

The edge currents associated with guided states, anticipated at zero magnetic field, have so far eluded experimental detection due to the challenge of imaging current with submicron spatial resolution. In particular, scanning tunneling spectroscopy (STS) images density of states but not current flow [82,83], while macroscopic conductivity cannot distinguish the edge and bulk contributions [84, 85]. With this motivation, we developed a technique to spatially image electric current pathways and applied it to high-mobility graphene. We employ superconducting quantum interferometry in a graphene Josephson junction to reconstruct the spatial structure of the electronic states which transmit supercurrent, which allows edge and bulk contributions to be disentangled [24, 86].

4.3 Experiment: spatial imaging of current flow using Josephson interferometry

Our approach employs gated Josephson junctions consisting of graphene coupled to superconducting titanium/aluminum electrodes (Fig. 4.1d). A gate electrode is used to tune the carrier density, n, in the graphene. In order to access the intrinsic properties of graphene at densities near charge neutrality, flakes are isolated from substrate-induced disorder through placement on thin hexagonal boron nitride (hBN) substrates [87]. A total of four bilayer and one monolayer devices are investigated, all of which exhibit similar

behavior (Table 4.1). Measurements of the AC voltage drop dV across the junction in response to an AC current modulation dI were conducted using lockin techniques in a dilution refrigerator at 10 mK, well below the critical temperature of Al. Figures 4.1e-h exemplify transport data from one of the bilayer devices. Upon sweeping DC current bias I_{DC}, a sharp transition in resistance between dissipationless and normal metal behavior appears at a critical current I_c, a transport signature of the Josephson effect (Fig. 4.1e,f).

Table 4.1: List of device dimensions for graphene Josephson junctions

Device	L (nm)	W (nm)	Aspect ratio, L/W	Contact width (nm)
BL1	250	1200	0.208	400
ML1	300	1200	0.25	300
BL2	300	800	0.375	400
BL3	350	1200	0.292	600
BL4	250	900	0.278	400

L and W refer to junction length and width, respectively, as labeled in Fig. 4.1d of the main text. Contact width refers to the size of the superconducting Ti/Al electrodes in the direction perpendicular to W. BLx and MLx refer to bilayer and monolayer graphene devices, respectively.

We obtain real-space information by applying a magnetic flux Φ through the junction area, which induces a position-dependent superconducting phase difference parallel to the graphene/contact interface [23]. As a result, the critical current I_c exhibits interference fringes in B field (Figure 4.1e). The measured interference patterns feature well defined nodes, which indicates the absence of field inhomogeneity such as that due to vortices [88]. The critical current I_c can be expressed as the magnitude of the complex Fourier transform of the current density distribution $J(x)$, providing a simple and concise description of our system. That is, $I_c = |\mathcal{I}_c(B)|$, where

$$\mathcal{I}_c(B) = \int_{-W/2}^{W/2} J(x) \cdot e^{2\pi i L B x/\Phi_0} dx \tag{4.1}$$

where $\Phi_0 = h/2e$ is the flux quantum, h is Planck's constant, e is the elementary charge, W is the width of the flake, and L is the distance between contacts (Fig. 4.1d). Here, following the conventional treatment for wide junctions ($L \ll W$), we ignore the y dependence. The spatial distribution of supercurrent thus dictates the shape of the interference pattern [23, 24, 49].

The results obtained with this technique show strikingly different behavior at high and low carrier densities. We observe the conventional uniform-current behavior at high density, $I_c(B)/I_c(0) \sim |\sin(\pi\Phi/\Phi_0)/(\pi\Phi/\Phi_0)|$, which mimics single-slit Fraunhofer diffraction (Fig. 4.1e). Defining features of such interference include a central lobe of width $2\Phi_0$ and side lobes with period Φ_0 and decaying $1/B$ amplitude. However, near the Dirac point, our results exhibit a striking departure from this picture and show a two-slit "SQUID-like" interference (Fig. 4.1f) [89]. Such behavior arises when supercurrent is confined to edge channels and is characterized by slowly decaying sinusoidal oscillations of period Φ_0. Importantly, these two regimes are easily distinguishable without much analysis by the width of the central lobe, which is twice as wide for the uniform case as compared to the case of edge flow.

The real-space current distribution can be obtained by inverting the relation in Eq.(1) with the help of the Fourier techniques of Dynes and Fulton [24] (see Extended Discussion). The resulting current density map reveals strong confinement of supercurrent to the edges of the crystal near the Dirac point (Fig. 4.1h), a robust experimental feature seen in all five devices. The width of the edge channel, extracted quantitatively from Gaussian fits, is on the order of the electron wavelength ($\sim$ 200 nm) and consistent across multiple samples. This value is likely an upper bound because the peak width is manifested in the decay envelope of the interference pattern, external factors that suppress the critical current amplitude at high B, such as activation and decay of the Al superconducting gap, may also

contribute to peak broadening. At high electron density, a conventional Fraunhofer-like behavior is recovered (Fig. 4.1e), suggesting a uniform distribution of supercurrent (Fig. 4.1g). A more numerically expensive Bayesian estimation of the current distribution produces current maps and standard error estimates that agree with the Fourier techniques (see Extended Discussion and Fig.4.6 within).

By tuning carrier concentration with a gate electrode, our measurements reveal coexistance of edge and bulk modes at intermediate densities. As illustrated in Fig.4.2, our monolayer graphene device exhibits SQUID-like quantum interference through charge neutrality, giving the spatial image of supercurrent that confirms edge-dominated transport (Fig. 4.2a-c,f). As density is increased, bulk current flow increases monotonically and crosses over to mostly uniform flow across the sample (Fig. 4.2d), signified by conventional Fraunhofer-like interference at high electron density (Fig. 4.2e). To track the evolution of edge and bulk currents with density, line cuts of the individual contributions are provided in Figure 4.2e, where the gate voltage corresponding to the charge neutrality point is identified as a dip in the current amplitude. Notably, raw interference near the Dirac point (Fig. 4.2e) and at high electron concentration (Fig. 4.2f) exhibit the salient features that distinguish edge-dominated from bulk-dominated transport, including a width of φ_0 versus $2\varphi_0$ of the central lobe, as well as Gaussian versus $1/B$ decay of the lobe amplitudes for low and high densities, respectively.

Similarly, we systematically explore the correspondence between edge and bulk flow in bilayer graphene and detect boundary currents in the presence of broken crystal inversion symmetry (Fig. 4.3). As the Fermi energy approaches the Dirac point from the hole side, the bulk is suppressed faster than the edge, leading to emergence of robust

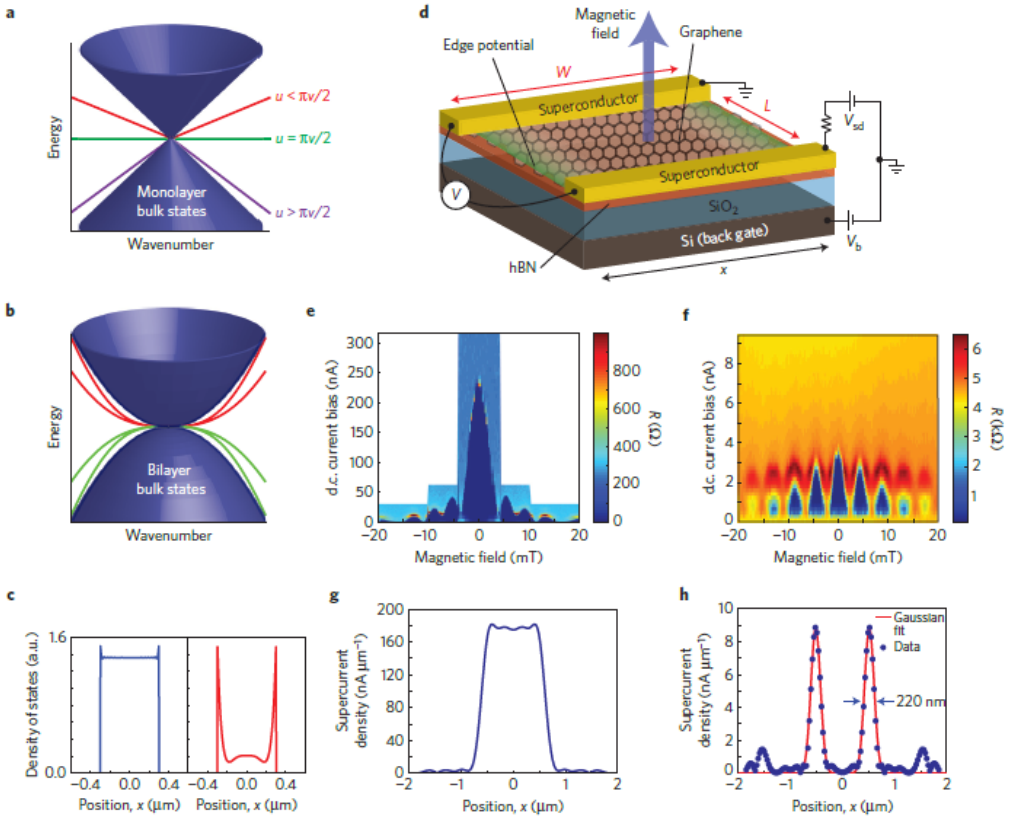

Figure 4.1: **(a, b)** Guided edge modes induced by an intrinsic band bending near crystal boundary, for single-layer and bilayer graphene (schematic). Mode frequencies positioned outside the Dirac continuum ensure mode decoupling from the bulk states. In a bilayer, the modes occur in pairs [*green and red curves*: dispersion for positive and negative potential strength, respectively]. **(c)** The guided modes are manifested through peaks in the density of current-carrying states at the boundaries, prominent near charge neutrality (*red*: $n = 0.05 \times 10^{11} cm^{-2}$; *blue*: $n = 2.5 \times 10^{11} cm^{-2}$). **(d)** Schematics of superconducting interferometry in a graphene Josephson junction. A flux is threaded through the junction area to produce interference patterns, as current bias V_{sd} is applied between the contacts and the voltage across the device is recorded. Carrier density n is tuned by a gate voltage V_b. **(e, f)** The interference pattern is of a single-slit type at high density, turning into a two-slit interference near neutrality (device $BL1$). **(g, h)** Current flow, extracted from the interference data using Fourier techniques, is uniform at high density and peaks at the edges close to neutrality.

edge currents near zero carrier density (Fig. 4.3a,b). In this device, current distributions are not plotted at the immediate Dirac point due to suppression of proximity-induced superconductivity at high normal state resistances. We note that the range in hole density

over which the bulk contribution is recovered varies in different devices. Further, application of an interlayer electric field E breaks crystal inversion symmetry and induces a bandgap [3, 90], manifested as a gate-tunable insulating state at the Dirac point (Fig. 4.3c,d). In this regime, conductance is mediated by edge currents that enclose the bulk, even in the presence of a gap (Fig. 4.3e,f).

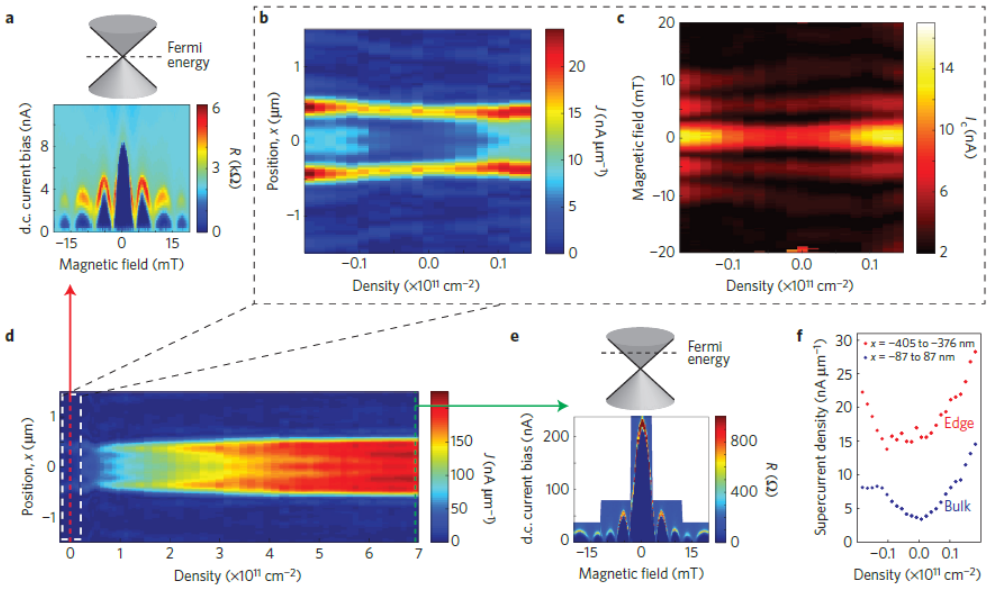

Figure 4.2: **(a)** Edge-dominated SQUID-like interference pattern at neutrality in device $ML1$ ($n = 2.38 \times 10^9$ cm^{-2}). **(b, c)** Real-space image of current flow confined to the boundaries over a range of densities near neutrality, shown alongside with the raw interference data (corresponding to the white box in (d)). **(d)** A real-space map of current flow as a function of electron concentration reveals coexistence of edge and bulk modes at intermediate densities. Over the entire scan, the full range of carrier modulation extends into the high 10^{11} range cm^{-2}. **(e)** Conventional Fraunhofer pattern for uniform current flow at high electron density ($n = 7 \times 10^{11}$ cm^{-2}). **(f)** Comparison of current amplitudes along the edge (red) and bulk (blue) from panel (c). Current flow is edge-dominated near neutrality. Minima for both contributions coincide in n, indicating that a positional edge/bulk density offset is not present.

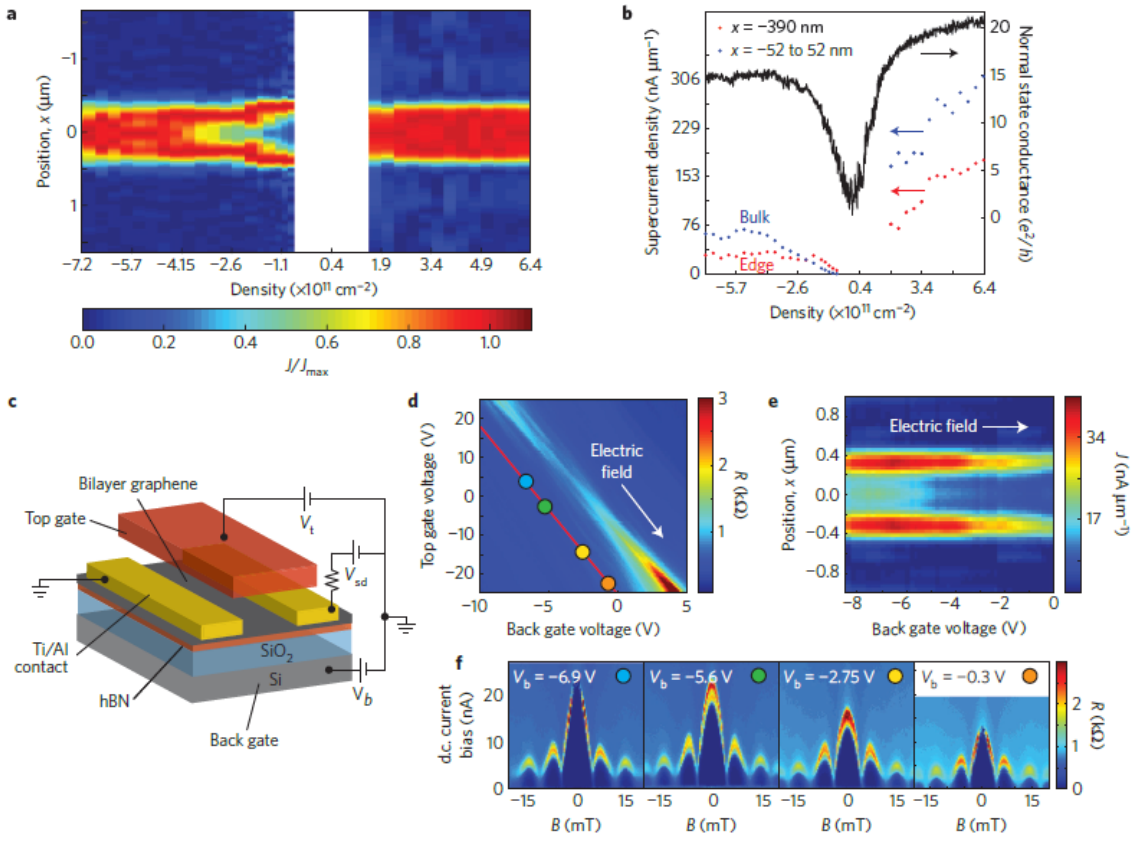

Figure 4.3: **(a)** Spatially resolved supercurrent map in device $BL2$, in a normalized plot of $J(x)/J_{max}(x)$. Edge-dominated transport occurs near charge neutrality, while an increasing bulk contribution is tuned with carrier concentration. **(b)** Comparison of current amplitudes along the edge (red) and through the bulk (blue) from panel (a). Enhanced edge currents are prominent at neutrality, whereas a uniformly distributed flow is recovered at high densities. The normal state conductance $G(e^2/h)$ *vs.* carrier density is also shown (black). **(c)** Measurement schematic for superconducting interferometry in a dual-gated bilayer graphene Josephson junction. A dual-gated device consists of bilayer graphene flake on hBN with a suspended top gate, where application of voltages V_t and V_b on the top and back gates enables independent control of the transverse electric field E and carrier density n. **(d)** Resistance map as a function of V_b and V_t for bilayer $BL4$. Enhanced resistance at high E fields indicates the emergence of a gate-tunable insulating state due to broken crystal inversion symmetry. **(e)** Spatially-resolved boundary currents as a function of E field. The vertical axis is a trace along the red path labeled in (b). **(f)** Sequence of Fraunhofer measurements at various locations on the current map in panel (e).

As a simple model of electronic fiber-optic states we consider massless Dirac particles in graphene monolayer in the presence of a line potential:

$$H = v\boldsymbol{\sigma}\cdot\boldsymbol{p} + V(x), \tag{4.2}$$

where σ_i are pseudospin Pauli matrices and $v \approx 10^6\,\mathrm{m/s}$. We seek plane-wave solutions of the Schrödinger equation, $\psi(x,y) = e^{iky}\varphi(x)$, where k is the wavevector component along the line and $\varphi(x)$ is a two-component spinor wavefunction depending on the transverse coordinate. This problem can be tackled by a matrix gauge transformation $\psi(x) = U(x)\tilde{\psi}(x)$, which eliminates the potential $V(x)$ and generates a mass term in the Dirac equation. Namely, $U(x) = e^{-i\theta(x)\sigma_x}$ with $\theta(x) = \frac{1}{\hbar v}\int_0^x V(x')dx'$ yields

$$\tilde{H} = U(x)HU^{-1}(x) = \hbar v[-i\sigma_x\partial_x + k\sigma_y\cos 2\theta(x) - k\sigma_z\sin 2\theta(x)]. \tag{4.3}$$

As a simple example, we consider the case of an armchair edge, for which the problem on a half plane for carriers in valleys K and K' is equivalent to the problem on a full plane for a single valley. Applying the above method to a potential localized in an interval $-d < x < d$ and focusing on the long-wavelength modes such that $kd \ll 1$, we can use a step approximation $\theta(x) \approx (u/2v)\,\mathrm{sgn}\,(x)$ with the parameter $u = \frac{1}{\hbar}\int_{-d}^{d} V(x')dx'$. We arrive at the seminal Jackiw-Rebbi problem for a Dirac equation with a mass kink

$$\tilde{H} = \hbar v(-i\sigma_x\partial_x + \sigma_y\tilde{k} + \sigma_z m(x)), \tag{4.4}$$

where $\tilde{k} = k\cos(u/v)$, $m(x) = -k\sin(u/v)\,\mathrm{sgn}\,(x)$. The Jackiw-Rebbi problem can be solved directly and explicitly [91], yielding guided-wave states as products of the zero-mode state found from $\tilde{H}$ for $\tilde{k} = 0$ and the plane wave factors e^{iky}. The energies of these states

are simply $\varepsilon = \eta\hbar v\tilde{k}$ with the sign $\eta = \mathrm{sgn}\,(m(0^+) - m(0^-))$. This gives a linear dispersion $\varepsilon = \hbar\tilde{v}|k|$ with $\tilde{v} = v\cos(u/v)\mathrm{sgn}\,(\sin(u/v))$. Since $|\tilde{v}| < v$, for each k the energies of these states lie outside the bulk continuum $|\varepsilon| \geq \hbar v|k|$ (see Fig. 4.1a). Decoupling from the bulk states ensures confinement to the region near the $x = 0$ line. The connection with the theory of zero modes renders robustness to our confinement mechanism. Similar guided-wave states are obtained for an edge potential in graphene bilayer (see Fig. 4.1b).

In Figure 4.4, we compare supercurrent density measurements with a theoretical prediction for density of states. Current density traces $J(x)$ measured in bilayer device $BL3$ at different densities have a strong edge component near neutrality, gradually evolving to the bulk flow away from neutrality. Traces of the density of states, obtained from the above model, exhibit qualitatively similar behavior (Fig. 4.4b). For the simulation, a delta function potential approximation was used with the best-fit value $\hbar u = 0.7$ eV·nm (see Extended Discussion).

Another key feature borne out by the above model is the robustness of the guided states in the presence of edge disorder. Indeed, since the lengthscales defined by the evanescent waves are on the order of electron wavelength λ, the resulting modes are weakly confined to the edge at low carrier density. Such modes can naturally decouple from the short-range edge disorder by diffracting around it. In particular, our analysis of monolayer graphene yields the mode damping that quickly vanishes at long electron wavelengths near charge neutrality, scaling as $\gamma(k) \sim k^2$ (see Extended Discussion section). This resembles the behavior of optical guided states in so-called "weakly-guiding" optical fibers, where a similar suppression of disorder scattering occurs due to evanescent waves diffracting around edge disorder.

One appealing aspect of the fiber-optic model is that it can naturally accommodate a wide range of different microscopic physical mechanisms discussed theoretically in the

literature [91–95] that may produce an edge potential. Examples include pinning of the Fermi energy to the low-energy states due to broken A/B sublattice symmetry [93–95], density accumulation caused by dangling bonds or trapped charges at the boundaries, or electrostatics [91, 92]. The competition of these effects can produce a complex dependence of the edge potential $V(x)$ on carrier density. Pinpointing the precise microscopic origins of the edge potential requires further study.

To the best of our knowledge, the fiber-optic modes is among the simplest models fully consistent with the observations. While edge density accumulation can influence the edge potential and in principle also support guided edge currents, the fact that the charge neutrality points for both edge and bulk roughly coincide in density n suggests an absence of a positional charge imbalance on a large scale (Fig. 4.2f). In addition, edge-dominated current flow is observed near the Dirac point but not at higher densities, behavior not expected for strong edge doping. Explanations involving electron-hole puddles are excluded by the reproducibility of edge currents with width on the order of electron wavelength across many samples, as well as the observation that edge currents tend to be stronger in clean samples with ballistic Fabry-Pérot interference [96] (see Fig.4.9 for normal state characterization of the graphene). Large charge inhomogeneities across the sample would suppress Fabry-Pérot interference and are thus unlikely.

Lastly, it is widely known that the A/B sublattice imbalance for broken bonds at the edge can lead to edge modes in pristine graphene at neutrality. Such dispersing zero-mode states can exist even in the absence of a line potential, forming edge modes for an atomically perfect zigzag edge [93–95]. However, our simulations for disordered edge show that these states are highly localized on the disorder length scale, and also that edge roughness induces strong scattering between the states at the boundary and in the bulk, which hinderds ballistic propagation. Similarly, valley Hall currents predicted at the

boundaries of a gapped bilayer due to momentum-space Berry curvature of the bands [97,98] are susceptible to disorder scattering at the boundaries. We therefore conclude that such states are unlikely to contribute to the observed boundary currents.

Our measurements establish that edge currents are present in graphene even at zero magnetic field, near the Dirac point. The observed edge currents are linked to electronic guided-wave states formed due to band bending at the edge, demonstrating confinement of electron waves at a level comparable to that for light in photonic systems. This defines a new mode for transmission of electronic signals at the nanoscale. We also anticipate this work will inspire more detailed investigations of boundary states in graphene and other materials. Such capabilities are also of keen interest due to the predicted topological nature of edge states along stacking domain boundaries in bilayer graphene [99, 100].

4.4 Extended Discussion

4.4.1 Modeling electronic guided modes

Main results

A realistic model of supercurrent-carrying states in graphene SNS junctions should account for several microscopic effects. This includes, in particular, the details of transport through the NS interfaces, the realistic edge potential profile due to band bending near graphene edge, and the effects of disorder. Since treating all these issues simultaneously and on equal footing may be challenging, we use a simplified model. First, we completely ignore the effects of induced superconductivity, focusing on the normal metallic state of pristine graphene. Second, we consider a clean system and account for disorder scattering perturbatively at the end. Third, since all the states in a clean system, being delocalized, are capable of carrying supercurrent, we resort to evaluating the density of states (DOS) taking

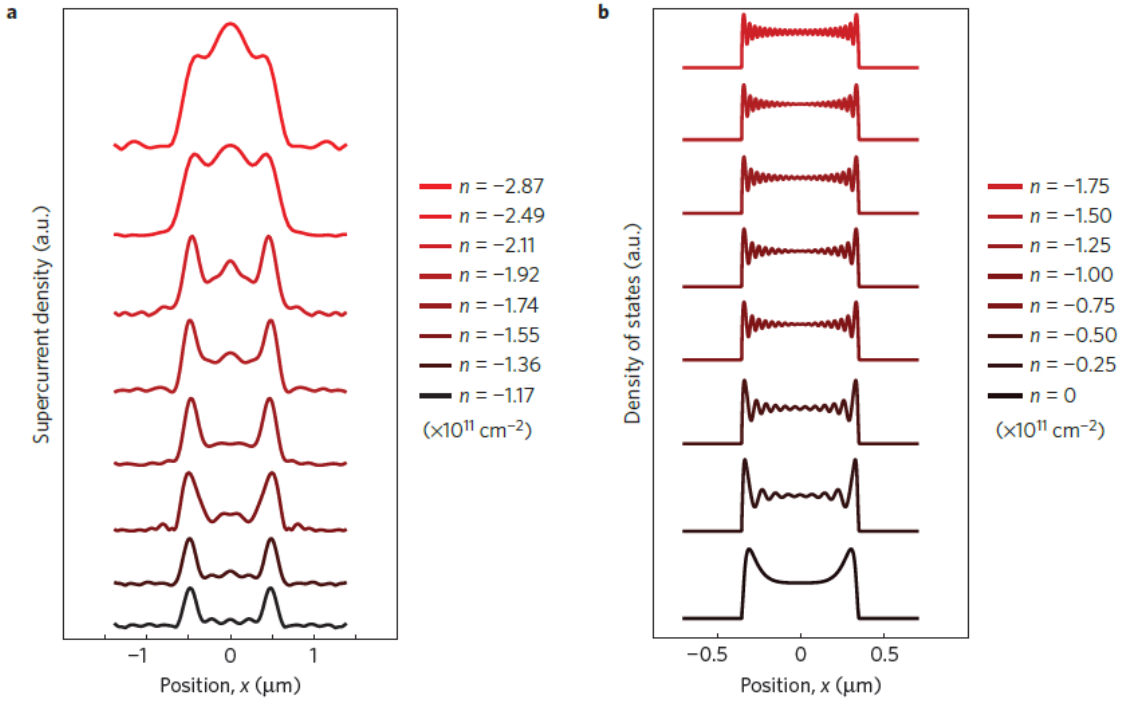

Figure 4.4: **(a)** Real-space maps of measured current flow $J(x)$ in bilayer device $BL3$ at fixed carrier densities on the hole side, showing edge currents near the Dirac point and a continuous evolution towards bulk flow. **(b)** Theoretical plot of spatially resolved density of states in bilayer graphene at fixed carrier densities for edge waveguide model. For the simulation, an effective delta function potential approximation is used with the best-fit value $\hbar u = 0.7$ eV·nm (see Extended Discussion). In each density of states simulation, the value of lambda is always consistent with the carrier density specified for that line cut. Band mass of bilayer graphene is taken $0.028m_e$ where m_e is electron mass.

it to reflect on the current-carrying capacity of the system. Naturally, such an approach should be used with caution for disordered systems in which some states are localized, and therefore can contribute to DOS but not to supercurrent. However, since the states in a clean system are of a plane wave character, contributing to current with the weights given by their occupancies and all possessing a roughly similar current-carrying capacity, we adopt the DOS-based approximation on the merit of its simplicity.

Below we focus on the two cases of interest: the monolayer graphene (MLG) and

bilayer graphene (BLG). States in MLG are described by the massless Dirac Hamiltonian

$$H_0 = v \begin{pmatrix} 0 & p_x - ip_y \\ p_x + ip_y & 0 \end{pmatrix} = v\sigma_1 p_x + v\sigma_2 p_y \tag{4.5}$$

with $v \approx 10^6$m/s the carrier velocity and σ_1, σ_2 the pseudospin Pauli matrices. States in BLG are described by the Hamiltonian

$$H_0 = \frac{1}{2m^*} \begin{pmatrix} 0 & (p_x - ip_y)^2 \\ (p_x + ip_y)^2 & 0 \end{pmatrix} = \frac{1}{2m^*} \Big\{ \sigma_1 (p_x^2 - p_y^2) + 2\sigma_2 p_x p_y \Big\} \tag{4.6}$$

with the band mass value $m^* = 0.028\, m_e$.

As stated above, we use spatially resolved DOS as a measure of current-carrying capacity of the system. We analyze the quantity

$$N(\mu, \mathbf{r}) = \frac{dn(\mathbf{r})}{d\mu}, \quad n(\mathbf{r}) = \langle \psi^\dagger(\mathbf{r}) \psi(\mathbf{r}) \rangle, \tag{4.7}$$

where n is the total carrier density and μ is the chemical potential. Below we evaluate DOS as a function of position and energy, focusing on the characteristic features due to the guided modes.

Our analysis of the spatial dependence of DOS and other related quantities is facilitated by the following observations. First, as discussed in the main text, the problem of guided states on a halfplane $x > x_0$ near the edge $x = x_0$ in MLG can be mapped onto a similar problem on a full plane by accounting for the states in valleys K and K' mixing at the edge. This mapping is particularly transparent for the armchair edge, where the boundary condition for the spinor wavefunctions in the two valleys is simply $\psi_K + \psi_{K'} = 0$. In this case, one can see that the two-valley half-plane problem is mathematically equivalent to the

problem posed on a full plane for particles in just one valley, provided the line potential for the latter problem is taken to be a sum of the original edge potential and its mirror-reflected double, $V(x > x_0) \rightarrow V(|x - x_0|)$.

Second, the states with the wavelengths larger than the edge potential width can be described by treating the potential in a delta function approximation. In that, a realistic microscopic potential $V(x)$ is replaced by a delta-function pseudopotential

$$\tilde{V}(x) = \hbar u \delta(x - x_0), \quad u = \frac{1}{\hbar} \int V(x')dx' \tag{4.8}$$

where x_0 is the edge position. Here we parameterized the effective potential strength by the quantity u which has the dimension of velocity. A system of width w with two parallel edges positioned at $x_0 = \pm w/2$ can therefore be described by a Hamiltonian in the full plane $-\infty < x < \infty$, $-\infty < y < \infty$:

$$H = H_0 + \hbar u \delta(x + w/2) + \hbar u \delta(x - w/2), \tag{4.9}$$

where H_0 is the 2×2 Dirac Hamiltonian for carriers with one spin/valley projection in MLG or BLG, see Eqs.(4.5),(4.6).

Lastly, taking into account that for for relevant densities $n \sim 10^{11}$ cm^{-2} typical electronic wavelength values $\lambda \sim n^{-1/2} \approx 50$ nm are much smaller than the distance between edges $w = 800 - 1200$ nm, we can represent DOS as a sum of partial contributions

$$N(\mu, x) = N_0(\mu) + N_1(\mu, x - w/2) + N_1(\mu, x + w/2). \tag{4.10}$$

Here $N_0(\mu)$ is the DOS of a uniform infinite system with fixed spin/valley projection,

$$N_0(\mu) = \frac{|\mu|}{2\pi\hbar^2 v^2} \text{ (MLG)}, \qquad N_0(\mu) = \frac{m^*}{2\pi\hbar^2} \text{ (BLG)} \tag{4.11}$$

and $N_1(\mu, x \pm w/2)$ are the contributions to DOS from a pair of delta-function line potentials placed at $x = \pm w/2$.

Below we derive an exact expression for DOS perturbed by a delta function. For MLG we find

$$N_1(\varepsilon, x) = \frac{4u}{\pi\hbar^2} \operatorname{Im} \int \frac{dp}{2\pi} \frac{p^2 e^{-2\kappa_{\varepsilon,p}|x|/\hbar}}{\kappa_{\varepsilon,p}\big[4\varepsilon u + (4v^2 - u^2)\kappa_{\varepsilon,p}\big]} \qquad \text{(MLG)} \tag{4.12}$$

where $\kappa_{\varepsilon,p} = \sqrt{p^2 - (\varepsilon/v)^2}$. For BLG we find

$$N_1(\varepsilon, x) = -\frac{2}{\pi\hbar^2 u} \operatorname{Im} \int \frac{dp}{2\pi} \frac{[1 + F_0(0)][F_0^2(x) + F_1^2(x) + F_2^2(x)] - 2F_1(0)F_0(x)F_1(x)}{[1 + F_0(0)]^2 - F_1^2(0)} \qquad \text{(BLG)} \tag{4.13}$$

where we introduced the notation

$$F_0(x) = \frac{m^* u}{2} \left[\frac{1}{\kappa^-_{\varepsilon,p}} e^{-\kappa^-_{\varepsilon,p}|x|} - \frac{1}{\kappa^+_{\varepsilon,p}} e^{-\kappa^+_{\varepsilon,p}|x|} \right] \tag{4.14}$$

$$F_1(x) = \frac{m^* u}{2} \left[\frac{1}{\kappa^-_{\varepsilon,p}} \left(1 - \frac{p^2}{m^*\varepsilon}\right) e^{-\kappa^-_{\varepsilon,p}|x|} + \frac{1}{\kappa^+_{\varepsilon,p}} \left(1 + \frac{p^2}{m^*\varepsilon}\right) e^{-\kappa^+_{\varepsilon,p}|x|} \right] \tag{4.15}$$

$$F_2(x) = -\frac{pu}{2\varepsilon} \left(e^{-\kappa^-_{\varepsilon,p}|x|} - e^{-\kappa^+_{\varepsilon,p}|x|} \right) \tag{4.16}$$

where $\kappa^\pm_{\varepsilon,p} = \sqrt{p^2 \pm 2m^*\varepsilon}$.

In the expressions given in Eq.(4.12) and Eq.(4.13) the energy ε is taken to have an infinitesimal positive imaginary part, which is essential for handling the poles in the denominators due to the guided modes. After evaluating the integral, ε must be replaced by the chemical

potential, $\varepsilon = \mu$. The spatial dependence of DOS in MLG described by Eq.(4.12) is shown in Fig. 4.5.

In our model, which is essentially non-interacting, the effects of screening can be included in a heuristic way by treating the potential strength in Eq.(4.9) as a function of carrier density parameterized by the chemical potential μ. We use a simple model which captures the overall behavior seen in the data

$$u \to u'(\mu) = \frac{u}{1 + (|\mu|/\mu_0)^\alpha} \tag{4.17}$$

where the parameter μ_0 depends on microscopic details. Comparing to the data indicates that a reasonably good fit can be achieved for $\alpha \approx 2$.

The results for MLG, of the form given in Eq. (4.10), are presented in Fig. 1c of the main text. The spatially resolved density of states is obtained for carrier densities $n = 0.05 \cdot 10^{11}{}_{\mathrm{cm}}{}^{-2}$ (red curve) and $n = 2.5 \cdot 10^{11}{}_{\mathrm{cm}}{}^{-2}$ (blue curve), where n accounts for the spin and valley degeneracy. Potential strength used is $\hbar u = -1.5\,\hbar v \approx 1$ eV·nm, the screening parameter value is $\mu_0 = 0.2\sqrt{\pi\hbar^2 v^2 n_0} \approx 7\,_{\mathrm{meV}}$, with $n_0 = 10^{11}{}_{\mathrm{cm}}{}^{-2}$ the corresponding carrier density.

A similar approach was used to model the density profile in BLG, with a pair of line delta functions mimicking the graphene edge potential. The resulting spatially resolved DOS in BLG, of the form given in Eq.(4.10) with $N_1(\varepsilon, x)$ defined in Eq.(4.13), is shown in Fig. 4b of the main text. The delta-function potential strength was parameterized in the same way as for MLG. The curves in Fig. 4b were obtained using the best-fit value $\hbar u = 0.7$ eV·nm and assuming no screening.

Microscopic derivation

To obtain Eq. (4.12) and Eq. (4.13) we consider long-wavelength modes for a line potential positioned at $x = 0$. This problem is described by the Hamiltonian $H = H_0 + V(x)$ with $V(x) = \hbar u \delta(x)$. Here we construct the Greens function which takes the full account of scattering by the potential $V(x)$. The discrete spectrum of the system, arising due to guided modes, can be conveniently expressed through the poles of the electron Greens function. The Greens function, in this case, can be evaluated using Dysons's equation and the T-matrix representation:

$$G = G_0 + G_0 V G_0 + G_0 V G_0 V G_0 + \cdots = G_0 + G_0 T G_0 \tag{4.18}$$

where $G_0 = (i\varepsilon - H_0)^{-1}$.

Naively, Dyson's equation for the T-matrix can be solved in an explicit way as

$$T(\varepsilon, p_y) = \hbar u \Big(1 - \hbar u \int \frac{dp_x}{2\pi\hbar} G_0(\varepsilon, \mathbf{p})\Big)^{-1} \tag{4.19}$$

In our problem, however, such a solution potentially misses the effects of the electron wavefunction phase variation in space near the delta-function potential. Indeed, the result in Eq.(4.19) can be seen to rely on the assumption of the wavefunction continuity in the vicinity of the delta-function. However, the property of wavefunction continuity holds for BLG but does not hold for MLG where the wavefunction phase experiences a jump across the delta-function (see discussion in the main text). The correct expression for the T-matrix for the MLG case, which is more complicated than that in Eq.(4.19), can be constructed by performing a suitable gauge transformation (to be discussed elsewhere). This analysis also indicates that despite the discontinuity pitfalls Eq.(4.19) provides a reasonable approx-

imation at not too large coupling strength values u. We will therefore use Eq.(4.19) on the merit of its simplicity to evaluate DOS at the weak-to-moderate coupling strengths. For that Eq.(4.19) has to be combined with the general expression for spatially resolved DOS

$$N(\varepsilon, \mathbf{r}) = -\frac{1}{\pi}\mathrm{Im}\,\mathrm{Tr}\,G(\varepsilon, \mathbf{r}, \mathbf{r}')_{\mathbf{r}=\mathbf{r}'}, \tag{4.20}$$

where the energy variable is analytically continued from positive imaginary values to real values via $i\varepsilon \to \varepsilon + i0$ with the trace taken over pseudospin variables. The results of this calculation for the MLG and BLG systems are presented below.

Microscopic derivation: MLG case

Evaluating the integral in Eq.(4.19) gives

$$T(\varepsilon, p_y) = \hbar u\Big(1 + \frac{u}{2v}\left(i\tilde{\varepsilon} + \sigma_1\tilde{p}\right)\Big)^{-1} \tag{4.21}$$

where we defined

$$\tilde{\varepsilon} = \frac{\varepsilon}{\sqrt{\varepsilon^2 + v^2p_y^2}} \qquad \tilde{p} = \frac{vp_y}{\sqrt{\varepsilon^2 + v^2p_y^2}} \tag{4.22}$$

Here ε is the Euclidean (Matsubara) frequency. Performing the analytic continuation $i\varepsilon \to \varepsilon + i0$ we find the T-matrix poles

$$\varepsilon = \pm\tilde{v}|p_y|, \quad \tilde{v} = v\frac{4v^2 - u^2}{4v^2 + u^2} \tag{4.23}$$

where the sign is given by $\pm = \mathrm{sign}\,u$. Eq.(4.23) describes the guided mode dispersion. Since $|\tilde{v}| < v$, the energies $\varepsilon = \pm\tilde{v}|p_y|$ are positioned, for each p_y value, outside the Dirac continuum of the bulk states. This expression behaves in a qualitatively similar way to the

exact dispersion derived in the main text, Eq. (1) (see Fig.4.1a of the main text). The guided modes described by Eq.(4.23) are quasi-1D states that propagate as plane waves in the y direction along the $x = 0$ line and decay exponentially as evanescent waves in the transverse direction.

To proceed with our calculation of spatially resolved DOS, we need Greens function evaluated in a mixed position-momentum representation

$$G_0(\varepsilon, p_y, x) = \int \frac{dp_x}{2\pi\hbar} e^{ip_x x} G_0(\varepsilon, \mathbf{p}) = \frac{-i\tilde{\varepsilon} - \sigma_2\tilde{p} - i\sigma_1 \mathrm{sign}(x)}{2\hbar v} \exp\bigl(-\kappa(i\varepsilon)|x|/\hbar\bigr) \tag{4.24}$$

where $\kappa(i\varepsilon) = \sqrt{(\varepsilon/v)^2 + p_y^2}$.

The trace of an equal-point Greens function in Eq.(4.20) then could be evaluated from Eq.(4.18) with the help of Eq.(4.21):

$$\mathrm{Tr}\, G(\varepsilon, x' = x) = \sum_{p_y} \left(\frac{\tilde{\varepsilon}}{i\hbar v} + \frac{4u\tilde{p}^2 e^{-2\kappa|x|/\hbar}}{\hbar\left[(2v + iu\tilde{\varepsilon})^2 - u^2\tilde{p}^2\right]} \right) \tag{4.25}$$

where the two terms represent contributions of G_0 and $G_0 T G_0$, respectively.

We start with considering the first term of (4.25). Introducing a UV cutoff $p_0 = \varepsilon_0/v$ we evaluate the sum over p_y as

$$\int_{-p_0}^{p_0} \frac{dp_y}{2\pi\hbar} \frac{\varepsilon}{\sqrt{\varepsilon^2 + v^2 p_y^2}} = \frac{\varepsilon}{\pi\hbar v} \ln \frac{\varepsilon_0}{\varepsilon}. \tag{4.26}$$

Performing analytic continuation $i\varepsilon \to \delta - i\varepsilon$, we arrive at

$$N_0(\varepsilon) = -\frac{\varepsilon}{\pi^2\hbar^2 v^2} \mathrm{Im}\, \ln \frac{\varepsilon_0}{\delta - i\varepsilon} \tag{4.27}$$

where $\delta = +0$. Taking the imaginary part, we obtain the expression in Eq.(4.11).

Next, we evaluate the second term in Eq.(4.25). Performing the same analytic continuation, we arrive at the result in Eq.(4.12). The expression in Eq.(4.12) can be conveniently analyzed by dividing the integral into two parts, taken over the domains $|p_y| > |\varepsilon|/\hbar v$ and $|p_y| < |\varepsilon|/\hbar v$, respectively. The latter contribution is particularly simple because it is governed by the pole (4.23) and can be easily evaluated as an integral of a delta function, giving

$$N_{\text{g.w.}}(\varepsilon, x) = \frac{2u|\varepsilon|}{\hbar^2 \tilde{v}(4v^2 - u^2)} e^{-2\sqrt{(v/\tilde{v})^2 - 1}|x||\varepsilon|/\hbar v} \tag{4.28}$$

This contribution is solely due to the guided mode. As illustrated in the Fig 4.5, this term dominates the peak structure in DOS for guided waves. The contribution of the region $|p_y| > |\varepsilon|/\hbar v$ describes the enhancement of DOS dues to the states in the continuum being pulled on the delta-function potential. This contribution is evaluated numerically.

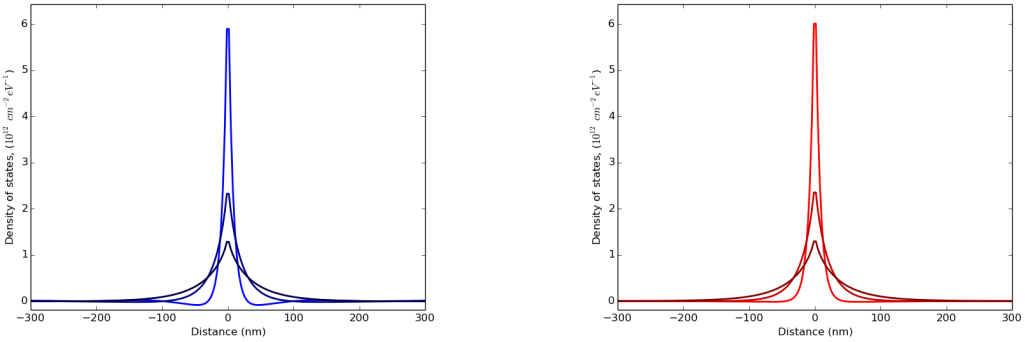

Figure 4.5: Plotted is the excess contribution to the spatially-resolved DOS, $\Delta N(\varepsilon, x) = N(\varepsilon, x) - N_0(\varepsilon)$ vs. distance from the delta function, where we subtracted the bulk contribution $N_0(\varepsilon)$ given in Eq. (4.11). The left panel shows the full excess contribution obtained from Eq. (4.12), the right panel shows the contribution solely due to the guided modes, Eq. (4.28). The two contributions are nearly identical, confirming that the peak in DOS can serve as a signature of the guided modes. Parameter values used: $\hbar u = -1.5\hbar v$, energies $\varepsilon = \varepsilon_0, 0.5\varepsilon_0, 0.1\varepsilon_0$, where $\varepsilon_0 = \pi\hbar\sqrt{\pi n_0}$, $n_0 = 10^{11}\,\text{cm}^{-2}$ (higher peaks correspond to higher energy values ε).

We used the full expression in Eq.(4.12) to produce the spatially resolved DOS curves shown in Fig.4.1c of the main text. In that, we accounted for screening, as described

in Eq.(4.17). Because of screening, the peak structure is more prominent at low chemical potential, and is suppressed relatively to the bulk DOS at high chemical potential values.

Microscopic derivation: BLG case

Following the same procedure as above, we derive the free electron Greens function for BLG in a mixed position-momentum representation:

$$G_0(\varepsilon, p_y, x) = \int \frac{dp_x}{2\pi\hbar} e^{ip_x x} G_0(\varepsilon, \mathbf{p}) = -\frac{1}{\hbar u}\Big(F_0(x) + \sigma_1 F_1(x) + i\sigma_2 F_2(x)\mathrm{sign}(x)\Big) \quad (4.29)$$

where we used the quantities defined in Eqs. (4.14)-(4.16). The dispersion relation can then be obtained from the T-matrix:

$$T(\varepsilon, p_y) = \hbar u\Big(1 - \hbar u G_0(\varepsilon, p_y, x)\big|_{x=0}\Big)^{-1} \quad (4.30)$$

Solving for the poles of this 2×2 T-matrix, we obtain two independent equations describing mode dispersion

$$\varepsilon(p) = \frac{u}{2}\left(\kappa^{+}_{\varepsilon,p} - \frac{p^2}{\kappa^{-}_{\varepsilon,p}}\right), \qquad \varepsilon(p) = \frac{u}{2}\left(\kappa^{-}_{\varepsilon,p} - \frac{p^2}{\kappa^{+}_{\varepsilon,p}}\right) \quad (4.31)$$

where $\kappa^{\pm}_{\varepsilon,p} = \sqrt{p^2 \pm 2m^*\varepsilon(p)}$. These equations have be easily solved numerically, giving two independent guided modes.

The resulting mode spectrum is more complicated than in the MLG case, Eq.(4.23). For energies $\varepsilon \leq \varepsilon' = m^*u^2/4$ two modes exist, whereas for higher energies only one mode exists. The latter features dispersion with the large-p_y asymptotic of the form

$$\varepsilon(p_y) \approx -\mathrm{sign}\, u\left(\frac{p_y^2}{2m^*} - \frac{m^*u^2}{4}\right) \qquad |p_y| \gg m^*|u| \quad (4.32)$$

For both modes the dispersion relation is such that the mode frequencies lie outside the continuum spectrum of BLG bulk (see Fig.4.1b of the main text). This property ensures 1D confinement.

The effect of disorder

In the presence of disorder scattering, guided modes acquire a finite lifetime. This is described by a complex dispersion frequency

$$\varepsilon = \tilde{v}|p_y| - i\gamma/2 \tag{4.33}$$

where the imaginary part can be expressed through the inverse lifetime, $\gamma = 1/\tau$.

Here we estimate the effect of disorder scattering assuming that it occurs predominantly at the graphene edge. We model the effect of edge roughness by a fluctuating confining potential strength, for simplicity treating the fluctuations as a gaussian white noise:

$$V(x,y) = \hbar\Big(u + \delta u(y)\Big)\,\delta(x), \quad \Big\langle \delta u(y)\delta u(y')\Big\rangle = \frac{\alpha}{\hbar^2}\delta(y-y'). \tag{4.34}$$

Writing the Greens function as a series expansion in the potential $V + \delta V$, Eq.(4.34), we have

$$G = G_0 + G_0(V+\delta V)G_0 + G_0(V+\delta V)G_0(V+\delta V)G_0 + ... \tag{4.35}$$

In averaging the Greens function over disorder, we employ the gaussian noise model in which we only need to account for the pair correlators $\langle \delta u(y)\delta u(y')\rangle$. In a non-crossing approximation, we express the disorder-averaged Greens function through a suitable self-energy

$$\langle G\rangle = G_0 + G_0(V+\Sigma)G_0 + G_0(V+\Sigma)G_0(V+\Sigma)G_0 + ... \tag{4.36}$$

where

$$\Sigma(\varepsilon) = \alpha \int \frac{dp_x}{2\pi\hbar} G(\varepsilon, p_y, x, x')_{x=x'=0} \tag{4.37}$$

The quantity (4.37) is complex-valued, with the imaginary part expressed through the density of states $N(\varepsilon)$ at $x = 0$ as

$$\mathrm{Im}\mathrm{Tr}\,\Sigma(\varepsilon) = -\pi\alpha N(\varepsilon)_{x=0}. \tag{4.38}$$

The disorder scattering rate for the guided waves in MLG can now be found from the dispersion relation obtained from the T-matrix pole, Eg(4.19), which is corrected by the presence of Σ as follows

$$1 + (\hbar u + \Sigma(i\varepsilon))\frac{i\tilde{\varepsilon} + \sigma_1\tilde{p}}{2\hbar v} = 0. \tag{4.39}$$

Here we continue to use the Euclidean (Matsubara) frequency notation, as in Eqs.(4.19), (4.21).

Since the density of states scales linearly with energy, $N(\varepsilon) \sim |\varepsilon|$ (see Eqs.(4.28),(4.11)), we can solve Eq.(4.39) in the long-wavelength limit treating $\Sigma(i\varepsilon)$ as a perturbation. Writing $\varepsilon = \varepsilon_0(p_y) + \delta\varepsilon$, where $\varepsilon_0 = \tilde{v}|p_y|$ is a solution for $\Sigma = 0$, we linearize in $\delta\varepsilon$ to obtain

$$\delta\varepsilon = -\frac{1}{\hbar u}\Big(1 - \frac{\tilde{v}^2}{v^2}\Big)\Sigma(i\varepsilon_0)|p_y|v \tag{4.40}$$

where $\tilde{v}$ is given by Eq.(4.23). After analytic continuation, we obtain dispersion relation in the form (4.33) with

$$\gamma(p_y) = \frac{\pi\alpha}{\hbar|u|}\Big(1 - \frac{\tilde{v}^2}{v^2}\Big)|p_y|vN\big(\tilde{v}|p_y|\big)_{x=0} \tag{4.41}$$

Accounting for the linear scaling $N(\varepsilon) \sim |\varepsilon|$, we find that the damping rate scales as p_y^2,

$$\gamma(p_y) = \frac{2\pi\alpha p_y^2}{\hbar^3(4v^2 - u^2)}\Big(1 - \frac{\tilde{v}^2}{v^2}\Big) \tag{4.42}$$

(we approximated the density of states by the expression in Eq.(4.28) which dominates near the line potential). The mean free path, defined by $l = \tilde{v}\tau$ with $\tau = \hbar/\gamma$, can now be related to the guided mode wavelength λ as

$$l = \frac{\lambda^2}{\xi}, \quad \xi = \frac{8\pi^3\alpha}{\hbar^2 v^2}\frac{1 - \tilde{v}^2/v^2}{4 - u^2/v^2}. \tag{4.43}$$

For an edge which is rough on the atomic scale we expect the values ξ on the order of lattice constant. The mean free path given by Eq.(4.43) grows rapidly with wavelength. Physically, the quadratic scaling $l \sim \lambda^2$ in Eq.(4.43) originates from the confinement becoming weaker at small ε, which allows the mode to diffract around disorder. This is in a direct analogy with the weakly guiding fiber designs for optical waves, where weak confinement is employed to achieve exceptionally long mean free paths.

Similar estimates hold for the BLG case. Indeed, the property of waves to diffract around disorder of the characteristic scale smaller than the wavelength is completely general, being valid for waves of any nature, electronic or else. Since the relation between carrier density and wavelength is the same for MLG and BLG, experimental densities translate to the wavelength values similar to those used above, $\lambda \sim 50$ nm. As in the MLG case, scattering by a short-range scatterers localized at the edge becomes inefficient at small ε, leading to large mean free path values.

4.4.2 Josephson junctions: Device overview

We analyze five graphene Josephson junctions on hBN with widths ranging from $W = 800 - 1200$ nm and lengths ranging from $L = 250 - 350$ nm (see Fig. 4.1d of the main text for a labeled device schematic). Listed in Table 4.1 are details on individual sample geometries. The small L/W aspect ratios place these devices are in the narrow junction limit, where the the critical current I_c can be approximated as a phase dependent summation over many parallel 1D current channels. Electrical measurements are conducted using standard Lockin techniques in a Leiden Cryogenics Model Minikelvin 126-TOF dilution refrigerator with a base temperature of 10 mK, well below the critical temperature of Al.

Using a dry transfer method, graphene/hBN stacks are sequentially deposited on a 300 nm thermally grown SiO_2 layer, which covers a doped silicon substrate functioning as a global back gate. Graphene flakes are etched to the desired geometry using a 950 PMMA A4 polymer mask ($\sim$ 200 nm thick; spun at 4000 rpm) followed by an RIE O2 plasma etch. Titanium/aluminum (Ti/Al) superconducting electrodes are defined on selected flakes using electron beam (ebeam) lithography on a 950 PMMA A4 resist mask, followed by thermal evaporation and liftoff in acetone. For the titanium adhesion layer, we evaporate 10 nm at a rate of 0.3 Angstrom/s. This is followed by an evaporation of a 70 nm aluminum layer at a rate of 0.5 Angstrom/s at pressures in the low to mid 10^{-7} Torr range. For dual-gated bilayers, suspended top gates are fabricated using a standard PMMA/MMA/PMMA trilayer resist method which leaves a 200 nm air gap between the top gate and graphene. After using ebeam lithography to define the gates, which employs position-dependent dosage, Cr/Au (3/425 nm) gates are deposited using thermal evaporation and liftoff in acetone. To remove processing residues and enhance quality, devices were current annealed in vacuum at dilution refrigerator temperatures. We note that edge currents were detected both in current-annealed and intrinsically high quality non-annealed

devices; typically the appearance of edge currents coincided with the occurrence of Fabry-Perot interference in the ballistic transport regime. All five graphene Josephson junctions exhibit similar transport behavior. Additional data sets are provided in the Supplementary Figures.

4.4.3 Fourier method for extraction of supercurrent density distribution

In a magnetic field B, the critical current $I_c(B)$ through a Josephson junction equals the magnitude of the complex Fourier transform of the current density distribution $J(x)$:

$$I_c(B) = |\mathcal{I}_c(B)| = \left| \int_{-\infty}^{\infty} J(x) \exp(2\pi i (L + l_{Al}) Bx/\Phi_0) dx \right| \tag{4.44}$$

where x is the dimension along the width of the superconducting contacts (labeled in Fig. 4.1d), L is the distance between contacts, l_{Al} is the magnetic penetration length (due to a finite London penetration depth in the superconductor and flux focusing), and $\Phi_0 = h/2e$ is the flux quantum. Relevant in the narrow junction limit where current is only a function of one coordinate, Eq. (4.44) provides a simple and concise description of our system. We employ Fourier techniques introduced by Dynes and Fulton to extract the real space current density distribution from the magnetic interference pattern $I_c(B)$. By expressing the current density as $J(x) = J_s(x) + J_a(x)$, where $J_s(x)$ and $J_a(x)$ are the symmetric and antisymmetric components, the complex critical current can be rewritten as:

$$\mathcal{I}_c(B) = \int_{-\infty}^{\infty} J_s(x) \cos(2\pi (L+l_{Al}) Bx/\Phi_0) dx + i \int_{-\infty}^{\infty} J_a(x) \sin(2\pi (L+l_{Al}) Bx/\Phi_0) dx \tag{4.45}$$

We calculate symmetric component of distribution, the relevant quantity for analyzing edge versus bulk behavior, as the antisymmetric component goes to zero in the middle of the sample. For symmetric solutions, $\mathcal{I}_c(B)$ is purely real. To reconstruct $\mathcal{I}_c(B)$ from the

measured critical current, the sign of $I_c(B)$ is reversed for alternating lobes of the Fraunhofer interference patterns. The extracted supercurrent distribution is expressed as an inverse Fourier transform:

$$J_s(x) \approx \int_{-\infty}^{\infty} \mathcal{I}_c(B) \exp(2\pi i(L + l_{Al})Bx/\Phi_0)dB \tag{4.46}$$

Because $I_c(B)$ is only nonzero over a rectangular window dictated by the finite scan range $B_{\min} < B < B_{\max}$, distribution extracted numerically is given by the convolution of $J(x)$ with the sinc function. To reduce artifacts due the convolution, we employ a raised cosine filter to taper the window at the endpoints of the scan. Explicitly,

$$J_s(x) \approx \int_{B_{\min}}^{B_{\max}} \mathcal{I}_c(B) \cos^n(\pi B/2L_B) \exp(2\pi i(L + l_{Al})Bx/\Phi_0)dB \tag{4.47}$$

where $n = 0.5 - 1$ and $L_B = (B_{\max} - B_{\min})/2$ is the magnetic field range of the scan.

While the presence of magnetic vortices can provide a different origin for anomalous Fraunhofer patterns, this physics does not apply to our experiment because the width of our devices is small compared to length scales relevant for that phenomenon. Furthermore, if magnetic vortices were the origin of the anomalous Fraunhofer patterns, they should equally affect response at all carrier densities for the same range of flux. The fact that anomalous patterns only arise at densities near charge neutrality further rules out magnetic vortices as a possible origin.

4.4.4 Gaussian fits to extract edge state widths

To extract a length scale for the width of the edge currents near the Dirac point, we fit the experimental supercurrent density distribution $J_c(x)$ to the Gaussian function

$$J_c^G(x) = b\left(\exp\left(\frac{-(x-a)^2}{c}\right) + \exp\left(\frac{-(x+a)^2}{c}\right)\right) \tag{4.48}$$

where a determines the spatial peak offset, b determines peak height, and c determines peak width. For the data in Fig. 4.1h, the fit parameters are $a = 0.515$, $b = 8.8$, and $c = 0.017$. The effective edge current width, given by the Gaussian full width at half maximum $x_{FWHM} = 2\sqrt{c \cdot \ln 2}$, is 220 nm.

4.4.5 Edge versus bulk amplitudes

To more quantitatively assess the evolution of edge and bulk currents with electronic carrier density n, we plot line cuts of the individual contributions (see Fig. 4.2f and 4.3b). These are given by:

$$J_c^{edge}(n) = \sum_{x_i=-x_W}^{-x_W+\varepsilon_1} \frac{J_c(x_i,n)}{N_1} \quad \text{and} \quad J_c^{bulk}(n) = \sum_{x_i=-\varepsilon_2}^{\varepsilon_2} \frac{J_c(x_i,n)}{N_2} \tag{4.49}$$

for a graphene flake whose full width spans from $-x_W$ to x_W. $J_c^{edge}(n)$ is the spatially averaged current amplitude over a small window of width ε_1 from the edge of the flake. Similarly, $J_c^{bulk}(n)$ is the spatially averaged current amplitude over a strip of width $2\varepsilon_2$ around the center of the flake. $N_1 = \varepsilon_1/x_{step}$ and $N_2 = \varepsilon_2/x_{step}$, where x_{step} is the distance between data points (determined by the magnetic field range of the scan). For example, for the plots in Fig. 4.2f, $x_W = 405$ nm, $\varepsilon_1 = 29$ nm, and $\varepsilon_2 = 87$ nm.

Based on the edge versus bulk current profiles, one may infer whether edge doping

is the dominant cause of edge currents in our devices. In the presence of edge doping, the edge versus bulk contributions should be reversed for opposite polarities of bulk carriers (for example, edge dominated behavior at high densities on the electron side and bulk dominated behavior at high densities on the hole side), which is not consistent with the data. Bulk-dominated or flat distributions appear at both high electron and hole doping fairly consistently. As a second test, one can track the edge versus bulk contributions through the Dirac point to detect an offset in gate voltage between the charge neutrality point at the edge versus in the bulk. We did not detect positional density offset substantial enough to account for the large edge currents in these devices (Fig. 4.2f).

4.4.6 Bayesian method for extraction of supercurrent density distribution

The critical current as a function of the magnetic field, $I_c(B)$, is related to the current density through the junction, $J_c(x)$, as

$$I_c(B) = \int_{-\frac{W}{2}}^{\frac{W}{2}} dx\, J_c(x) \exp\left(2\pi i x L B/\Phi_0\right), \tag{4.50}$$

with L and W the length and width of the junction, and $\Phi_0 = h/2e$ the superconducting flux quantum.

In the measured $|I_c(B)|$ all information about its complex phase is lost, making the problem of determining the current density not have a unique solution. Using the method of Dynes and Fulton (DF), a unique solution can be found under the assumption of a symmetric current distribution, $J_c(x) = J_c(-x)$. In practice however, disorder and inhomogeneities in the junction will lead to asymmetric current densities. Additionally, since experiments are performed over a finite range of magnetic fields, there is a cutoff in the current density resolution. Neither this finite resolution, nor experimental uncertainties

are taken into account in the DF method, meaning it can only provide a qualitative estimate of $J_c(x)$.

To gain a more quantitative understanding, we instead ask what is the distribution of $J_c(x)$ which produces the same critical current $I_c(B)$. We answer this question by performing Bayesian inference to obtain the posterior distribution of the current density, given the measured critical current. In our case, Bayes' rule reads:

$$\mathcal{P}\big(J_c;|I_c|\big) = \frac{\mathcal{P}\big(|I_c|;J_c\big)\,\mathcal{P}\big(J_c\big)}{\mathcal{P}\big(|I_c|\big)}. \tag{4.51}$$

Here, $\mathcal{P}\big(J_c;|I_c|\big)$ is the posterior distribution of the current density, the quantity we want to calculate, while $\mathcal{P}\big(J_c\big)$ is its prior distribution. The likelihood function $\mathcal{P}\big(|I_c|;J_c\big)$ indicates the compatibility of the measured critical current with a given current density:

$$\mathcal{P}\big(|I_c|;J_c\big) = \exp\left[-\frac{(|I_c|-|I_c^f|)^2}{2\varepsilon^2}\right], \tag{4.52}$$

where I_c^f is the current obtained from J_c by using Eq. (4.50), I_c is the measured current, and ε is the measurement error. The factor $\mathcal{P}\big(|I_c|\big)$ is the same for all current densities, meaning it does not enter into determining their relative probabilities.

The experimental current profiles are extracted from scans of the differential resistance as a function of DC current bias and magnetic field, $dV/dI(I_{\mathrm{DC}},B)$. Within the same scan, for some field values dV/dI has a clear maximum, while for others it monotonically increases towards its normal state value. We extract the critical current as the value I_{DC} at which the differential resistance is $x \times \max dV/dI$, choosing a value of $x \lesssim 1$. This selects points close to the maxima at field values where they are well defined, and points close to where the differential resistance reaches its normal state value otherwise. The uncertainty is obtained in the same fashion, by choosing a slightly smaller cutoff.

We maximize the likelihood function using a Monte Carlo sampling algorithm. [101] To get a large resolution of the current density without a significant increase in the dimensionality of the sampling space, we expand $J_c(x)$ as

$$J_c(x) = \sum_{n=0}^{N} A_n \cos(2\pi n x/L) \tag{4.53}$$

and enforce $J_c(x) > 0$ for all x. The A_n coefficients determine the shape of the distribution, which in Eq. (4.53) is assumed to be symmetric, $J_c(x) = J_c(-x)$. Using an asymmetric form would typically lead to a critical current which shows node lifting – the minima of $I_c(B)$ have nonzero values. While this feature is present in the measured critical current, it can be accounted for by factors other than an asymmetric current distribution, such as relatively small aspect ratios ($\sim$5), and a non-sinusoidal current-phase relationship arising from a large junction transparency. Using a symmetric J_c avoids this ambiguity, and has the additional advantage of providing a more direct comparison between our method and that of Dynes and Fulton.

The likelihood function is maximized by allowing the A_n coefficients to vary at each Monte Carlo step. As N is increased the posterior distribution of the current density widens, an indication of over-fitting. This increase in uncertainty serves as a criterion for choosing N, which for the typical dataset is between 4 and 8. The priors of A_n are set to the uniform distribution $[-\max(I_c), \max(I_c)]$.

An example of our method is shown in Fig. 4.6, using $N = 5$. The current density is peaked at the edges of the sample, a feature also recovered in the DF approach. The corresponding critical current is in good agreement with the measured one, with the exception of the regions close to the nodes. Fig. 4.6 indicates that the supercurrent through the junction flows mainly along its edges. As a further test of the edge state contribution,

we modify the functional form of the current density in Eq. (4.53), to explicitly allow for edge states. We add delta functions to the current density at the edges of the sample, $J_c(x) \rightarrow J_c(x) + d_L\delta(x + W/2) + d_R\delta(x - W/2)$, and estimate the contribution of edge states as the ratio of $d_L + d_R$ to the total current density J_c^{tot}. As the carrier density approaches zero a significant fraction of the supercurrent is carried by the edge states, with $(d_L + d_R)/J_c^{\text{tot}} \simeq 0.45$ (see Fig. 4.7).

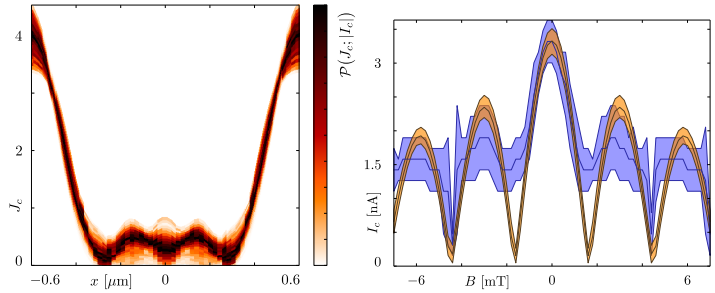

Figure 4.6: Posterior distribution of the current density (left panel), and corresponding critical current (right panel). The values of I_c obtained from the posterior distribution (orange) are in good agreement with the measured critical current (blue).

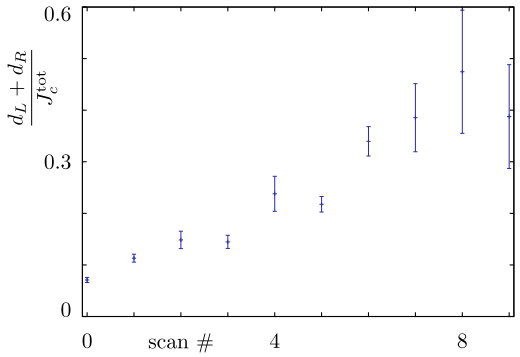

Figure 4.7: Each scan corresponds to a Fraunhofer pattern, with Fig. 4.6 showing the 8^{th} scan. (Increasing scan number corresponds to decreasing carrier density.)

The amount of disorder leading to the appearance of guided edge modes in our

samples can indeed be expected to be different at the two edges. However, as shown earlier in the Extended Discussion, the mean free path of the guided edge modes is estimated to be significantly larger than the junction length. This is a consequence of weak confinement at the edge, making the edge mode wavefunctions extend far from the edge and lie mostly outside of the confining potential. Such states can diffract around disorder at the edge gaining large mean free path. As a result, impurity scattering is ineffective, so we expect a similar amount of current flowing at the two edges, and use a theoretical model where symmetry is explicitly built in.

Current asymmetry generically leads to interference patterns which show node lifting, a phenomenon where the minima of the critical current $I_c(B)$ acquire non-zero values. Because minimal node lifting is observed experimentally, the distributions are qualitatively expected to be almost symmetric. This behavior provides indirect confirmation of the guided edge mode model, which allows for a large degree of symmetry even in the presence of disordered edges. While minor node lifting is present in the measured data, it can be ascribed to other factors than an asymmetric current distribution, such as a large aspect ratio, and non-sinusoidal current phase relations. The use of a symmetric current model avoids the ambiguity of which combinations of factors lead to node lifting.

To give bounds on asymmetry of edge currents, we include results on Bayesian analysis for non-symmetric distributions. The effect of an asymmetric current distribution can be quantified by adding $\sum_{i=1}^{N} B_n \sin(2\pi n x/L)$ to the current distribution $J_c(x)$, with N=5 as for the symmetric part. We have included a new figure (Fig. 4.8) showing the spatial distribution of current through the junction, which remains peaked at the edges but becomes slightly asymmetric as a consequence of node-lifting.

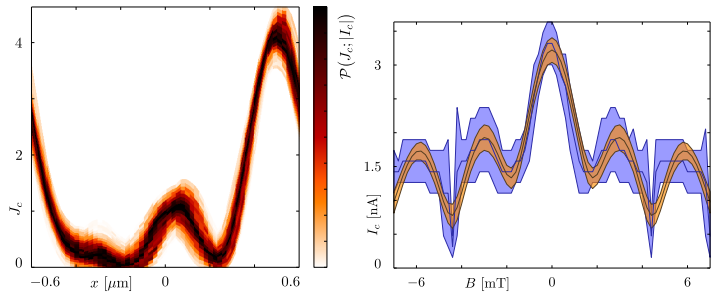

Figure 4.8: Same as Fig. 4.6, but including the effect of an asymmetric current distribution by adding $\sum_{i=1}^{N} B_n \sin(2\pi n x/L)$ to the current distribution $J_c(x)$, with $N = 5$ as for the symmetric part. The posterior current density distribution (left) remains peaked at the edges, but becomes asymmetric, as a consequence of node-lifting. The corresponding critical current is now in good agreement with the measured one also in the node regions (right).

4.4.7 Normal state device characterization

We have provided normal state characteristics of the graphene layer in Fig. 4.9 and used conventional wisdom to determine whether devices are clean, including Dirac point width and Fabry-Perot oscillations, both of which indicate high quality flakes. To assess the intrinsic graphene quality, we estimate the charge inhomogeneity to be in the low 10^{10} cm^{-2} range based on Dirac point width on the normal resistance curves. Note that this is a conservative upper bound that likely overestimates the amount of disorder because the presence of Fabry-Perot resonances on the hole side broadens the curve (Fig. 4.9). By comparison, the edge-dominated transport regime exists over a widow extending to densities $\sim 2-3\times10^{11}$ cm^{-2} (see Fig. 4.2d; also Figs. 4.3a, 4.4a of the main text) away from the charge neutrality point, exceeding the intrinsic charge inhomogeneity by roughly an order of magnitude. Furthermore, the window (in density) of edge-dominated transport consistently exceeds the charge inhomogeneity in multiple devices that exhibit edge currents (see caption of Fig. 4.9 for detailed parameters).

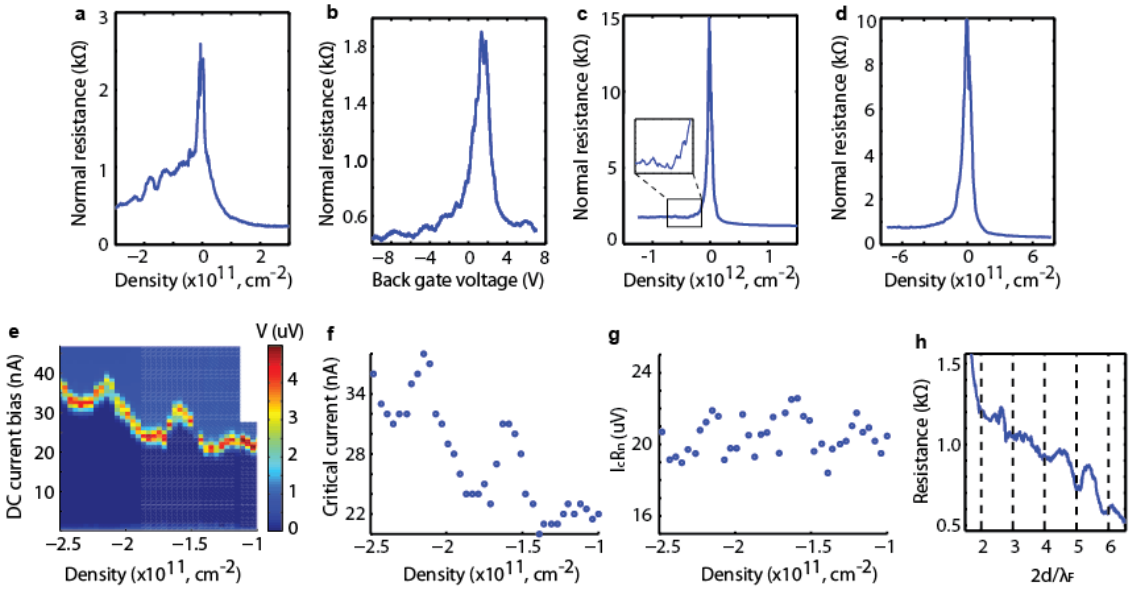

Figure 4.9: **(a)** Normal resistance of device ML1. At hole dopings, Fabry-Perot oscillations appear, a signature of ballistic transport. The Dirac point's full width at half maximum is about $3.4 \times 10^{10}\,\mathrm{cm}^{-2}$. The edge-to-bulk crossover density is roughly $3 \times 10^{11}\,\mathrm{cm}^{-2}$. **(b)** Normal resistance of device BL4. Ballistic Fabry-Perot oscillations also appear on the hole side. **(c)** Normal resistance of device BL2. Signatures of Fabry-Perot interference appear upon zooming into the hole side of the neutrality point (see inset). The Dirac point's full width at half maximum is about $6.9 \times 10^{10}\,\mathrm{cm}^{-2}$. The edge-to-bulk crossover density is roughly $-3 \times 10^{11}\,\mathrm{cm}^{-2}$. **(d)** Normal resistance of device BL3. The Dirac point's full width at half maximum is about $8 \times 10^{10}\,\mathrm{cm}^{-2}$. The edge-to-bulk crossover density is roughly $-2.5 \times 10^{11}\,\mathrm{cm}^{-2}$. **(e)** Ballistic supercurrent oscillations in the Fabry-Perot regime, shown in a plot of applied DC current bias vs density at zero magnetic field. The critical current I_c marks the transition between dissipationless and resistive states. Data taken from device ML1. **(f)** Plot of critical current I_c oscillations from the data in panel (e). **(g)** Plot of the I_cR_n product from the data in panel (e). **(h)** Oscillations in panel (a) plotted versus $2d/\lambda_F$, where λ_F is the Fermi wavelength and $d = 225$ nm is the effective cavity length. Resonances appear when the constructive interference conditions are satisfied for electron waves in a resonator, $2d = N\lambda_F$ for integer N, verifying that the oscillations are indeed associated with Fabry-Perot interference.

As a second indicator of quality, the existence of Fabry-Perot interferences on the hole side of normal state resistance curves show that the samples are in the ballistic limit (see Fig. 4.9). Large spatial density fluctuations would prevent such resonances from being resolved in transport. Edge currents only appear in the cleanest devices and tend to emerge

in ballistic samples that exhibit Fabry-Perot interference, which suggests that the observed edge states are indeed correlated with higher sample quality. The reproducibility of the width of the edge currents over many independent samples also rules out random disorder effects, which would yield a wide range of edge peak shapes and widths. While current annealing has been noted to enhance quality, it is not strictly necessary for observation of edge modes, which have been observed in both annealed and non-annealed devices.

We estimate the contact quality as follows: at carrier density $n = 10^{11}\ cm^{-2}$, the normal state resistance of device ML1 is 350 Ohms (Fig. 4.9a). At this density, the Fermi wavelength is $\lambda = 112$ nm. Given that the width of the device is W=1200 nm, the number of conducting channels (N) can be estimated from the sample geometry using the relation $N = aW/(\lambda/2) = 84$ modes, where $a = 4$ accounts for the spin and sublattice degeneracies in graphene. The ideal conductance is therefore $84e^2/h = 307$ Ohms. By comparing this value to the measured resistance, this yields a total estimated contact resistance of 43 Ohms, or transmission coefficient of $\sim 90\%$.

Chapter 5

Visualization of phase-coherent electron interference in a ballistic graphene Josephson junction

5.1 Overview

Interference of standing waves in electromagnetic resonators forms the basis of many technologies, from telecommunications [102] and spectroscopy [103] to detection of gravitational waves [104]. However, unlike the confinement of light waves in vacuum, the interference of electronic waves in solids is complicated by boundary properties of the crystal, notably leading to electron guiding by atomic-scale potentials at the edges [77–80]. The microscopic role of boundaries on wave interference is an unresolved question due to the challenge of detecting charge flow with submicron resolution. Here we employ Fraunhofer interferometry to achieve spatial imaging of cavity modes in a graphene Fabry-Pérot (FP) resonator, embedded between two superconductors to form a Josephson junction [21, 22].

By directly visualizing current flow using Fourier methods [24], our measurements reveal surprising spatial redistribution of current on and off resonance. These findings provide evidence of separate interference conditions for edge and bulk states and elucidate the microscopic nature of interference at the crystal boundaries. We also observe modulation of the multiple Andreev reflection amplitude on and off resonance, a direct measure of cavity transparency. These results represent a new regime of Josephson behavior at the intersection of superconductivity and electron-optics.

5.2 Electron optics in ballistic graphene

Graphene provides an appealing platform to explore "electron-optics" due to the ballistic nature of wavelike carriers and ability to engineer transmission of electronic waves in real space using electrostatic potentials [69–76]. In particular, the electronic analog to refractive index is the Fermi energy, which is tunable via electrostatic gating [70, 105]. Because the gapless spectrum of Dirac materials enables continuous tunability of carrier polarity, positive and negative index of refraction regions can be combined in bipolar structures that form the building blocks of Veselago "electronic lenses" [74], Fabry-Pérot (FP) interferometers [70–74, 76], and whispering gallery mode cavities [106]. Electronic analogs to optical interferometers attract attention because relativistic effects such as hyperlensing and phase-coherent Klein transmission provide capabilities beyond conventional optics [69–76, 107]. Here we investigate the simplest analog to an optical interferometer, the electron FP resonator, which consists of standing electron waves confined between two reflective interfaces [48, 108]. Despite extensive exploration in the momentum domain, in which Fermi momentum is simply tuned with a gate, little information is available about the real-space distribution of current flow due to the challenge of imaging current paths

with submicron resolution. Furthermore, in real devices, atomically sharp potentials at the edges of graphene can confine electron waves into guided edge modes, in analogy to the guiding of light in optical fibers [77–80], as we have demonstrated experimentally in prior work [109]. To investigate the nature of these boundary currents, we measure the interference of standing waves in a graphene Josephson junction and image the real space distribution of supercurrent flow using Fraunhofer interferometry [24]. By visualizing the spatial structure of current-carrying states in the cavity using Fourier methods, our measurements disentangle edge from bulk current flow and highlight the surprising role of the crystal boundaries.

In a coherent electron cavity, quantum interference of electron waves replaces classical diffusion as a key feature of electronic transport [48, 108]. In our system, a pair of superconducting electrodes is coupled to a graphene membrane, defining a ballistic cavity between the two graphene-electrode interfaces. As the Fermi wavelength in the cavity is tuned with a gate, the quantized energy levels of the cavity are moved on and off resonance with the Fermi energy of the superconducting leads, thus inducing an oscillatory critical current whose period satisfies the FP interference conditions. Due to the chiral nature of fermions in monolayer and bilayer graphene, at zero magnetic field carrier trajectories with an incidence angle θ and refraction angle angle θ' produce a contribution to FP fringes in the single-particle transmission probability of the form

$$T(\theta) \sim \frac{|t_1(\theta)|^2 |t_2(\theta)|^2}{|1 - r_1(\theta) r_2(\theta) e^{2ik_\parallel L}|^2}, \quad k_\parallel = k \cos\theta' \tag{5.1}$$

where $t_{1,2}$ and $r_{1,2}$ are the angle-dependent transmission and reflection amplitudes for the two p-n junctions. The resulting fringes are dominated by the angles for which both the transmission and reflection are reasonably high (the first harmonic of FP fringes is at its

brightest when the product of transmission and reflection coefficients $|t(\theta)|^2|r(\theta)|^2$ takes a maximum value). In general, a spread of angles for different trajectories in the bulk gives rise to a spread of the FP oscillation periods, somewhat reducing the fringe visibility in the net current. In contrast, no suppression is expected for interference fringes due to edge modes, as discussed in detail later.

5.3 Superconducting transport in a ballistic graphene Josephson junction

We employ proximity induced superconductivity to shed light on the microscopic nature of electron interference in a graphene Josephson resonator [110–113]. On a practical level, graphene provides an accessible interface for superconducting electrodes because it is purely a surface material, unlike 2D electron gases embedded in semiconductor heterostructures. Although graphene is not intrinsically superconducting, proximity-induced superconductivity can be mediated by phase coherent Andreev reflection at the graphene/superconductor interface [21, 22]. This process features an electron-hole conversion by the superconducting pair potential that switches both spin and valley to preserve singlet pairing and zero total momentum of the Cooper pair [20]. In this study, we employ gated mesoscopic Josephson junctions consisting of bilayer graphene suspended between two superconducting Ti/Al electrodes, as well as a graphene device on hBN. The superconductors serve three roles: (1) they create electrostatic potentials that confine electron waves, serving as electronic analogs to mirrors (2) superconducting interferometry can extract spatial information on how current flows through the system, and (3) beyond equilibrium, scattering events between the superconductors and graphene (multiple Andreev reflections) depend critically on resonance conditions and reveal how the resonator couples to the out-

side world.

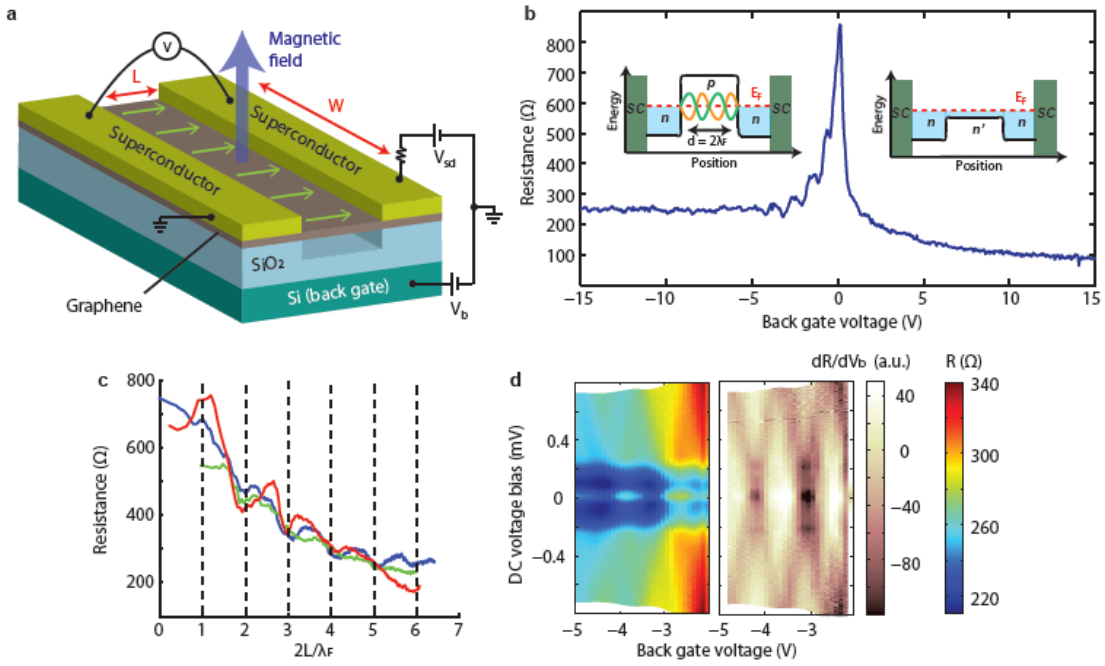

Figure 5.1: **(a)** Gated mesoscopic Josephson junction consisting of bilayer graphene suspended between two superconducting Ti/Al electrodes. L is the lithographic distance between contacts and W is the junction width. In the presence of magnetic field, a flux threads the junction area. A current bias is applied between the electrodes and the voltage drop across the device is recorded. A voltage applied to the back gate electrode V_b tunes the Fermi wavelength λ_F in the cavity. **(b)** Plot of the normal resistance R_n, obtained by sweeping the gate voltage V_b at a fixed bias exceeding I_c. Data sets in panels (b-d) are from device *B1*. *Left inset:* Charge transfer at the boundaries of the superconducting electrodes leads to intrinsic n-doped regions near the contacts, forming an electronic resonator when the bulk is tuned to hole doping. Dips in resistance appear when constructive interferences conditions in the cavity are satisfied, $2L = m\lambda_F$. *Right inset:* When the bulk is tuned to electron doping, standing waves are not formed, leading to monotonic resistance. **(c)** Fabry-Pérot diamonds obtained using voltage bias spectroscopy, as shown in color maps of $R(\Omega)$ and its derivative dR_n/dV_b, as function of back gate voltage V_b and voltage bias V_{DC}. Data from sample *B1*. **(d)** R_n plotted versus $2d/\lambda_F$, where d is the effective junction length and λ_F is the Fermi wavelength. By comparing the junction length L to the effective size d extracted from fits, we determined that the contact-doped regions extend at most 100 nm into the channel, consistent with the results of scanning photocurrent studies. Reproducibility of the oscillation period is demonstrated in three devices of length $L = 500$ nm. The blue resistance curve is from sample *B1*, the green curve is from sample *B4*, and the red curve is from sample *B5* and offset by -250 Ω. Resonances marked by dips in resistance appear when constructive interferences conditions are satisfied.

A schematic of a suspended graphene Josephson junction is provided in Figure 5.1a. To access the ballistic regime, we developed a new method to isolate the flake from charge disorder in the underlying dielectric by suspending it over the back gate electrode, described in detail in the Extended Discussion. This approach combines the high purity of suspended devices with superconductivity enables creation of ballistic waveguides where the mean free path l_e of electrons exceeds channel length L. We note that similar results are also obtained on a gate-defined resonator in monolayer graphene encapsulated in hBN, discussed later, which enables a higher degree of electronic control over the cavity while preserving sample quality.

The superconducting leads serve not only as electronic probes but also induce a resonant electron cavity in the scaling limit $l_e > L$ (Fig. 5.1b) [48, 108]. The graphene in the immediate vicinity of the Ti/Al contact is n-doped by charge transfer [114], forming an intrinsic n-n or n-p junction near the interface when the graphene has electron or hole carriers, respectively. We exploit contact induced doping to define the resonator because it is scalable to ultrashort channel lengths, provides electrostatic barriers that are sharp compared to the electron wavelength, and is less complex than gate-defined methods [115–118]. Analogous to an optical Fabry-Pérot cavity, the n-p junctions serve as the electronic counterparts to mirrors while the ballistic graphene channel serves as an electron waveguide. The Fermi wavelength λ_F of electrons in the cavity is directly tunable with a gate electrode which controls the carrier density n.

Fabry-Pérot (FP) resonances in ballistic junctions arise due to reflection from p-n junctions formed near superconducting leads when carrier polarity in the graphene region is opposite to the polarity of contact doping. Figure 5.1b shows a plot of the normal resistance R_n, obtained by sweeping the gate voltage V_b at a fixed bias exceeding I_c. We observe well-resolved resistance oscillations at small positive carrier densities ($V_b < 0$) when

n-p-n junction formation is favored and monotonic behavior when doping is unipolar. The dips in R_n coincide with carrier densities satisfying the constructive interference condition $2d = m\lambda_F$ for electron waves in a resonator, where d is the effective cavity length and m is an integer. Sweeping the gate voltage changes the Fermi energy in the graphene and hence the Fermi wavenumber, given by $k_F = 2\pi/\lambda_F = \sqrt{\pi n}$ for a 2D Fermi disk with fourfold degeneracy. The correspondence to FP interference conditions can be seen more clearly in Fig. 5.1c, which shows that R_n is periodic as a function of $2d/\lambda_F$. Reproducibility of the oscillation period is demonstrated in three devices of 500 nm length (Fig. 5.1c), while shorter junctions exhibit larger periods as expected. Quantum confinement between the cavity "mirrors" gives rise to discrete energy levels with spacing $hv_F/2d$, where $v_F = \hbar k_F/m^*$ is the Fermi velocity and and m^* is the effective electron mass in bilayer graphene. We evaluate this energy scale to be of the order 1 meV using the height of FP diamonds, as measured using voltage bias spectroscopy (Fig. 5.1d).

The interplay between cavity resonances and supercurrent is evident from a resistance colormap as a function of I_{DC} and V_b (Fig. 5.2a-b) showing critical current oscillations whose period satisfies FP interference conditions, consistent with supercurrent propagation via ballistic charge carriers [119]. As λ_F in the cavity is tuned with the gate, the quantum levels of the cavity are moved *on* or *off* resonance with the Fermi energy of the superconducting leads, thus inducing a oscillating critical current periodic in $\sqrt{n}$ for bilayer graphene. This phenomena is observed in two independent systems: (1) suspended bilayer graphene resonators defined by contact-induced doping (Fig. 5.2b) and (2) a gate-defined resonator in monolayer graphene on hBN (Fig. 5.2c and Supplementary Fig. A.11), both of which exhibit similar behavior. In total, five suspended bilayer devices are studied with a lithographic distance L between superconducting contacts of 350 to 500 nm and contact width W of 1.5 to 3.2 μm, in addition to one gate-defined monolayer device with cavity dimensions

of $L = 100$ nm and $W = 2.7$ μm (see Extended Discussion). Figure 5.2c displays critical current modulations in a gate-defined monolayer resonator whose oscillations are periodic in n, in agreement with a monolayer FP model for cavity length ~ 100 nm.

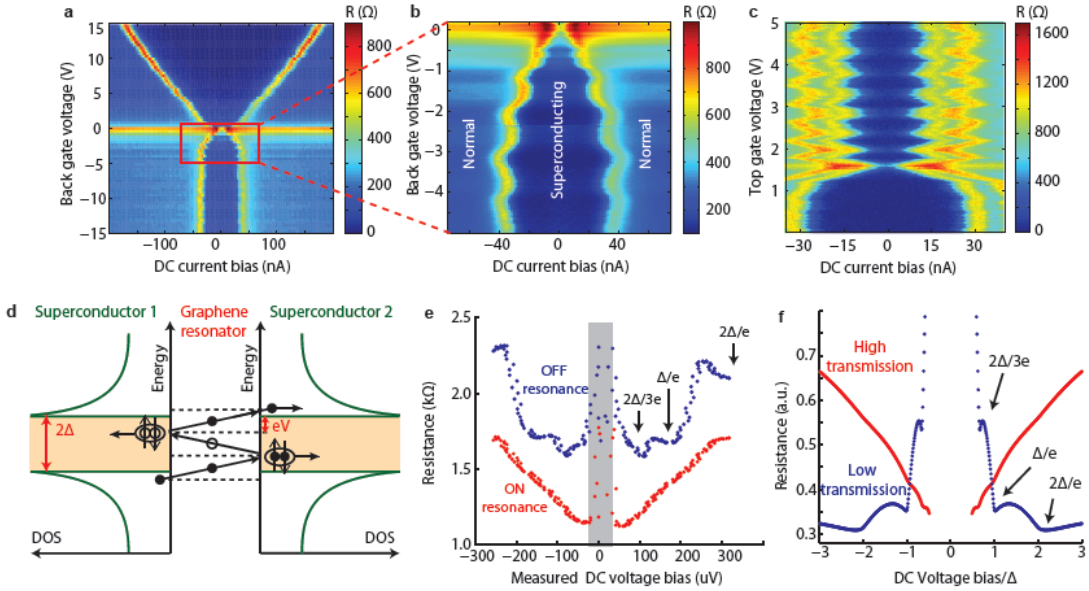

Figure 5.2: **(a, b)** Plots of resistance as a function of DC current bias and back gate voltage. The critical current I_c oscillates with a period that satisfies the Fabry-Pérot (FP) interference conditions, consistent with supercurrent propagation via ballistic charge carriers. **(c)**Differential resistance of a gate-defined FP resonator in monolayer graphene on hBN (device *M1*), as a function of top gate voltage and DC bias current when the back gate voltage is held fixed at -1.75 V. The critical current, defined by the width of zero resistance region along the current axis, oscillates with the same periodicity as normal state resistance, in agreement with a FP model for cavity length ~ 100 nm. **(d)** Schematic illustration of the mechanism of multiple Andreev reflection in a graphene Josephson junction for voltage bias $eV = 2\Delta/3$. **(e)** Line cuts of resistance versus DC voltage bias *on* (V_b=0.3 V, red curve) and *off* (V_b=0.14 V, blue curve) resonance. Well defined MAR peaks appear at $2\Delta, \Delta$, and $2\Delta/3$ when the density is tuned off resonance, while MAR is completely suppressed on resonance. Data is from device *B3*. **(f)**Theoretically obtained conductance profiles in the short junction limit, as a function of applied bias voltage. The curve corresponding to high transmission, G_{high} (red) is computed for a single mode with transmission 0.9. The low transmission curve (blue) is obtained for 4 modes with transmission 0.6. Lower transparencies lead to the formation of conductance resonances at bias voltages corresponding to $2\Delta/3$, Δ, and 2Δ.

5.4 Modulation of multiple Andreev reflection intensity using cavity resonances

We employ yet another property of superconductor-normal-superconductor (SNS) systems to gain insight into the coupling between the cavity modes with the superconducting reservoirs. Because the phenomenon of multiple Andreev reflection (MAR) is known to be extremely sensitive to the coupling between electrons in the normal metal and the superconductor, we use voltage bias spectroscopy to map out the interplay between MAR oscillation amplitude and cavity transmission (Fig. 5.2d-e). The millielectronvolt energy scale associated with FP interference substantially exceeds the Al superconducting gap Δ, allowing one to study the system close to equilibrium conditions for the resonator. A colormap of resistance R_n as a function of applied voltage bias V_{DC} and gate voltage V_b shows modulations due to FP interference (Supplementary Figure A.16). Well defined MAR peaks appear at $2\Delta, \Delta$, and $2\Delta/3$ when the density is tuned off resonance, while MAR is completely suppressed on resonance, as visible in line cuts of resistance on and off resonance in Fig. 5.2e (additional data sets are provided in Supplementary Figs. A.14-A.15). It is notable that the amplitude of the multiple Andreev reflections depends strongly on cavity resonance conditions, thereby providing a direct measure of the tunable coupling between the resonator and the outside world.

The change in visibility of MAR on and off FP resonances is most naturally explained by changes in the distribution of transmission eigenvalues, which can be understood using the following model. Because supercurrent is predominately transmitted by bulk modes, as indicated by the Fraunhofer interferometry data (Supplementary Fig. A.12), we simplify our analysis by focusing on resonances of bulk states. The magnitude of multiple Andreev reflection peaks is small for modes with high transmission probability due to

the absent suppression of higher order scattering processes [120]. In a FP cavity a larger fraction of the current is carried by highly transmitting modes when the cavity is tuned to the resonant wave length. In a short junction different modes contribute independently to the current, producing the observed multiple Andreev reflection pattern. In our junction, $\xi = \hbar v_F/\Delta \approx 450 - 700$ nm, while the junction size is ≈ 350 nm, so we expect the short junction limit to qualitatively hold.

In order to compare this model to the observed experimental data, we have modeled the current through the junction as a sum of contributions of the modes with high ($\sim$ 0.9), medium ($\sim$ 0.6), and low transmission ($\sim$ 0.3) coefficient (Fig. A.17). This separation was chosen to avoid overfitting, while keeping the qualitative features of I-V relationships with different transparencies. We then approximate

$$I(V) = \sum_n \rho(T_n) \cdot I(V, T_n), \tag{5.2}$$

with T_n the transmission probability in various channels, ρ the density of transmission eigenvalues, and $I(V,T)$ the contribution of a single mode with transmission probability T to the total current, calculated in the short junction limit following Ref. [120]. Fitting the model to the measured conductance curves on and off resonance (Fig. 5.2e and Supplementary Fig. A.17) shows that the junction transparency is increased on resonance and suggests good qualitative agreement between this theoretical interpretation and the experiment.

We obtain the estimated contributions of each T_n by fitting the measured I-V traces using the Eq. (5.2) constrained by the condition $\rho(T_n) > 0$. The fits show no systematic error, and increasing the number of T_n leads to noisier fits, indicating overfitting. The coefficient ρ corresponding to large transmissions increase, while the ones corresponding to low transmissions decrease whenever the system is on resonance, at values of the back gate

voltage where the normal state conductance is also peaked (see Supplementary Fig. A.17). The normal state conductance estimated using our model $G_N = g_0 \sum_n T_n \rho(T_n)$ is smaller than the measured one for all back gate voltages, which may be due to deviations from the short junction theory, or the nonlinear behavior of the p-n junctions.

5.5 Visualization of edge and bulk current flow using Josephson interferometry

Next we employ superconducting interferometry as a tool to spatially resolve optics-like phenomena associated with electron waves confined within a ballistic graphene Josephson junction. Unlike experiments in 1D systems [110, 111, 121], one can thread flux through the junction and explore the rich interplay between magnetic interference effects and cavity transmission. Upon application of a magnetic field B, a flux Φ penetrates the junction area and induces a superconducting phase difference $\Delta\varphi(x) = 2\pi\Phi x/\Phi_0 W$ parallel to the graphene/contact interface, where $\Phi_0 = h/2e$ is the flux quantum, h is Planck's constant, and e is the elementary charge. When a flux penetrates the junction area, the critical current $I_c(B)$ exhibits oscillations in magnetic field given by:

$$I_c(B) = \left| \int_{-W/2}^{W/2} J(x) \cdot e^{2\pi i L B x/\Phi_0} dx \right| \tag{5.3}$$

where L is the distance between superconducting electrodes (Fig. 5.1) [23,24]. This integral expression applies in the wide junction limit, relevant for our system, where $L \ll W$ and the current density is only a function of one coordinate. Because the critical current $I_c(B)$ equals magnitude of the complex Fourier transform of the real-space supercurrent distribution $J(x)$, the shape of the interference pattern is determined directly by the spatial distribution of supercurrent across the sample [24, 49].

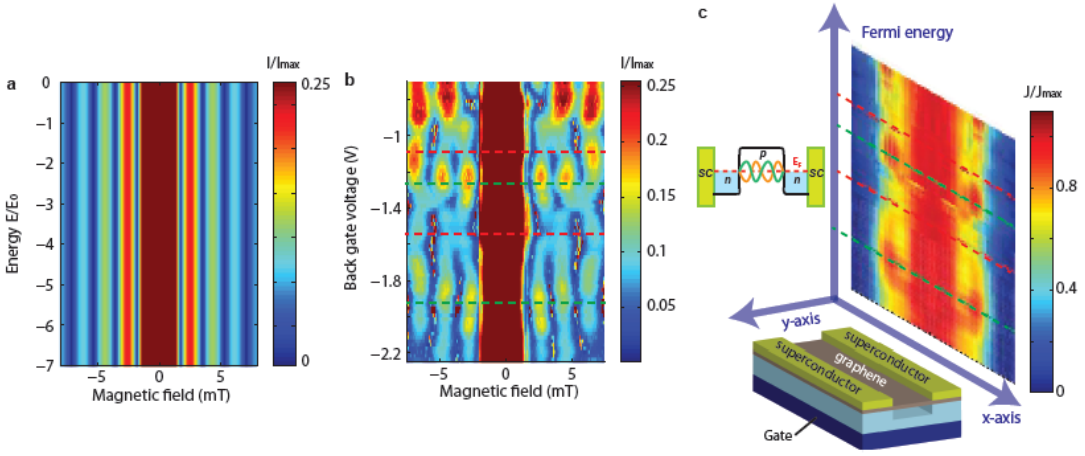

Figure 5.3: **(a)** Theoretical calculation of the superconducting interference pattern for the case of uniform current flow, plotted as the normalize critical current $I_c(B)/I_c(B=0)$. (b) Plot of normalized critical current $I_c(B)/I_c(B=0)$, indicating a nontrivial dependence of superconducting interference on cavity resonances. The value of I_c at each pixel was obtained by measuring the DC voltage V_{sd} across the junction as a function as a function of DC current bias I_{DC} and extracting the maximum derivative dV_{sd}/dI_{DC}. Red and green dotted lines indicate *on* and *off* resonance conditions for the cavity, respectively. Data was collected from device *B2*. **(c)** Real-space normalized supercurrent density distribution $J(x)/J_{max}(x)$ extracted from the $I_c(B)$ data in (b) using Fourier techniques (see Extended Discussion for details).

To visualize current flow associated with interfering electron waves in graphene, we measure supercurrent modulations in B field that arise from a Fraunhofer diffraction. In a conventional graphene Josephson junction with uniform current density, the normalized critical current $I_c(B)/I_c(0) = |\sin(\pi\Phi/\Phi_0)/(\pi\Phi/\Phi_0)|$ is described by Fraunhofer diffraction and should be independent of gate voltage, as depicted in the theoretical plot in Fig. 5.3a. Our results exhibit a striking departure from this picture and feature nodes in $I_c(B)/I_c(0)$ as a function of both V_b and B: Figure 5.3b and Supplementary Fig. A.12 display the different behavior of the normalized interference pattern $I_c/I_c(B=0)$ at gate voltages corresponding to *on* and *off* resonance conditions (labeled by the red and green dotted lines, respectively). Reproducibility of this phenomenon in additional samples is shown in Supplementary Fig. A.13. Using Eq.(5.3), one can extract an effective spatial distribution

of the supercurrent $J(x)$ by taking the inverse Fourier transform of the above $I_c(B)$ line plots with the technique of Dynes and Fulton [24] (see Extended Discussion). As revealed in Fig. 5.3c, the normalized spatial distribution features bulk-dominated current flow *on* resonance and an enhanced edge current contribution *off* resonance.

5.6 Model of superconducting interference in the presence of guided edge states

Inspired by the relation between the spatial current distribution $J(x)$ and critical current $I_c(B)$ in Eq. (5.3), we directly model the spatial distribution of current paths for bilayer graphene in the FP regime (Fig. 5.4a-b). These calculations take into account guided edge modes due to band-bending at the crystal boundaries, which have been experimentally observed in Ref. [109]. This electron guiding effect can be quantified by an edge potential, which is capable of confining carriers to edge-defined 'waveguides' in analogy to the confinement of photons in fiber optic cables. Energies of these edge states lie outside the bulk continuum (Fig. 5.4a), which ensures an evanescent-wave decay of carrier states into the bulk. The resulting states are effectively one-dimensional, propagating as plane waves along the graphene edges. Applying the FP quantization condition in the p-n-p region leads to a sequence of FP maxima positioned at $k_n = \pi n/L$, where n is an integer and L represents distance between superconducting contacts. These quasi-1D states guided along the edge feature head-on transmission and reflection and hence should produce much stronger FP fringes than the bulk states.

As shown in the theoretical dispersion in Fig. 5.4a, the interference conditions in the bulk and at the edge should not coincide due to the difference in the carrier dispersion at the edge and in the bulk as well as due to the angle-dependence of the FP period for the latter

carriers. Hence a gradual increase of doping will trigger repeated switching between the bulk-dominated and edge-dominated regimes, with the current distribution switching from an approximately uniform to edge like, accordingly. Qualitatively, this would be manifested in the dependence of measured critical current on applied magnetic field, switching between Fraunhofer and more SQUID-like behavior (Fig. 5.4b-c).

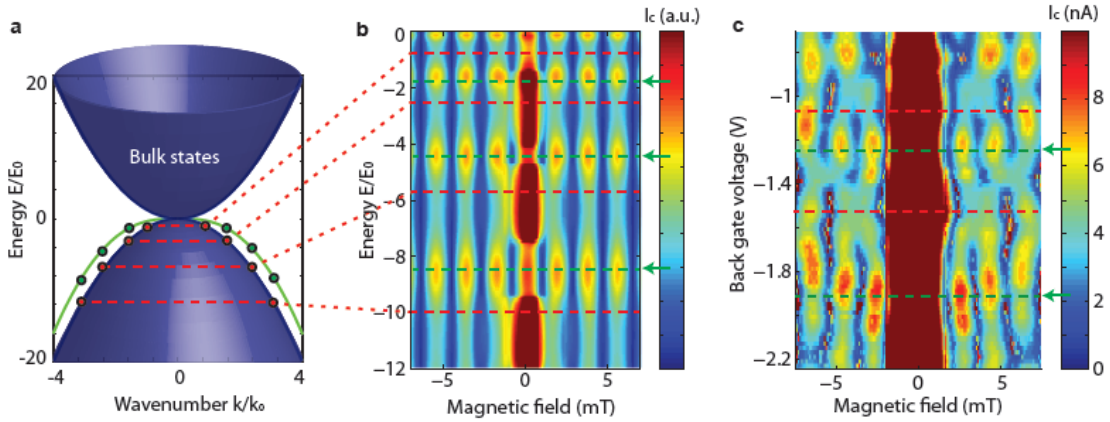

Figure 5.4: **(a)** Spectrum of bilayer graphene with small edge potential, for which one edge mode dominates. In panels (a,b) $p_0 = \lambda m^*/2\hbar$, $E_0 = p_0^2/2m^*$ and $x_0 = \hbar/p_0$ with m^*=0.04 m_e (BLG band mass) and delta function potential strength $\lambda = 0.5$ eV·nm. Energies corresponding to quantized momenta are represented by horizontal red lines. **(b)** Theoretical plot of critical current I_c as a function of barrier energy and applied magnetic field in presence of edge modes. Bulk and edge currents produce distinct FP patterns due to different dispersion laws and angle dependent transmission of bulk modes. **(c)** Plot of critical current I_c as a function of back gate voltage V_b and applied magnetic field B. Red and green dotted lines indicate on and off resonance conditions, respectively. Data was collected from device *B2*.

To quantify these phenomena, we model FP resonances using the approach described in Ref. [109]. Assuming that the edge potential is sufficiently short-ranged, we approximate it with a delta function. We obtain the density of persistent current along the edge (chosen to be along y axis) from the exact Green's function G in a mixed coordinate-

momentum representation:

$$j(\varepsilon, x) = -\frac{\pi}{\mathrm{Im}} \sum_{k_y, x'=x} \Big[G(\varepsilon, x, x', k_y) J_y \Big] \tag{5.4}$$

where J_y is the operator for current along the edge (see Eq. (8-9) in supplement of Ref. [109]). The sum in Eq.(5.4) runs over the values $k_n = \pi n/L$ for one sign of n. Each term in Eq.(5.4) has poles corresponding to bounded states for the momentum value k_n, each of which corresponds a to current maximum at the edge. To translate this into an experimentally observable quantity, we model Fraunhofer interference pattern $I_c(B)$ using the theoretical amplitude and spatial distribution of edge modes (see Extended Discussion). This result, plotted in Fig. 5.4b, captures the key features of the raw data in Fig. 5.4c, namely the redistribution of current on and off resonance as well as the suppression of side lobes' intensity on resonance. Thus, the measurements are consistent with a model that features separate FP interference of guided-wave edge currents, in parallel to interference of bulk modes. This further suggests that the quasi-1D edge currents previously observed [109] have ballistic character. Despite its simplified nature, which neglects disorder and finite temperature effects, our model captures the essential features of the measurements. While the edge potential featured in this simulation accommodates a single edge channel, we note that the number of guided modes may exceed one for stronger potentials. In this case, each mode would contribute independently to the interference pattern, giving rise to fringes with complicated multi-period structure at the edge.

In summary, we utilize different aspects of proximity-induced superconductivity, particularly Fraunhofer interferometry and Andreev scattering, as new tools to resolve optics-like phenomena associated with electron waves confined within a ballistic graphene Josephson junction. This enables real-space visualization of cavity modes in a graphene

FP resonator, which reveals surprising redistribution of current on and off resonance and provides direct evidence of the ballistic nature of guided edge currents. These results constitute a strong departure from conventional Josephson behavior in graphene and motivate further exploration of new effects at the intersection of superconductivity and optics-like phenomena.

5.7 Extended Discussion

Theoretical model of ballistic supercurrent in a graphene Fabry-Pérot resonator

Here we consider a graphene SNS junction in which Fabry-Pérot (FP) interference and oscillations arise due to a pair of p-n junctions which act as mirrors of an electron FP resonator. There are two kinds of propagating electronic states in this system: one-dimensional edge modes and two-dimensional bulk modes. We first analyze the contribution to supercurrent due to the edge modes and subsequently consider the bulk modes.

In our analysis we assume electron wavelength values much smaller than the junction length, $\lambda \ll L$, which allows us to use the semiclassical approximation. In the experimental regime of interest the carrier density in graphene varies in the range $(2.5-6.0)\times 10^{10}$ cm^{-2} corresponding to wavelength values $0.14-0.22$ micron, which is a few times smaller than the junction length $L = 0.35$ μm. We therefore expect the semiclassical approach to provide a reasonably good starting point.

The contribution of ballistic modes to supercurrent is described by theory originally derived by Kulik and subsequently explored by other researchers [122–125]. In the semiclassical regime the supercurrent is given by [124]

$$j(\varphi) = \frac{e\Delta}{\hbar}\sum_{k=1}^{\infty}(-1)^{k+1}\frac{L}{\xi}\frac{\sin k\varphi}{\sinh\frac{kL}{\xi}} \tag{5.5}$$

where Δ is the order parameter in the leads and, for the sake of clarity, we suppress an order-one prefactor. Here the phase φ accounts for both the phase difference $\Delta\varphi$ between superconducting leads and the Aharonov-Bohm phase gained by a pair of Andreev quasiparticles in the presence of a magnetic vector potential $\mathbf{A}$:

$$\varphi = \Delta\varphi + \frac{2e}{\hbar c}\int_1^2 \mathbf{A}(\mathbf{r})d\mathbf{r}, \quad \mathbf{A}(\mathbf{r}) = (-By, 0, 0) \tag{5.6}$$

where the integral is taken along the pair trajectory. Here we analyze a rectangular system $0 < x < L$, $0 < y < W$, focusing on the modes propagating along system edges $y = 0$ and $y = W$. Evaluating the integral $\int_1^2 \mathbf{A}(\mathbf{r})d\mathbf{r}$ we find the phase value $-2\pi\Phi/\Phi_0$ for the $y = W$ edge and zero for the $y = 0$ edge (here $\Phi = BLW$ is the magnetic flux through the system and $\Phi_0 = hc/2e$ is the magnetic flux quantum).

The result in Eq.(5.5), which is valid in the absence of backscattering, can be generalized to the FP resonator case by introducing scattering matrices S_e and S_h for the electrons and the corresponding Andreev-reflected holes. Scattering of the electrons originating in contact 1 and moving to contact 2 and of the back-reflected holes moving from 2 to 1 can be described by the matrices

$$S_e = \begin{bmatrix} R & T'\mathrm{e}^{-i\delta} \\ T\mathrm{e}^{i\delta} & R' \end{bmatrix}, \quad S_h = \begin{bmatrix} \bar{R} & \bar{T}\mathrm{e}^{i\delta} \\ \bar{T}'\mathrm{e}^{-i\delta} & \bar{R}' \end{bmatrix} \tag{5.7}$$

where $\delta = \varphi/2$. The form of S_e and S_h guarantees that $S_h S_e = 1$ for $\delta = 0$, which corresponds to fully coherent Cooper pair transmission through the N region. Here R and T are the FP scattering amplitudes

$$T = \frac{t_1 t_2 e^{iD}}{1 - r_1 r_2 e^{2iD}}, \quad R = r_1' + \frac{t_1 t_1' r_2 e^{2iD}}{1 - r_1 r_2 e^{2iD}}, \tag{5.8}$$

and $R' = -\bar{R}$, $T' = \bar{T}$ denote scattering amplitudes for propagation in the reverse direction (the quantity $D = p_F L$ denotes the one-way optical path in the FP resonator, with p_F the Fermi momentum inside the pnp region). Here the transmission and reflection amplitudes for individual pn junctions satisfy the unitarity conditions:

$$t_i' = \bar{t}_i \qquad r_i' = -\bar{r}_i \qquad |r_i|^2 + |t_i|^2 = 1 \tag{5.9}$$

from which it follows that the scattering matrices S_e and S_h comprised of the compound FP amplitudes (5.8) are unitary.

To combine the S-matrices (5.7) with Eq.(5.5) we note that different terms in this equation describe processes involving repeated transmission of several Cooper pairs. The total scattering matrix for a Cooper pair passing through the junction is $S_{he} = S_h S_e$. Accordingly, the contribution to current corresponding to the $k = 1$ term in Eq.(1)(5.5) is given by a single pair transmission:

$$j_1 \sim \frac{1}{2i}((S_{he})_{11} - (S_{he})_{22}) = \frac{1}{2i}\mathrm{Tr}\ (\sigma_z S_{he}) = |T|^2 \sin\varphi. \tag{5.10}$$

By analogy, the contribution of a repeated transmission of two pairs corresponding to $k = 2$ in Eq.(5.5) can be written as

$$j_2 \sim \frac{1}{2i}\mathrm{Tr}\ \left(\sigma_z S_{he}^2\right) = |T|^4 \sin 2\varphi + 2|T|^2|R|^2 \sin\varphi. \tag{5.11}$$

Here the first term describes the contribution of two sequentially transmitted pairs, whereas the second term describes the contribution of two pairs only one of which made it though the resonator. Generalizing these observations to processes of higher order, we can write

the contribution of k pairs as

$$j_k \sim \frac{1}{2i}\mathrm{Tr}\left(\sigma_z S_{he}^k\right) = \sum_{m=0}^{k} a_m \sin m\varphi \tag{5.12}$$

where $a_k = |T|^{2k}$, $a_{k-1} = k|T|^{2(k-1)}|R|^2$, ... The net current is then given by a sum of all partial contributions with different k values as follows

$$j = \frac{e\Delta}{\hbar}\mathrm{Im}\sum_{k=1}^{\infty}(-1)^{k+1}\frac{L}{\xi}\frac{\mathrm{Tr}\left[\sigma_z(S_h S_e)^k\right]}{\sinh\frac{kL}{\xi}} \tag{5.13}$$

which for unit transmission $T = T' = 1$, $R = -R' = 0$ matches Eq.(5.5) (here again we suppress an order-one prefactor).

Proceeding with the analysis of Eq.(5.13) we note that for ballistic dynamics the correlation length is defined as $\xi = \hbar v_F/2\pi kT$. For experimental temperature $T \approx 10$ mK and densities $(2.5-6.0)\times 10^{10}$ cm^{-2} this yields values $\xi \sim 10-20\,\mu$m which are substantially larger than system dimension $L = 0.35$ μm. For $\xi \gg L$ we can approximate

$$\frac{L}{\xi\sinh\frac{kL}{\xi}} \approx \frac{1}{k}$$

and perform summation over k in Eq.(5.13) to obtain

$$j = \frac{ev_F}{\lambda_F}\mathrm{Im}\mathrm{Tr}\left[\sigma_z \ln(1 + S_h S_e)\right] \tag{5.14}$$

Combining the contributions of the $y = 0$ and $y = W$ edges in a single expression, we have

$$I_e = \eta(E_F)\Big\{j(\Delta\varphi) + j(\Delta\varphi - 2\pi\Phi/\Phi_0)\Big\} \tag{5.15}$$

where η is a dimensionless parameter depending on the edge potential strength.

To describe the contribution of the bulk modes we need to account for the contributions of various oblique trajectories. Since the junction length $L = 0.35$ μm is considerably smaller than its width $W = 1.7$ μm, we focus on the wide junction limit $W \gg L$ and neglect the boundary effects. In this case the only relevant characteristic of a trajectory is its angle relative to the pn interfaces and contacts. Denoting by θ the angle relative to x axis we write the net contribution of the bulk modes to supercurrent as

$$I_b = p_F \int_0^W dy \int_{-\pi/2}^{\pi/2} d\theta \cos\theta j(\varphi(y), \theta), \tag{5.16}$$

$$\varphi(y) = \Delta\varphi - 2\pi \frac{\Phi(y)}{\Phi_0}, \quad \Phi(y) = BWy, \tag{5.17}$$

where y parameterizes the trajectory transverse displacement (along the y axis) and $j(\varphi(y), \theta)$ is the current along the trajectory given by a suitable generalization of Eq.(5.14) (here again we suppress an order-one prefactor in the expression for I_b).

The increased length of oblique trajectories can be accounted for via $L \to \tilde{L} = L/\cos\theta$, whereas the optical path that controls the FP interference is obtained as

$$D \to \tilde{D} = p_F L \cos\theta \mp \frac{\pi B L^2}{2\Phi_0} \tan\theta. \tag{5.18}$$

Here we accounted for the opposite Aharonov-Bohm phases gained by an electron and a hole in the presence of a magnetic field (for $L \ll W$ this is a small effect compared to the y-dependent phase in Eq.(5.17)).

The transmission and reflection of the individual pn interfaces are given by the functions of the incidence angle θ accounting for Klein scattering, as appropriate for the monolayer and bilayer graphene.

The net critical current used to obtain Fig. 5.4b of the main text is given by

$$I_c = \max_{\Delta\varphi}(I_e(\Delta\varphi) + I_b(\Delta\varphi)) \tag{5.19}$$

We note parenthetically that in general the Fermi momentum takes different values inside and outside the FP resonator. The same is true for the inner and outer incidence angles, which satisfy $p_F \sin\theta = p'_F \sin\theta'$ (here the primed variables correspond to the region outside the resonator). For the inner incidence angle varying in the range $-\pi/2 < \theta < \pi/2$ the outer incidence angle varies in the range $-\theta'_{\max} < \theta' < \theta'_{\max}$, where

$$\theta'_{\max} = \begin{cases} \arcsin(p_F/p'_F) & p_F < p'_F \\ \pi/2 & p_F \geq p'_F \end{cases} \tag{5.20}$$

These relations guarantee that the mode counting performed using p_F and θ in a crosssection inside the pnp region yields the results identical to those found from the mode counting performed outside the pnp region (with p'_F and θ' used in place of p_F and θ).

Fabrication and design of ballistic graphene Josephson junctions

- *Suspended Josephson junctions*:

We investigate suspended Josephson junctions of two types. The first type, which corresponds to data shown in Fig. 5.1 and 5.2a-b, features superconducting electrodes in the interior of the flake. Graphene is mechanically exfoliated directly onto on a 300 nm SiO_2 dielectric layer that coats a doped silicon wafer serving as a global back gate. Next, thin Cr/Au leads are defined using e-beam lithography in a pseudo-four probe geometry in order to make electrical contact to the bilayer graphene device. These contacts are spaced

roughly 1-1.5 μm apart in order to leave room for the superconducting contacts that will eventually define the Josephson junction itself. These Cr/Au (3/30 nm) contacts are deposited using thermal evaporation, followed by immersion in acetone for metal liftoff. Next, thick gold electrodes are defined in a way that overlaps the outer edges of the thin contacts, thus maintaining electrical contact to the flake. The thick electrodes serve a dual purpose: (1) to provide structural support and mechanically hold up the entire suspended graphene Josephson junction and (2) provide an electrical connection between the Josephson junction and the bondpads. After an evaporation mask is defined using e-beam lithography, Cr/Au (3/200 nm) is deposited. To define the Josephson junction, a pair of rectangular Ti/Al superconducting contacts are patterned in the interior of the flake and extending over the thin Cr/Au leads to maintain electrical contact to the bondpads. The superconducting electrodes are patterned using e-beam lithography, followed by thermal evaporation of a 10 nm Ti adhesion layer and a 70 nm superconducting Al layer. Finally, in order to protect the superconductor from degradation in acid during the suspension process, a PMMA polymer etch mask is defined over the superconducting contacts using e-beam lithography. After development, the entire chip is immersed in a buffered oxide wet etchant to remove 150 nm of the underlying SiO_2 dielectric layer, leaving the Josephson junction fully suspended. Immediately following the etch, the substrate is immersed in methanol, followed by an acetone soak to dissolve the PMMA mask, after which the chip is again immersed in methanol and dried in a critical point dryer.

The second type of suspended Josephson junction, which corresponds to the data in Fig. 5.2e-f and Fig. 5.3, features superconducting electrodes that extend over the full width of the flake. This Josephson geometry is preferable for imaging current flow due to the uniform distance between contacts and rectangular junction dimensions. Devices are fabricated on a 300 nm SiO_2 dielectric layer that coats a doped silicon wafer that serves as

a global back gate. Bilayer graphene flakes are deposited over predefined narrow trenches that are etched into the SiO_2 with a depth of 150 nm. Next, thin Cr/Au contacts and bondpads are defined using e-beam lithography in a pseudo-four probe geometry in order to make electrical contact to the bilayer graphene device. These contacts are spaced far apart on either side of the etched trench in order to leave room for the superconducting contacts that will eventually define the Josephson junction itself. These Cr/Au (3/30 nm) contacts are deposited using thermal evaporation. The devices are then immersed in acetone for metal liftoff, transferred immediately into methanol, and carefully dried using a critical point dryer due the delicate nature of suspended graphene membranes. To construct the Josephson junction, superconducting Ti/Al contacts are patterned along the trench edges using e-beam lithography and with width large enough to achieve electrical contact with the Cr/Au leads. The superconducting contacts are deposited using thermal evaporation with the following procedure: a 10 nm Ti adhesion layer is deposited, followed by a 50 nm layer of Al superconductor. As with the previous step, metal liftoff is conducted by immersion in acetone and methanol, followed by drying in a critical point dryer. The motivation for using Cr/Au bondpads is to achieve the best possible electrical connection to the gold bonding wires and sample holder pins. Aluminum, by contrast, oxidizes upon exposure to air and forms intermetallic compounds at the interface with gold bonding wire, which would be expected to degrade electrical contact. Devices are current annealed in vacuum at dilution refrigerator temperatures in order to remove organic processing residues and enhance quality. All low temperature data is collected using standard lockin measurement techniques in a Leiden Cryogenics Model Minikelvin 126-TOF dilution refrigerator with a base temperature of ~ 10 mK.

- *Suspended Josephson junction device dimensions*:

Sample *B1*: Fig. 5.1b, 5.1d, the blue curve in Fig. 5.1c, and Fig. 5.2a-b. Type 1 geometry. Distance between superconducting electrodes: 500 nm. Width of superconducting contacts (defines transverse dimension of junction): 1.7 μm.

Sample *B2*: Fig. 5.3b-c, Fig. 5.4c, and Supplementary Fig. A.12: Type 2 geometry. Distance between superconducting electrodes: 350 nm. Junction width: 1.7 μm.

Sample *B3*: Fig. 5.2e-f, Supplementary Fig. A.15: Type 2 geometry. Distance between superconducting electrodes: 350 nm. Junction width: 1.7 μm. Note: Data sets *B2* and *B3* are from the same physical device but are collected after different current annealing iterations and thus have different disorder configurations.

Sample *B4*: Fig. 5.1c: green curve. Type 1 geometry. Distance between superconducting electrodes: 500 nm. Width of superconducting contacts (defines transverse dimension of junction): 3.2 μm.

Sample *B5*: Fig. 5.1c: red curve. Type 1 geometry. Distance between superconducting electrodes: 500 nm. Width of superconducting contacts: 1.65 μm.

Sample *B6*: Supplementary Fig. A.13-A.14: Type 2 geometry. Distance between superconducting electrodes: 350 nm. Junction width: 1.5 μm.

Sample *B7*: Supplementary Fig. A.13: Type 2 geometry. Distance between superconducting electrodes: 350 nm. Junction width: 1.5 μm. Note: Data sets *B6* and *B7* are from the same physical device but are collected after different current annealing iterations and thus have different disorder configurations.

- *Josephson junctions on hBN*:

To investigate a separate device design, the gate-defined FP cavity, we also consider one dual-gated monolayer graphene Josephson junction encapsulated in hexangonal boron nitride (hBN). By isolating the graphene from the surface roughness and charge disorder

associated with the underlying silicon dioxide gate dielectric, hBN substrates enable high device quality to be achieved, which is a crucial ingredient for observing ballistic charge transport. This Josephson junction has a distance of 750 nm between the superconducting contacts and a flake width of 2.7 μm. The top gate length, which defines the size of the FP resonator, is ∼100 nm. The superconducting electrodes consist of an adhesion layer of Ti (10 nm) and a superconducting layer of Al (60 nm). The top gate consists of Ti/Au (5/50 nm). The thicknesses of the top and bottom hBN flakes that encapsulate the graphene are ∼19 nm and ∼30 nm, respectively, as measured by atomic force microscopy (AFM).

- *Encapsulated Josephson junction device dimensions*:

Sample *M1*: Fig. 5.2c, Supplementary Fig. A.11: Distance between superconducting electrodes: 750 nm. Junction width: 2.7 μm. The top gate length: ∼100 nm.

Fourier method for extraction of supercurrent density distribution

In order to disentangle edge from bulk current flow through the resonator, we employ the Fourier techniques of Dynes and Fulton to reconstruct the real-space supercurrent distribution from the magnetic interference pattern $I_c(B)$. This procedure, described in detail in Ref. (10) of the main text, is briefly summarized here. When a magnetic field B is applied perpendicular to the junction area, the critical current $I_c(B)$ through a Josephson junction is:

$$I_c(B) = |\mathcal{I}_c(B)| = \left| \int_{-\infty}^{\infty} J(x) \exp(2\pi i (L + l_{Al}) B x / \Phi_0) dx \right| \tag{5.21}$$

where x is the dimension along the width of the superconducting contacts (labeled in Fig. 5.1), L is the distance between contacts, l_{Al} is the magnetic penetration length scale (determined by the London penetration depth of the superconductor and flux focusing), and $\Phi_0 = h/2e$ is the flux quantum. This integral expression applies in the narrow junction

limit where $L \ll W$, relevant for our system.

Observing that $\mathcal{I}_c(B)$ represents the complex Fourier transform of the current density distribution $J(x)$, one can apply Fourier methods to extract the spatial structure of current-carrying electronic states. Because the antisymmetric component of $J(x)$ vanishes in the middle of the junction, the relevant quantity for analyzing edge versus bulk behavior is the symmetric component of distribution. By reversing the sign of $I_c(B)$ for alternating lobes of the superconducting interference patterns, we reconstruct $\mathcal{I}_c(B)$ from the recorded critical current. One can determine the real-space current density distribution across the sample by computing the inverse Fourier transform:

$$J_s(x) \approx \int_{-\infty}^{\infty} \mathcal{I}_c(B) \exp(2\pi i(L + l_{Al})Bx/\Phi_0) dB \tag{5.22}$$

We employ a raised cosine filter to taper the window at the endpoints of the scan in order to reduce convolution artifacts due to the finite scan range $B_{min} < B < B_{max}$. This the explicit expression used is:

$$J_s(x) \approx \int_{B_{min}}^{B_{max}} \mathcal{I}_c(B) \cos^n(\pi B/2L_B) \exp(2\pi i(L + l_{Al})Bx/\Phi_0) dB \tag{5.23}$$

where $n = 0.5 - 1$ and $L_B = (B_{max} - B_{min})/2$ is the magnetic field range of the scan.

Appendix A

Supplementary Figures

A.1 Supplementary Figures for Chapter 3

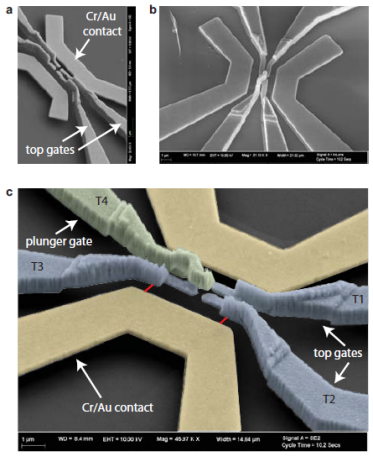

Figure A.1: **(a)** Tilted SEM image of a four gate quantum dot device. **(b)** SEM image of a three gate quantum dot taken with the Inlens detector. An additional plunger gate used to control the density in the dot is suspended above the lower gates. The suspended graphene bilayer is faintly visible below the gates. **(c)** Colored SEM image of a device similar to that pictured in (b) taken with the SE2 detector. Red lines mark the estimated graphene boundaries. The gate geometry is nearly identical to that of device *D2*, and the top gate labeling that accompanies the data in Fig. 3.4b is provided here.

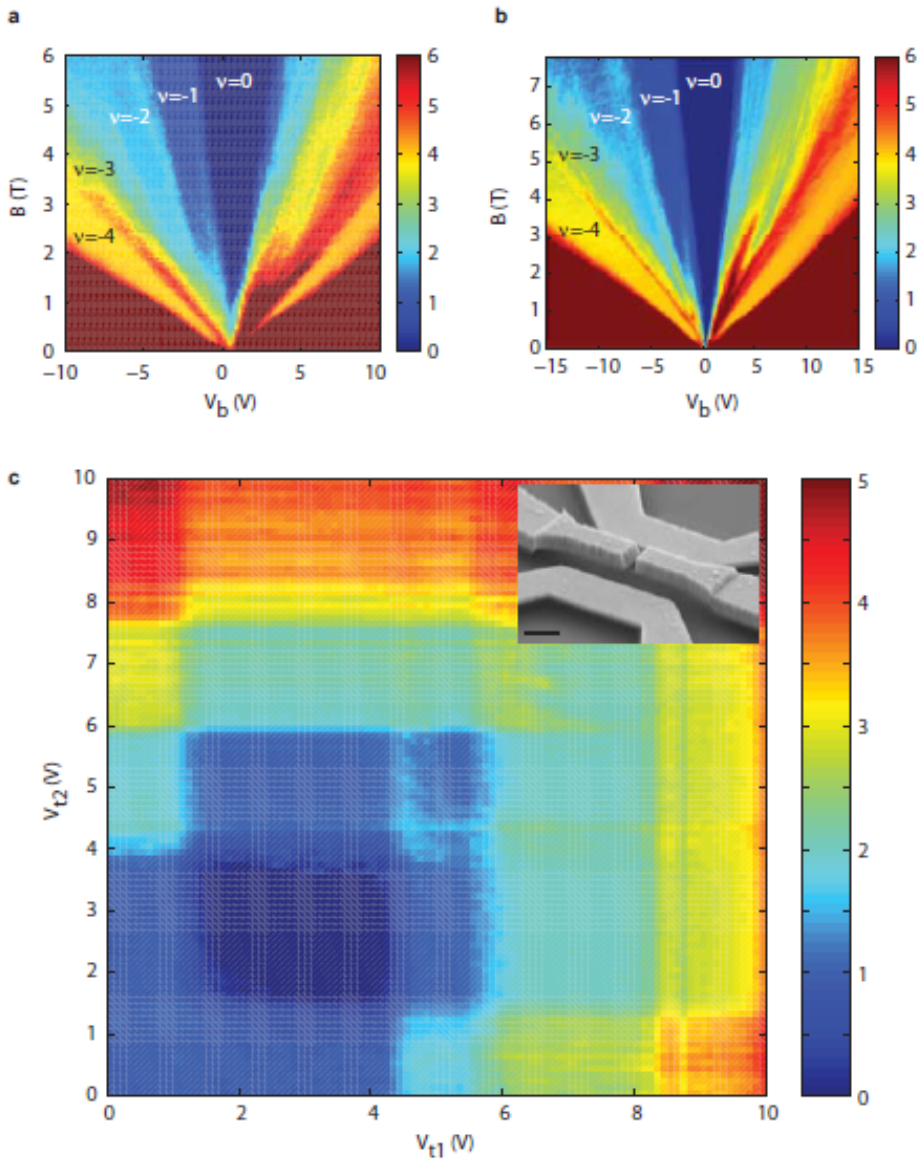

Figure A.2: **(a)** Landau fan in device *D4* plotted as conductance (in units of e^2/h) as a function of back gate voltage V_b and magnetic field B. All top gates are fixed at zero volts. **(b)** Landau fan in a two gate split-gate device with zero voltage on the top gates. **(c)** Conductance map (in units of e^2/h) of the device in part (b) as a function of the voltages on each split top gate. The voltage $V_b = -3$V and field $B = 4$T are held constant. This provides direct evidence of local control over broken symmetry quantum Hall states in suspended bilayer graphene. *Inset*: Scanning electron micrograph of the split gate device featured in parts (b) and (c). The scale bar represents 1 μm.

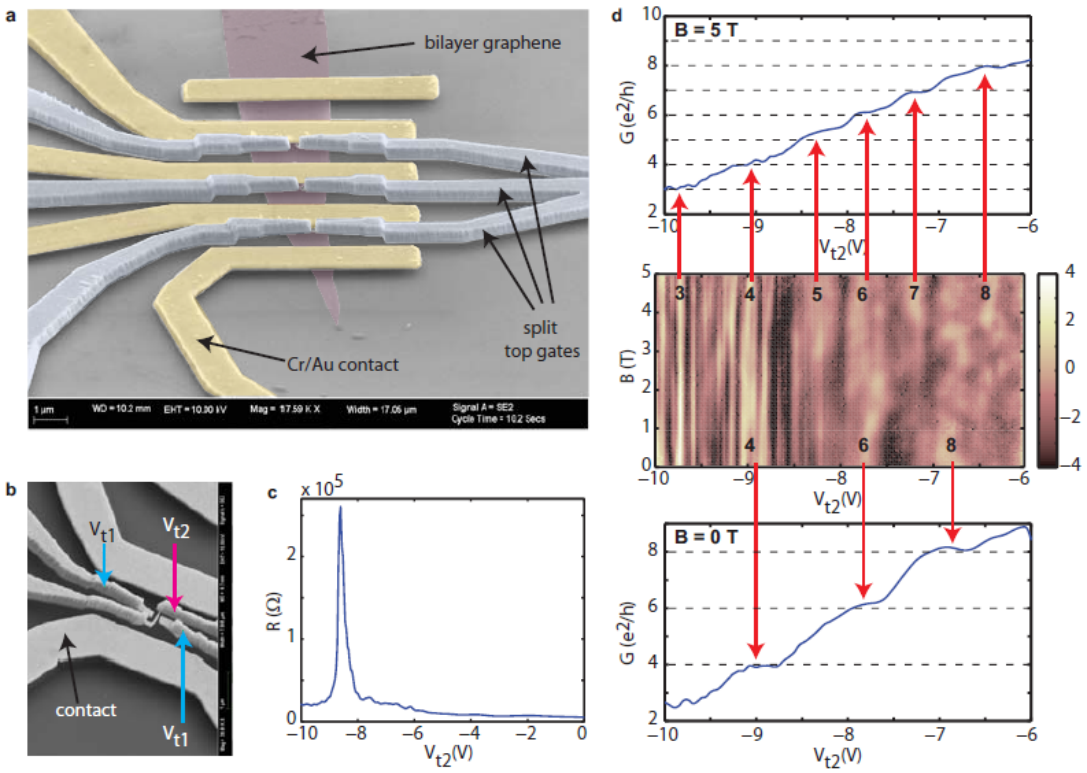

Figure A.3: By opening a bandgap beneath local top gates in a quantum point contact (QPC) geometry, electron transport is restricted to conductance through the constriction. **(a)** Tilted false-color SEM image of three suspended QPC devices in series. **(b)** SEM image of fully suspended QPC with 200 nm between split gates (labeled with blue arrows). The central gate (labeled with a pink arrow) tunes the carrier density in the channel. Beneath the split side gates, one may induce a bandgap by applying a perpendicular E field, meanwhile fixing the top and back gate voltages, V_{t1} and V_b, at a ratio that places the Fermi energy near the center of the gap. Application of voltage V_{t2} to the central gate independently tunes the carrier density within the channel, enabling one to sweep the Fermi wavelength for a fixed constriction width. **(c)** Pinching off of the constriction at $B = 0$ is illustrated. This is a plot of conductance (in units of e^2/h) versus central gate voltage, V_{t2}. The split gates are fixed at $V_{t1} = -9.75$ V and the back gate is at $V_b = 11.4$ V. **(d)** Plot of conductance in units of e^2/h versus central gate voltage, V_{t2}, in a device similar to that pictured in part b. The split gates are fixed at $V_{t1} = -10$ V and the back gate is at $V_b = 11.9$ V. At $B = 0$ conductance steps are visible at values of 4, 6, and 8 e^2/h (bottom panel), while steps energe at integer multiples of e^2/h in the presence of an in-plane magnetic field of $B = 5$ T (top panel). This behavior is suggestive of a broken valley degeneracy at $B = 0$ and the gradual breaking spin degeneracy with increasing magnetic field. The central panel, a plot of $\Delta G/\Delta V_{t2}$, shows the gradual emergence of the integer steps over a 5 T field range.

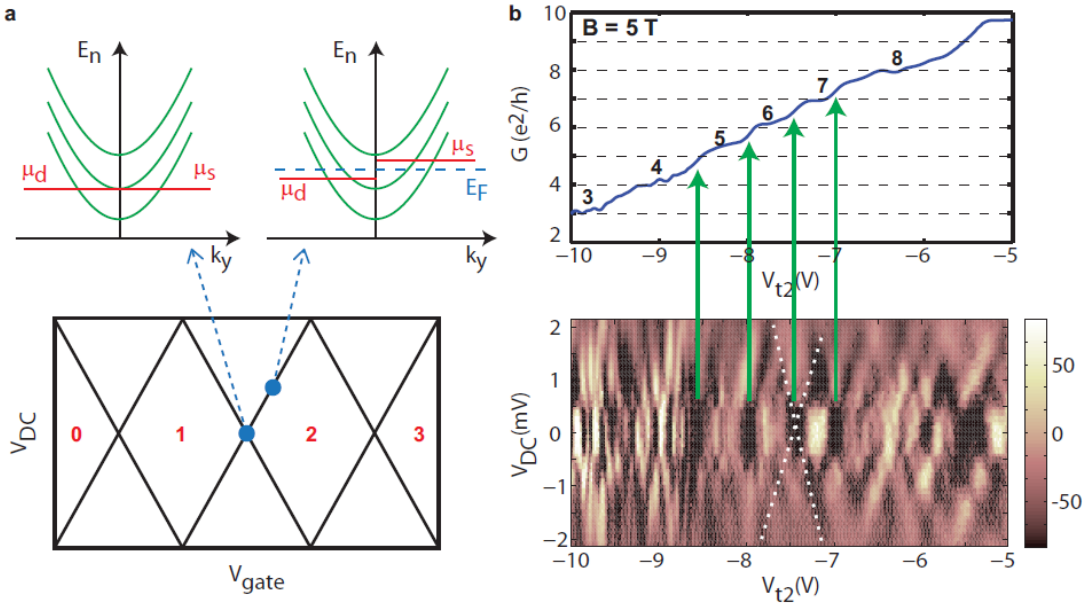

Figure A.4: **(a)** Schematic of DC bias behavior for a QPC. The black lines in the bottom panel represent transitions between conductance plateaus as a function of V_{gate} and V_{DC}. The energy diagrams in the upper panels show placement of the source and drain chemical potentials (μ_s, μ_d) relative to the one-dimensional subbands at the locations marked with blue circles. **(b)** Plot of conductance in units of e^2/h versus central gate voltage (labeled V_{t2}) in a device similar to that pictured in Fig. A.2b. Steps emerge at integer multiples of e^2/h in the presence of an in-plane magnetic field of $B = 5$ T (top panel). A map of $\Delta G/\Delta V_{t2}$ as a function of DC bias and central gate voltage exhibits behavior consistant with conductance quantization, though the features are obscured by Fabry-Perot like interference patterns

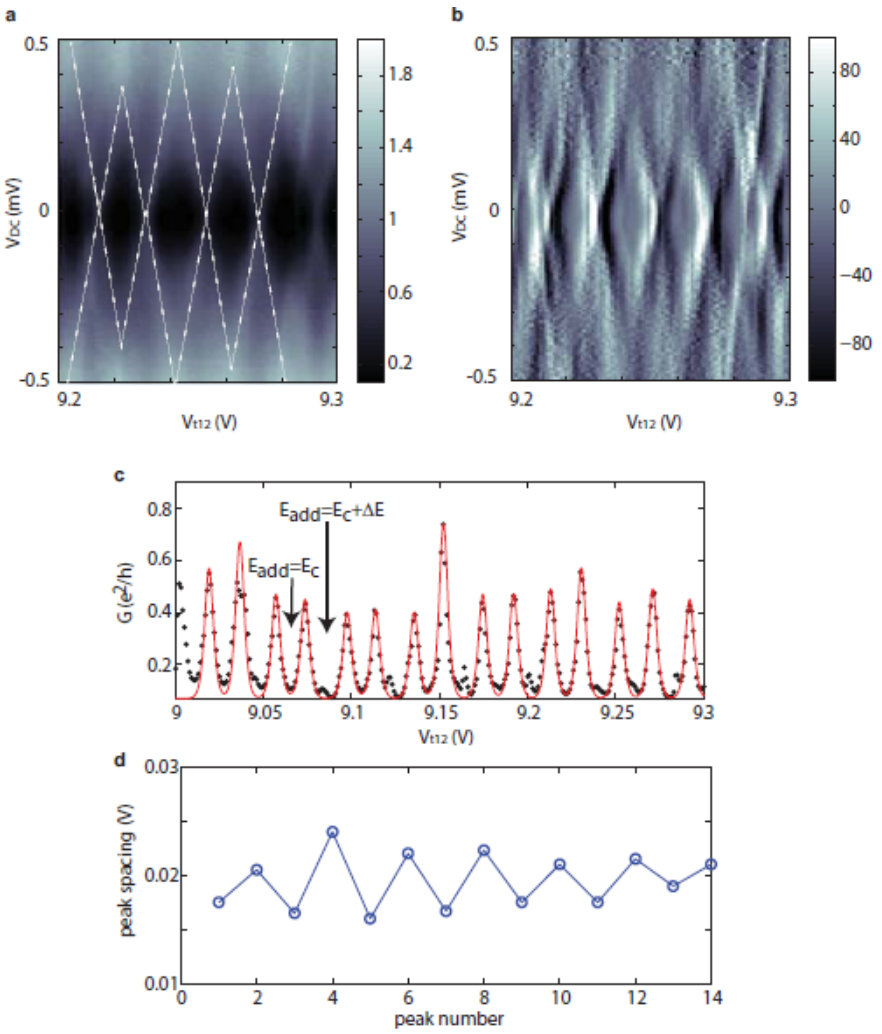

Figure A.5: **(a)** Coulomb diamonds in device *D4* are shown in a plot of G as a function of V_{t12} and V_{DC}, where G is conductance in units of e^2/h and V_{DC} is the DC bias across the electrodes. The voltages $V_b = -10.7$V and $V_{t34} = 9.27$ V are held constant. **(b)** Plot of $\Delta G/\Delta V_{t12}$ for the data in part (a). **(c)** Even-odd effect visible in a conductance plot (units of e^2/h) of Coulomb blockade oscillations as a function of V_{t12} at fixed $V_b = -10.7$V and $V_{t34} = 9.27$V. Black points represent data and the red line indicates a functional fit used to extract peak positions. In the presence of a two-fold degeneracy, the constant interaction model yields electron addition energy $E_{add} = E_C$ for N odd and $E_{add} = E_C + \Delta E$ for N even (for charging energy E_C and orbital energy spacing ΔE) because electrons of opposite index can occupy a single orbital state. **(d)** Peak spacing (in volts) as a function of peak number for the fitted data in part (c).

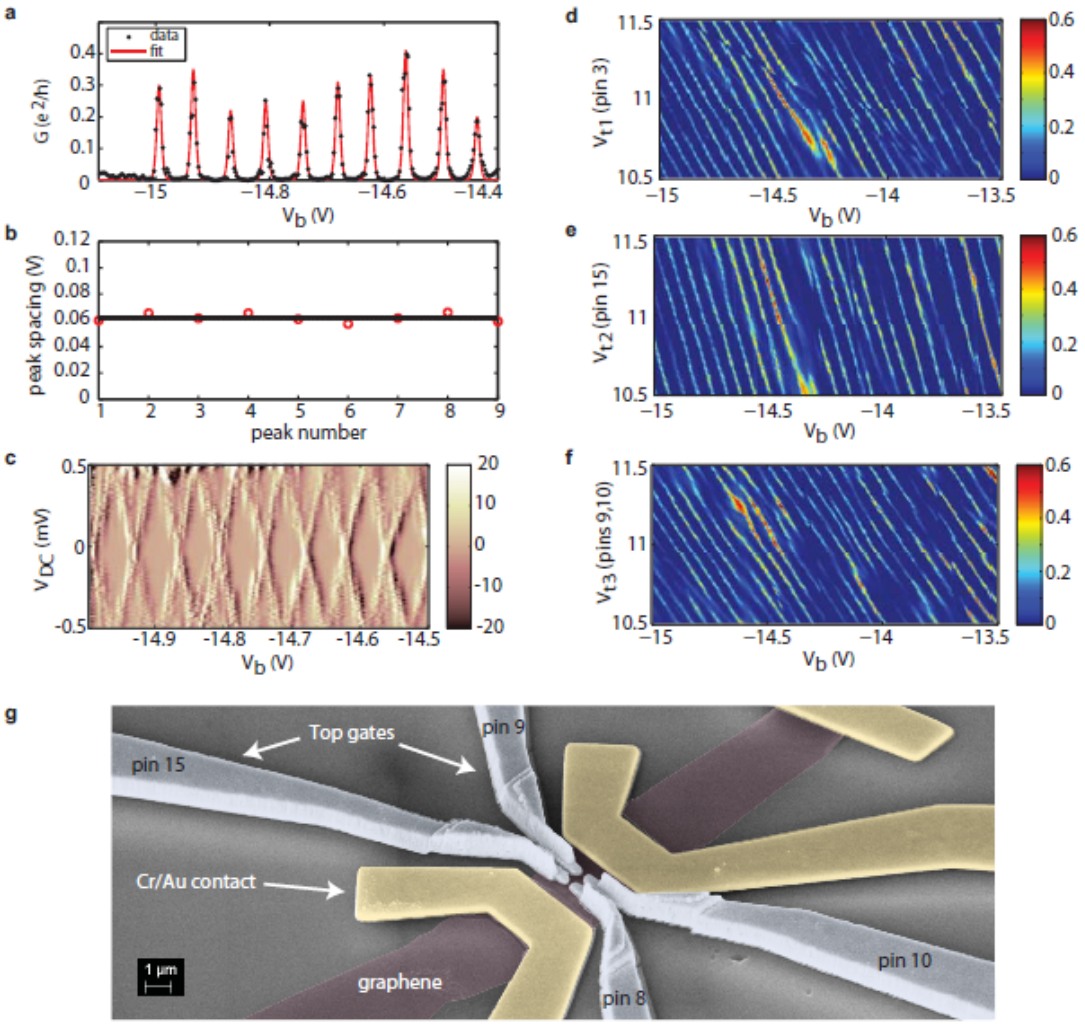

Figure A.6: **(a)** Coulomb blockade peak conductance vs. back gate voltage V_b at $B = 7$ T. Top gate voltages are $V_{t1} = V_{t3} = 11$ V and $V_{t2} = 10.5$ V. **(b)** Peak spacings for the data in part a. **(c)** Coulomb diamonds in a plot of $\Delta G/\Delta V_b$, where G is conductance in units of e^2/h and V_{DC} is the DC bias across the contacts. **(d-f)** Conductance(e^2/h) of Coulomb blockade peaks vs. V_{t1}, V_{t2}, and V_{t3}, respectively. Similar coupling to each top gate suggests a centrally located dot. **(g)** False-color scanning electron micrograph of a dot similar to *D3*. Voltages V_{t1}, V_{t2}, and V_{t3} are applied to pins 3, 15, and 9&10, respectively. The gates connected to pins 9 and 10 are shorted together.

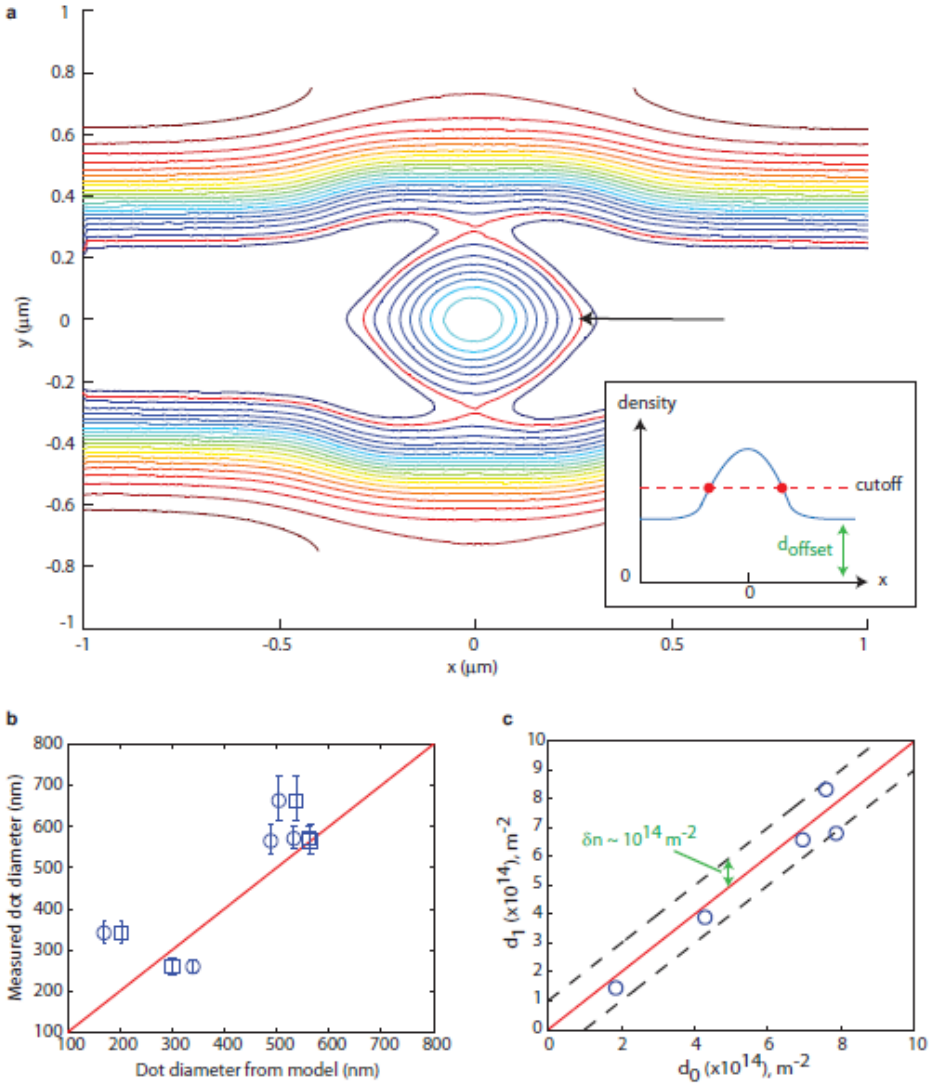

Figure A.7: **(a)** Contour plot representing COMSOL simulation of spatial density profile in device *D4* at a top gate voltage of 12 V. The red line (indicated by the black arrow) is the contour line at the saddle points of the density profile, and the area bounded by the closed portion of this curve represents the quantum dot size calculated by Model 1. *Inset*: Cross sectional cut of density profle along $y = 0$. The points of intersection with the cutoff (red circles) coincide with the red contour line that determines the dot area. **(b)** Simulated dot size versus measured size. Circles and squares represent areas calculated using Models 1 and 2, respectively. Error bars represent the range of diameters expected for measured Coulomb blockade peak spacings within one standard deviation of the mean. **(c)** Comparison between cutoffs in the two modeling approaches. Carrier densities d_0 and d_1 represent the cutoff values above which charge accumulation begins in Models 1 and 2, respectively. The black dashed lines are plots of $y = x \pm \delta n$, where $\delta n \sim 10^{14}\ m^{-2}$ is the density variation due to disorder in our suspended flakes [39].

A.2 Supplementary Figures for Chapter 4

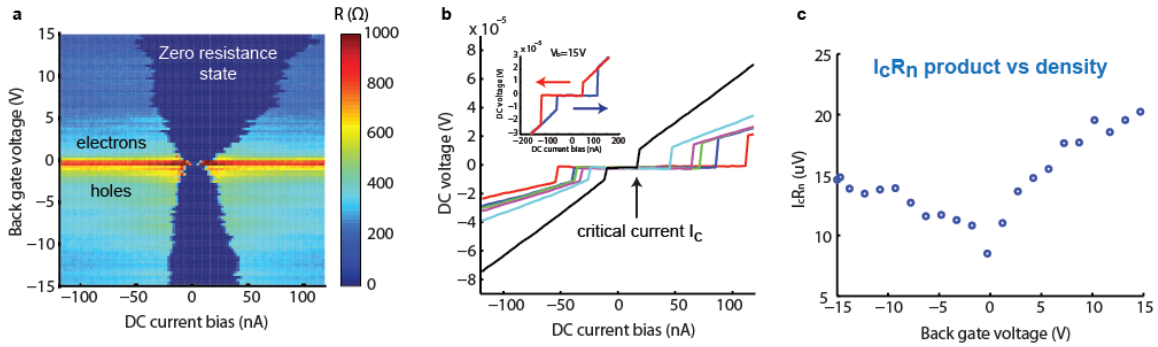

Figure A.8: **(a)** Bipolar supercurrent in graphene, observed in a color map of resistance as a function of DC current bias and back gate voltage. The zero resistance superconducting state is indicated in dark blue, while the normal state resistance is indicated by the colored regions at high bias. **(b)** I-V curves from the data in part (a), plotted for various fixed densities. A DC current bias is applied between the electrodes, and the resulting voltage drop across the junction is recorded. The critical current I_c marks the transition between dissipationless and resistive states. The inset shows typical hysteresis curves based on scan direction of the applied current bias. **(c)** Plot of the I_cR_n product for the data in part (a), where I_c is the critical current and R_n is the normal state resistance. Suppression is observed near the Dirac point, consistent with previous observations in graphene Josephson junctions.

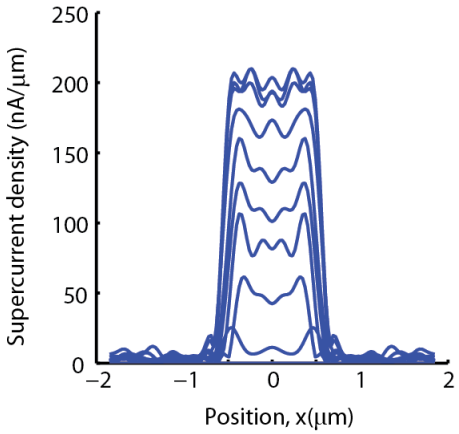

Figure A.9: Supercurrent density distribution as a function of position, for the carrier density range $\sim 0 - 7 \times 10^{11}\ {}_{\rm cm}{}^{-2}$, corresponding to the data in Fig. 4.2d of the main text.

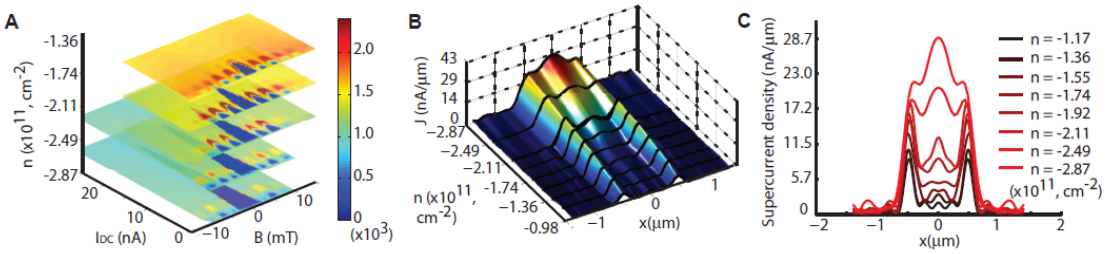

Figure A.10: **(A)** Sequence of Fraunhofer measurements in bilayer device $BL3$ for the current maps in panels (B) and (C), shown in plots of $dV/dI(\Omega)$ as a function of magnetic field B (mT) and current bias I_{DC} (nA). **(B)** Real space image of current flow $J(x)$ as a function of carrier density on the hole side, showing edge currents near the Dirac point and a continuous evolution of bulk flow. **(C)** Individual line cuts of $J(x)$ plotted from (B). This is the data set in Fig. 4.4a of the main text, plotted with a properly scaled vertical axis (supercurrent density, nA/μm).

A.3 Supplementary Figures for Chapter 5

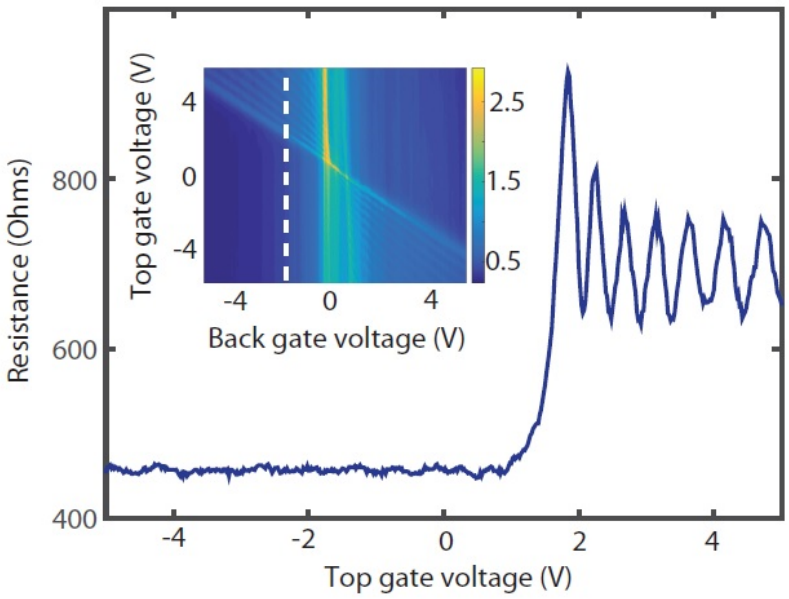

Figure A.11: Normal state resistance of a monolayer graphene device on hBN as a function of top gate when the back gate is held fixed at -1.75 V (resistance line cut corresponds to the white dotted line in the inset). Data was collected from sample *M1*. The oscillation period agrees with a Fabry-Pérot model with a cavity length ~ 100 nm. Inset shows that oscillation occurs in p-n-p and n-p-n regions, which is characteristic of Klein tunneling in monolayer graphene. The oscillations also suggest the ballistic nature of electronic transport in the locally gated region.

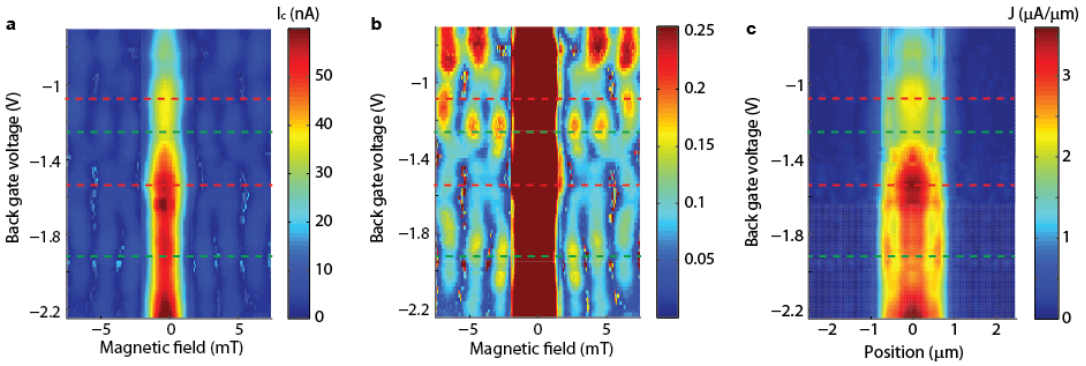

Figure A.12: **(a)** Unsaturated map of the critical current $I_c(B)$ data from Fig. 5.3b, plotted over a full color scale range. **(b)** Plot of normalized critical current $I_c(B)/I_c(B=0)$ from the data in Fig. 5.3b, indicating a nontrivial dependence of Fraunhofer interference on cavity resonances. Red and green dotted lines indicate *on* and *off* resonance conditions for the cavity, respectively. **(c)** Real-space supercurrent density distribution $J(x)$ extracted from the Fraunhofer interference $I_c(B)$ data in Fig. 5.3b using Fourier techniques. (Fig. 5.3c in the main text is a plot of the real-space normalized supercurrent density distribution for this data set.) Data was collected from sample *B2*.

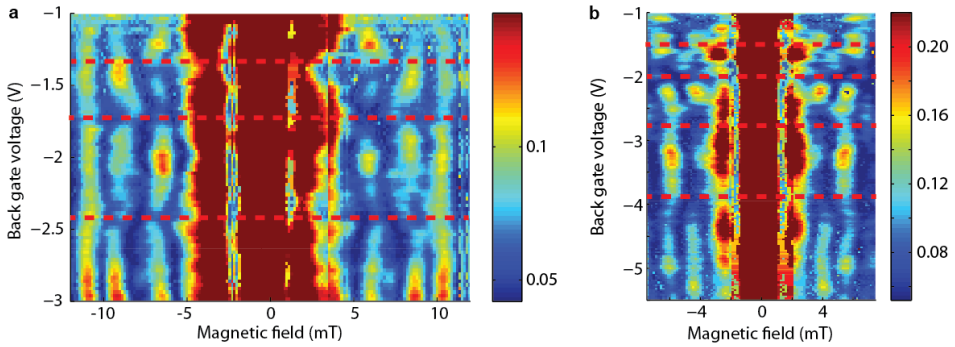

Figure A.13: Plot of normalized critical current $I_c(B)/I_c(B=0)$, indicating nontrivial dependence of Fraunhofer interference on cavity resonances. Red dotted lines indicate *on* resonance conditions for the cavity. Data was collected from samples *B6* (panel **(a)**) and *B7* (panel **(b)**), which exhibit qualitatively similar behavior to sample *B2* in Supplementary Fig. A.12.

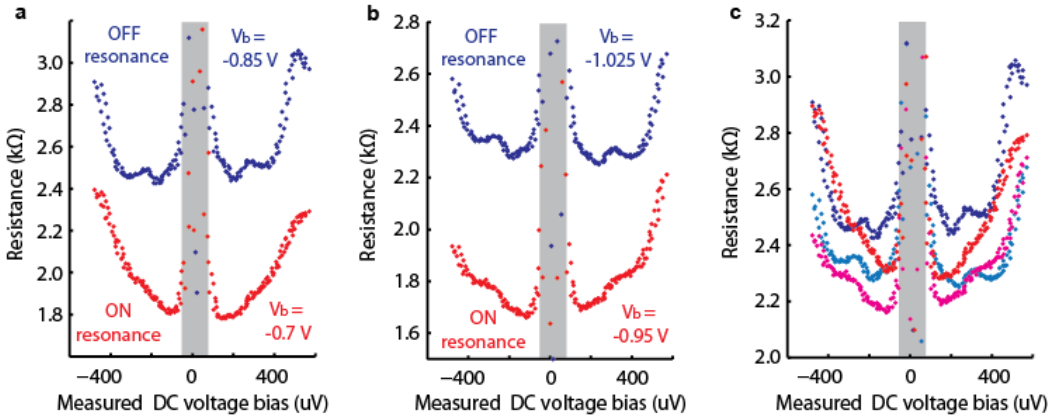

Figure A.14: Experimental resistance profiles obtained using voltage bias spectroscopy, measured at fixed back gate voltages V_b tuned to *on* or *off* resonance conditions for the cavity (red or blue curves, respectively). The amplitude of the multiple Andreev reflections, manifested in resistance dips at $2\Delta/n$ for integer n, is strongly modulated by cavity transmission and thus exhibits suppression when carrier density is tuned on-resonance. **(a)** Red curve: $V_b = -0.7$ V, (on-resonance, corresponding to a dip in normal state resistance). Blue curve: $V_b = -0.85$ V, (off-resonance, corresponding to a peak in normal state resistance). **(b)** Red curve: $V_b = -0.95$ V (on-resonance); Blue curve: $V_b = -1.025$ V (off-resonance). In panels (a) and (b), the red curves are offset by -500Ω for clarity. **(c)** All curves from panels (a) and (b), plotted on the same resistance scale. Red curve: $V_b = -0.7$ V (on-resonance); dark blue curve: $V_b = -0.85$ V (off-resonance); magenta curve: $V_b = -0.95$ V (on-resonance).; light blue curve: $V_b = -1.025$ V (off-resonance). Data was collected from sample *B6*, which shows qualitatively equivalent behavior to sample *B3* in Fig. 5.2e of the main text.

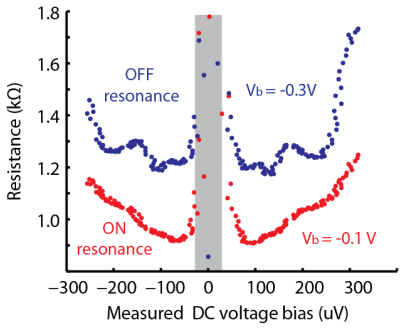

Figure A.15: More voltage bias spectroscopy data from sample in Fig. 5.2e, taken at additional back gate voltages. Red curve: $V_b = -0.1$ V (on-resonance); Blue curve: $V_b = -0.3$ V (off-resonance).

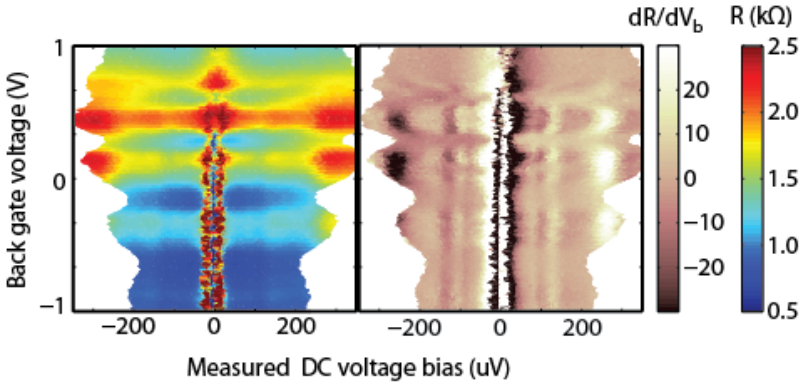

Figure A.16: *Right panel*: A colormap of resistance R_n as a function of applied voltage bias V_{DC} and gate voltage V_b shows modulations due to Fabry-Pérot interference. *Left panel*: Derivative plot dR_n/dV_{DC} for the data on the right. Data sets are from device *B3*.

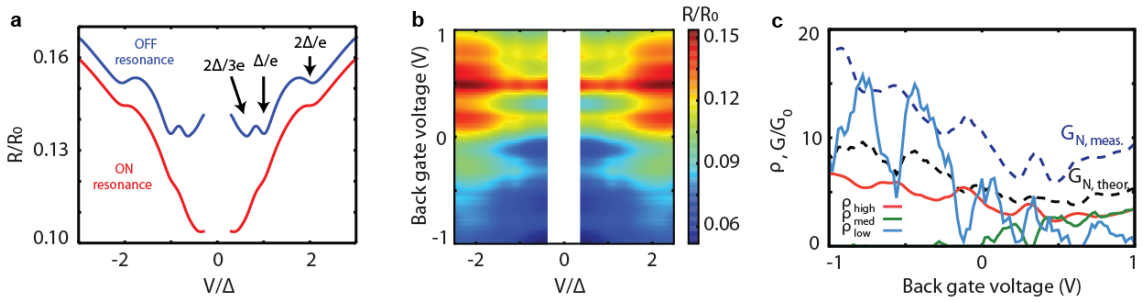

Figure A.17: **(a)** Theoretical resistance profiles as a function of applied bias voltage, corresponding to the experimental data in Fig. 5.2e. The red curve (on resonance, $V_b = 0.3V$) shows suppressed MAR features, while in the blue curve (off resonance, $V_b = 0.5V$) MAR peaks appear at bias voltages 2Δ, Δ, and $2\Delta/3$. The red curve has been shifted upwards by $0.015R_0$ for clarity. **(b)** Simulated resistance map obtained by fitting the measured data to the short junction model, plotted continuously as a function of applied DC bias voltage V and back gate voltage. The theoretical resistance profile is in good agreement with the experimental one (Fig. A.16), showing well defined MAR peaks when the system is off resonance, and suppressed MAR features on resonance. **(c)** Mode contributions ρ (thick solid lines) corresponding to large (red), medium (green), and small (blue) transmissions, as a function of back gate voltage. The black and blue dashed lines show the normal state conductance values from measurement and theory, respectively.

Appendix B

Fabrication of Suspended Graphene Devices

B.1 Fabrication of dual-gated suspended bilayer graphene

Wafer preparation: First sonicate the Si/SiO2 wafer in acetone for 5 minutes and isopropanol for 5 minutes. Acid clean the wafer in H_2SO_4 (96%):H_2O_2(30%):H_2O 4:1:10 at 65 C for 5 minutes, followed by a rinse in water. Do a second acid clean in NH_4OH(29%):H_2O_2(30%):H_2O 3:1:10 at 65 C for 5 minutes, followed by a rinse in water. Then ozone clean the substrate at 60C for 30 minutes, bake it at 250 C for 30 minutes, bake it at 160 C for 10 minutes, and then deposit graphene (we use standard green-label Scotch tape for exfoliation). I used highly ordered pyrolytic graphite (HOPG) ordered from SPI supplies, product number 430HP-AB (HOPG GD ZYA, 12x12x2 mm).

Lithography for electrical contacts, gate dielectric, and top gates: To prepare the e-beam resist, spin on 495 PMMA C6 (from Microchem) at 4000 rpm, 40 seconds. Bake at 180 C for 6 minutes. Then spin on 950 PMMA A4 at 4000 rpm, 40

seconds. Bake at 180 C for 5 minutes. After the lithography, develop in MIBK/IPA 1:3 developer for 4 minutes, 30 seconds, followed by a rinse in isopropanol. Scratch the corner of the chip to make electrical contact to the back gate. Ozonate the chip at 60 C for 1 minute. Evaporate the metal for the contacts in the cleanroom thermal evaporator. First pump down the chamber to pressures in the low to mid 10^{-7} Torr range. Evaporate 3 nm of chromium at a rate of 0.1 A/s, followed by 100 nm of gold at a rate of 1.5 A/s. Do liftoff in acetone at 80 C. For the top gate dielectric, use the same lithography procedure as for the contacts. Deposit about 280 nm of SiO2 using e-beam evaporation in the Edwards EE-2 evaporator at a rate of 1.5 A/s. To define the top gates, use the same lithography procedure as for the contacts. Thermally evaporate 3 nm of chromium at a rate of 0.1 A/s, followed by 300 nm of gold at a rate of 1.5 A/s. [Note: for local suspended top gates, define the smallest features as follows. Spin on 950 PMMA A4 at 4000 rpm, 40 seconds and bake at 180 C for 10 minutes. Evaporate 3 nm of chromium at a rate of 0.1 A/s, followed by 75 nm of gold at a rate of 1 A/s. The rest of the process is identical to that for globally gated devices.] Finally, etch in 5:1 buffered oxide etch (BOE) for 1 minute, 30 seconds, followed by a rinse in two beakers of methanol. Dry in the critical point dryer CD-1.

B.2 Current annealing procedure for graphene

Connect device contacts to the parameter analyzer using BNC cables, connecting the source and drain contacts to terminals 2 and 3 on the parameter analyzer, respectively. When current annealing, use the following settings on the parameter analyzer: SMU1 - V - CONST; SMU2 - V - VAR1; SMU3 - Common - CONST. Set the compliance of VAR1 (SMU2) to 10 mA (sets an upper bound on current through the sample; we stay well below this during current annealing). Make sure the "double" setting is selected to ensure the

bias automatically ramps to zero volts after the scan. To current anneal, sweep the DC voltage bias from zero to two volts at the "medium" rate setting (and allow the voltage to automatically ramp to zero). To assess samples changes due to annealing, measure flake resistance as a function of back gate voltage at zero DC bias. To do this, use the following settings on the parameter analyzer: SMU1 - V - VAR1; SMU2 - V - VAR2; SMU3 - Common - CONST. Ramp the back gate (SMU1) from 0 to 15 V with a step size of 20 mV and a compliance of 10 nA. Set the source-drain bias (SMU2) to 200 uV. Define R2=V2/I2 and display V1, R2, and I1. I use the same procedure for both two terminal and multi-terminal graphene devices.

Appendix C

Preparation of graphene - boron nitride layered heterostructures

C.1 Piranha cleaning recipe for wafers

For graphene-boron nitride heterostructures, I used Nova Si/SiO2 wafers (Description: 6" P/Bo < 100 > 0.001-0.004 ohm-cm; 500±18 μm Thick SSP Prime Grade Si wafers w/ Primary Flat only, 2850 A Dry Chlorinated), which are stored in the wafer cabinet on the 6th floor. To clean the wafers, prepare an acid mixture of H_2SO_4:H_2O_2 at a ratio of 3:1 in a glass beaker. Place the wafers in the piranha solution and soak for 30 minutes at 80 C on the hot plate. Immediately remove the wafers from the solution and place them in a beaker of water to rinse. Then soak them in a second beaker of clean water for a few minutes (about 5 minutes). Blow dry with the nitrogen gas gun. Exfoliate all graphene and hBN flakes directly onto the piranha-cleaned Si/SiO2 wafers using room-temperature exfoliation with the blue tape (gently rub plastic tweezers over the tape for about 2-3 minutes to deposit flakes).

C.2 Flake pick-up procedure for assembly of van der Waals heterostructures

PPC preparation: To pick up flakes, we used a polymer consisting of 15 wt% Alfa Aesar polypropelyne carbonate (PPC) in anisole. Specifically, use 3 grams of PPC in 20 mL anisole. Place this in a brown glass bottle with a small magnetic stir rod and leave it on the hot plate at 90 C overnight with the stirrer on to allow the polymer to dissolve.

Preparation of glass slide/polymer stack: Prepare roughly a 1 mm thick PDMS layer in a plastic petri dish (or buy it commercially). The full stack consists of a glass microscope slide/ PDMS square/transparent tape/PPC. First place a square of PDMS (about 2 mm in size) onto a glass microscope slide and cover with transparent Scotch tape. For the top layer, spin PPC at 3000 rpm for 1 minute onto a Si wafer and bake at 90 C for 5 minutes. Cut a window larger than the size of the PDMS square into a piece of Scotch tape (green label) and secure the tape on the PPC. Peel the PPC off the Si wafer with the tape (scratching corner with tweezers to get it started, if necessary), align the window over the PDMS, and tape it in place over the PDMS.

Flake pick-up and transfer: Align the square polymer stack over the desired pickup flake on the Si/SiO2 wafer. Lower the stack with the z-micrometer to bring the PPC into contact with the flake at room temperature. Heat to 45 C. Good contact should be achieved, as indicated by a large green region extending around the target flake. Cool to 30 C, then disengage stack. Pickup is successful if flake appears transparent on the PPC stack. To transfer the pick-up flake onto a target flake, align the stack over the target flake on the Si/SiO2 wafer and bring into contact at room temperature. Heat to 80 C. Disengage using the z-micromanipulator. Green regions indicate where the polymer has adhered to the chip and purple regions indicate where the polymer remains on the PDMS stack. To

remove the PPC deposited on the wafer, immerse chip in chloroform for 15 minutes. Rinse in IPA and blow dry with nitrogen gas.

C.3 Exfoliation of MoS_2

Sonicate Si/SiO2 wafers in acteone for 5 minutes and isopropanol for 5 minutes. Then clean the wafers using an oxygen reactive ion etch: use the recipe "Joel-WangO2cleaning of substrate" on the RIE-8 tool in the cleanroom. Exfoliate the MoS_2 using Scotch tape, heat the chip on a hot plate at 160 C, and press the tape onto the chip for roughly 1 minute, 30s to deposit MoS_2.

Bibliography

[1] M. I. Katsnelson, K. S. Novoselov, and A. K. Geim. Chiral tunneling and the Klein paradox in graphene. *Nat. Phys.*, 2:620–625, 2006.

[2] A. H. CastroNeto, F. Guinea, N. M. R. Peres, K. S. Novoselov, and A. K. Geim. The electronic properties of graphene. *Rev. Mod. Phys.*, 81:109–162, 2009.

[3] E. McCann. Asymmetry gap in the electronic band structure of bilayer graphene. *Phys. Rev. B*, 74:161403, 2006.

[4] E. V. Castro, K. S. Novoselov, S. V. Morozov, N. M. R. Peres, J. M. B. Lopes dos Santos, J. Nilsson, F. Guinea, A. K. Geim, and A. H. Castro Neto. Biased bilayer graphene: Semiconductor with a gap tunable by the electric field effect. *Phys. Rev. Lett.*, 99(21):216802, 2007.

[5] H. K. Min, B. Sahu, S. K. Banerjee, and A. H. MacDonald. Ab initio theory of gate induced gaps in graphene bilayers. *Phys. Rev. B*, 75:155115, 2007.

[6] J. B. Oostinga, H. B. Heerche, X. Liu, A. F. Morpurgo, and L. M. K. Vandersypen. Gate-induced insulating state in bilayer graphene devices. *Nature Materials*, 7:151–157, 2007.

[7] Y. Zhang, T. Tang, C. Girit, Z. Hao, M. C. Martin, A. Zettl, M. F. Crommie, Y. R. Shen, and F. Wang. Direct observation of a widely tunable bandgap in bilayer graphene. *Nature*, 459:820–823, 2009.

[8] Y. B. Zhang, Y. W. Tan, H. L. Stormer, and P. Kim. Experimental observation of the quantum hall effect and berry's phase in graphene. *Nature*, 438:201–204, 2005.

[9] K. S. Novoselov, E. McCann, S. V. Morozov, V. I. Falko, M. I. Katsnelson, U. Zeitler, D. Jiang, F. Schedin, and A. K. Geim. Unconventional quantum Hall effect and Berry's phase of 2π in bilayer graphene. *Nat. Phys.*, 2:177–180, 2006.

[10] A. K. Geim and K. S. Novoselov. The rise of graphene. *Nat. Mater.*, 6:183, 2007.

[11] E. McCann and V. I. Fal'ko. Landau-level degeneracy and quantum Hall effect in a graphite bilayer. *Phys. Rev. Lett.*, 96:086805, 2006.

[12] K. Yang, K. Moon, L. Zheng, A. H. MacDonald, S. M. Girvin, D. Yoshioka, and S.-C. Zhang. Quantum ferromagnetism and phase transitions in double–layer quantum hall systems. *Phys. Rev. Lett.*, 72:732, 1994.

[13] M. Ezawa. Intrinsic zeeman effect in graphene. *J. Phys. Soc. Jpn.*, 76:094701, 2007.

[14] Y. Barlas, R. Cote, K. Nomura, and A. H. MacDonald. Intra-landau-level cyclotron resonance in bilayer graphene. *Phys. Rev. Lett.*, 101:097601, 2008.

[15] B. E. Feldman, J. Martin, and A. Yacoby. Broken symmetry states and divergent resistance in suspended bilayer graphene. *Nature Physics*, 5:889–893, 2009.

[16] Y. Zhao, P. Cadden-Zimansky, Z. Jiang, and P. Kim. Symmetry breaking in the zero-energy Landau level in bilayer graphene. *Phys. Rev. Lett.*, 104(6):066801, 2010.

[17] W. Bao, Z. Zhao, H. Zhang, G. Liu, P. Kratz, L. Jing, J. Velasco, D. Smirnov, and C. N. Lau. Magnetoconductance oscillations and evidence for fractional quantum hall states in suspended bilayer and trilayer graphene. *Phys. Rev. Lett.*, 105:246601, 2010.

[18] J. Martin, B. E. Feldman, R. T. Weitz, M. T. Allen, and A. Yacoby. Local compressibility measurements of correlated states in suspended bilayer graphene. *Phys. Rev. Lett.*, 105(25):256806, 2010.

[19] C. R. Dean, A. F. Young, I. Meric, C. Lee, L. Wang, S. Sorgenfrei, K. Watanabe, T. Taniguchi, P. Kim, K. L. Shepard, and J. Hone. Boron nitride substrates for high-quality graphene electronics. *Nat. Nanotech.*, 5:722, 2010.

[20] C. W. J. Beenakker. Andreev reflection and Klein tunneling in graphene. *Rev. Mod. Phys.*, 80:1337–1354, 2008.

[21] H. B. Heersche, P. Jarillo-Herrero, J. B. Oostinga, L. M. K. Vandersypen, and A. F. Morpurgo. Bipolar supercurrent in graphene. *Nature*, 446:56–59, 2007.

[22] X. Du, I. Skachko, and E. Y. Andrei. Josephson current and multiple andreev reflections in graphene sns junctions. *Phys. Rev. B*, 77:184507, 2008.

[23] M. Tinkham. *Introduction to Superconductivity.* McGraw-Hill Book Co., New York, NY, 1975.

[24] R. C. Dynes and T. A. Fulton. Supercurrent density distribution in Josephson junctions. *Phys. Rev. B*, 3:3015, 1971.

[25] F. D. M. Haldane. Model for a quantum hall effect without landau levels: Condensed-matter realization of the "parity anomaly". *Phys. Rev. Lett.*, 61:2015, 1988.

[26] S. Raghu, X.-L. Qi, C. Honerkamp, and S.-C. Zhang. Topological mott insulators. *Phys. Rev. Lett.*, 100:156401, 2008.

[27] H. Min, G. Borghi, M. Polini, and A. H. MacDonald. Pseudospin magnetism in graphene. *Phys. Rev. B*, 77:041407, 2008.

[28] R. Nandkishore and L. Levitov. Dynamical screening and excitonic instability in bilayer graphene. *Phys. Rev. Lett.*, 104:156803, 2010.

[29] R. Nandkishore and L. Levitov. Flavor symmetry and competing orders in bilayer graphene, Preprint at.

[30] F. Zhang, H. Min, and M. Poliniand A. H. MacDonald. Spontaneous inversion symmetry breaking in graphene bilayers. *Phys. Rev. B*, 81:041402, 2010.

[31] O. Vafek and K. Yang. Many–body instability of coulomb interacting bilayer graphene: Renormalization group approach. *Phys. Rev. B*, 81:041401, 2010.

[32] Y. Lemonik, I. L. Aleiner, C. Toke, and V. I. Falko. Spontaneous symmetry breaking and lifshitz transition in bilayer graphene. *Phys. Rev. B*, 82:201408(R), 2010.

[33] J. Moser, A. Barreiro, and A. Bachtold. Current–induced cleaning of graphene. *Appl. Phys. Lett.*, 91:163513, 2007.

[34] K. I. Bolotin, K. J. Sikes, Z. Jiang, M. Klima, G. Fudenberg, J. Hone, P. Kim, and H. L. Stormer. Ultrahigh electron mobility in suspended graphene. *Solid State Commun.*, 146:351, 2008.

[35] A. B. Kuzmenko, E. van Heumen, D. van der Marel, P. Lerch, P. Blake, K. S. Novoselov, and A. K. Geim. Infrared spectroscopy of electronic bands in bilayer graphene. *Phys. Rev. B*, 79:115441, 2009.

[36] J. Shan T. F. Heinz K. F. Mak, C. H. Lui. Observation of an electric-field-induced band gap in bilayer graphene by infrared spectroscopy. *Phys. Rev. Lett.*, 102:256405, 2009.

[37] Y. P. Shkolnikov, E. P. De Poortere, E. Tutuc, and M. Shayegan. Valley splitting of alas two-dimensional electrons in a perpendicular magnetic field. *Phys. Rev. Lett.*, 89:226805, 2002.

[38] D. A. Abanin, K. S. Novoselov, U. Zeitler, P. A. Lee, A. K. Geim, and L. S. Levitov. Dissipative quantum hall effect in graphene near the dirac point. *Phys. Rev. Lett.*, 98:196806, 2007.

[39] E. Shimshoni, H. A. Fertig, and G. V. Pai. Onset of an insulating zero-plateau quantum hall state in graphene. *Phys. Rev. Lett.*, 102:206408, 2009.

[40] E. V. Gorbar, V. P. Gusynin, and V. A. Miransky. Dynamics and phase diagram of the $\nu = 0$ quantum hall state in bilayer graphene. *Phys. Rev. B*, 81:155451, 2010.

[41] I. Meric, M. Y. Han, A. F. Young, B. Ozyilmaz, P. Kim, and K. L. Shepard. Current saturation in zero-bandgap, top-gated graphene field-effect transistors. *Nature Nanotechnology*, 3:654–659, 2008.

[42] C. Stampfer, J. Guttinger, F. Molitor, D. Graf, T. Ihn, and K. Ensslin. Tunable Coulomb blockade in nanostructured graphene. *Appl. Phys. Lett.*, 92(1):012102, 2008.

[43] B. Trauzettel, D. V. Bulaev, D. Loss, and G. Burkard. Spin qubits in graphene quantum dots. *Nature Physics*, 3:192–196, 2007.

[44] A. V. Khaetskii, D. Loss, and L. Glazman. Electron spin decoherence in quantum dots due to interaction with nuclei. *Phys. Rev. Lett.*, 88:186802, 2002.

[45] J. R. Petta, A. C. Johnson, J. M. Taylor, E. A. Laird, A. Yacoby, M. D. Lukin, C. M. Marcus, M. P. Hanson, and A. C. Gossard. Coherent manipulation of coupled electron spins in semiconductor quantum dots. *Science*, 309(5744):2180–2184, 2005.

[46] F. H. L. Koppens, C. Buizert, K. J. Tielrooij, I. T. Vink, K. C. Nowack, T. Meunier, L. P. Kouwenhoven, and L. M. K. Vandersypen. Driven coherent oscillations of a single electron spin in a quantum dot. *Nature*, 442:766–771, 2006.

[47] P. Recher, J. Nilsson, G. Burkard, and B. Trauzettel. Bound states and magnetic field induced valley splitting in gate-tunable graphene quantum dots. *Phys. Rev. B*, 79:085407, 2009.

[48] Y. Wu, V. Perebeinos, Y. Lin, T. Low, F. Xia, and P. Avouris. Quantum behavior of graphene transistors near the scaling limit. *Nano Lett.*, 12(3):1417–1423, 2012.

[49] H. Y. Hui, A. M. Lobos, J. D. Sau, and S. Das Sarma. Proximity-induced superconductivity and Josephson critical current in quantum spin Hall systems. 2014.

[50] K. Todd, H. Chou, S. Amasha, and D. Goldhaber-Gordon. Quantum dot behavior in graphene nanoconstrictions. *Nano Lett.*, 9(1):416–421, 2008.

[51] J. Martin, N. Akerman, G. Ulbricht, T. Lohmann, J. H. Smet, K. von Klitzing, and A. Yacoby. Observation of electron-hole puddles in graphene using a scanning single-electron transistor. *Nat. Phys.*, 4:144–148, 2008.

[52] F. Molitor, S. Droscher, J. Guttinger, A. Jacobsen, C. Stampfer, T. Ihn, and K. Ensslin. Transport through graphene double dots. *Appl. Phys. Lett.*, 94(22):222107, 2009.

[53] X. L. Liu, D. Hug, and L. M. K. Vandersypen. Gate-defined graphene double quantum dot and excited state spectroscopy. *Nano. Lett.*, 10(5):1623–1627, 2010.

[54] X. Wang, Y. Ouyang, L. Jiao, H. Wang, L. Xie, J. Wu, J. Guo, and H. Dai. Graphene nanoribbons with smooth edges behave as quantum wires. *Nature Nanotechnology*, 6:563–567, 2011.

[55] J. M. Pereira, P. Vasilopoulos, and F. M. Peeters. Tunable quantum dots in bilayer graphene. *Nano Lett.*, 7:946–949, 2007.

[56] E. McCann. Asymmetry gap in the electronic band structure of bilayer graphene. *Phys. Rev. B*, 74(16):161403, 2006.

[57] F. Xia, D. B. Farmer, Y. Lin, and P. Avouris. Graphene field-effect transistors with high on/off current ratio and large transport band gap at room temperature. *Nano. Lett.*, 10(2):715–718, 2010.

[58] T. Taychatanapat and P. Jarillo-Herrero. Electronic transport in dual-gated bilayer graphene at large displacement fields. *Phys. Rev. Lett*, 105:166601, 2010.

[59] K. Nomura and A. H. MacDonald. Quantum Hall ferromagnetism in graphene. *Phys. Rev. Lett.*, 96(25):256602, 2006.

[60] R. T. Weitz, M. T. Allen, B. E. Feldman, J. Martin, and A. Yacoby. Broken-symmetry states in doubly gated suspended bilayer graphene. *Science*, 330(6005):812–816, 2010.

[61] I. Martin, Y. M. Morpurgo, and A. F. Morpurgo. Topological confinement in bilayer graphene. *Phys. Rev. Lett.*, 100:036804, 2008.

[62] D. B. Chklovskii, B. I. Shklovskii, and L. I. Glazman. Electrostatics of edge channels. *Phys. Rev. B*, 46(7):4026–4034, 1992.

[63] R. Leturcq, C. Stampfer, K. Inderbitzin, L. Durrer, C. Hierold, E. Mariani, M. G. Schultz, F. von Oppen, and K. Ensslin. Franck Condon blockade in suspended carbon nanotube quantum dots. *Nature Physics*, 5:327–331, 2009.

[64] G. A. Steele, A. K. Huttel, B. Witkamp, M. Poot, H. B. Meerwaldt, L. P. Kouwenhoven, and H. S. J. van der Zant. Strong coupling between single-electron tunneling and nanomechanical motion. *Science*, 325(5955):1103–1107, 2009.

[65] A. V. Shytov, L. S. Levitov, and C. W. J. Beenakker. Electromechanical noise in a diffusive conductor. *Phys. Rev. Lett.*, 88:228303, 2002.

[66] M. D. LaHaye, O. Buu, B. Camarota, and K. C. Schwab. Approaching the quantum limit of a nanomechanical resonator. *Science*, 304(5667):74–77, 2004.

[67] J. S. Bunch, A. M. van der Zande, S. S. Verbridge, I. W. Frank, D. M. Tanenbaum, J. M. Parpia, H. G. Craighead, and P. L. McEuen. Electromechanical resonators from graphene sheets. *Science*, 315(5811):490–493, 2007.

[68] C. Chen, S. Rosenblatt, K. I. Bolotin, W. Kalb, P. Kim, I. Kymissis, H. L. Stormer, T. F. Heinz, and J. Hone. Performance of monolayer graphene nanomechanical resonators with electrical readout. *Nature Nanotechnology*, 4:861–867, 2009.

[69] A. H. Castro Neto, F. Guinea, N. M. R. Peres, K. S. Novoselov, and A. K. Geim. The electronic properties of graphene. *Rev. Mod. Phys.*, 81:109–162, 2009.

[70] M. I. Katsnelson, K. S. Novoselov, and A. K. Geim. Chiral tunnelling and the klein paradox in graphene. *Nat. Phys.*, 2:620–625, 2006.

[71] A. F. Young and P. Kim. Quantum interference and Klein tunnelling in graphene heterojunctions. *Nat. Phys.*, 5:222–226, 2009.

[72] L.C. Campos, A.F. Young, K. Surakitbovorn, K. Watanabe, T. Taniguchi, and P. Jarillo-Herrero. Quantum and classical confinement of resonant states in a trilayer graphene Fabry-Perot interferometer. *Nat. Commun.*, 3:1239, 2012.

[73] A. Varlet, M.-H. Liu, V. Krueckl, D. Bischoff, P. Simonet, K. Watanabe, T. Taniguchi, K. Richter, K. Ensslin, and T. Ihn. Fabry-Pérot interference in gapped bilayer graphene with broken anti-Klein tunneling. *Phys. Rev. Lett.*, 113:116601, 2014.

[74] V. V. Cheianov, V. Fal'ko, and B. L. Altshuler. The focusing of electron flow and a Veselago lens in graphene p-n junctions. *Science*, 315(5816):1252–1255, 2007.

[75] A. V. Shytov, M. S. Rudner, and L. S. Levitov. Klein backscattering and Fabry-Perot interference in graphene heterojunctions. *Phys. Rev. Lett.*, 101:156804, 2008.

[76] A. S. Mayorov, R. V. Gorbachev, S. V. Morozov, L. Britnell, R. Jalil, L. A. Ponomarenko, P. Blake, K. S. Novoselov, K. Watanabe, T. Taniguchi, and A. K. Geim. Micrometer-scale ballistic transport in encapsulated graphene at room temperature. *Nano Lett.*, 11:2396–2399, 2011.

[77] J. M. Pereira, V. Mlinar, F. M. Peeters, and P. Vasilopoulos. Confined states and direction-dependent transmission in graphene quantum wells. *Phys. Rev. B*, 74:045424, 2006.

[78] F.-M. Zhang, Y. He, and X. Chen. Guided modes in graphene waveguides. *Applied Physics Letters*, 94(21), 2009.

[79] R. R. Hartmann, N. J. Robinson, and M. E. Portnoi. Smooth electron waveguides in graphene. *Phys. Rev. B*, 81:245431, 2010.

[80] J. R. Williams, T. Low, M. S. Lundstrom, and C. M. Marcus. Gate-controlled guiding of electrons in graphene. *Nat. Nanotech.*, 6:222–225, 2011.

[81] T. Taychatanapat, K. Watanabe, T. Taniguchi, and P Jarillo-Herrero. Electrically tunable transverse magnetic focusing in graphene. *Nat. Phys.*, 9:225–229, 2013.

[82] K. A. Ritter and J. W. Lyding. The influence of edge structure on the electronic properties of graphene quantum dots and nanoribbons. *Nat. Mater.*, 8:235–242, 2009.

[83] C. Tao, L. Jiao, O. V. Yazyev, Y. C. Chen, J. Feng, X. Zhang, R. B. Capaz, J. M. Tour, S. G. Louie, H. Dai, and M. F. Crommie. Spatially resolving edge states of chiral graphene nanoribbons. *Nat. Phys.*, 7:616–620, 2011.

[84] J. B. Oostinga, H. B. Heersche, X. Liu, A. F. Morpurgo, and L. M. K. Vandersypen. Gate-induced insulating state in bilayer graphene devices. *Nat. Mater.*, 7:151–157, 2007.

[85] D. Bischoff, F. Libisch, J. Burgdrfer, T. Ihn, and K. Ensslin. Characterizing wave functions in graphene nanodevices: Electronic transport through ultrashort graphene constrictions on a boron nitride substrate. *Phys. Rev. B*, 90:115405, 2014.

[86] A. Barone and G. Paterno. *Physics and Applications of the Josephson Effect*. John Wiley and Sons Inc., 1982.

[87] C. R. Dean, A. F. Young, I. Meric, C. Lee, L. Wang, S. Sorgenfrei, K. Watanabe, T. Taniguchi, P. Kim, K. L. Shepard, and J. Hone. Boron nitride substrates for high-quality graphene electronics. *Nat. Nanotech.*, 5:722–726, 2010.

[88] J. C. Cuevas and F. S. Bergeret. Magnetic interference patterns and vortices in diffusive SNS junctions. *Phys. Rev. Lett.*, 99:217002, 2007.

[89] R. C. Jaklevic, J. Lambe, and J. E. Mercereau. Quantum interference effects in Josephson tunneling. *Phys. Rev. Lett.*, 12:159, 1964.

[90] E. V. Castro, K. S. Novoselov, S. V. Morozov, N. M. R. Peres, J. M. B Lopes dos Santos, J. Nilsson, F. Guinea, A. K. Geim, and A. H. Castro Neto. Biased bilayer graphene: Semiconductor with a gap tunable by the electric field effect. *Phys. Rev. Lett.*, 99:216802, 2007.

[91] R. Jackiw and C. Rebbi. Solitons with fermion number . *Phys. Rev. D*, 13:3398–3409, 1976.

[92] P. G. Silvestrov and K. B. Efetov. Charge accumulation at the boundaries of a graphene strip induced by a gate voltage: Electrostatic approach. *Phys. Rev. B*, 77:155436, 2008.

[93] K. Nakada, M. Fujita, G. Dresselhaus, and M. S. Dresselhaus. Edge state in graphene ribbons: Nanometer size effect and edge shape dependence. *Phys. Rev. B*, 54:17954, 1996.

[94] A. R. Akhmerov and C. W. J. Beenakker. Boundary conditions for Dirac fermions on a terminated honeycomb lattice. *Phys. Rev. B*, 77:085423, 2008.

[95] E. V. Castro, N. M. R. Peres, J. M. B Lopes dos Santos, A. H. Castro Neto, and F. Guinea. Localized states at zigzag edges of bilayer graphene. *Phys. Rev. Lett.*, 100:026802, 2008.

[96] M. T. Allen, O. Shtanko, I. C. Fulga, J. I.-J. Wang, D. Nurgaliev, K. Watanabe, T. Taniguchi, A. R. Akhmerov, P. Jarillo-Herrero, L. S. Levitov, and A. Yacoby. Visualization of phase-coherent electron interference in a ballistic graphene josephson junction. 2015.

[97] D. Xiao, W. Yao, and Q. Niu. Valley-contrasting physics in graphene: Magnetic moment and topological transport. *Phys. Rev. Lett.*, 99:236809, 2007.

[98] J. Jung, F. Zhang, Z. Qiao, and A. H. MacDonald. Valley-hall kink and edge states in multilayer graphene. *Phys. Rev. B*, 84:075418, 2011.

[99] F. Zhang, A. H. MacDonald, and E. J. Mele. Valley Chern numbers and boundary modes in gapped bilayer graphene. *PNAS*, 110:10546–10551, 2013.

[100] J. S. Alden, A. W. Tsen, P. Y. Huang, R. Hovden, L. Brown, J. Park, D. A. Muller, and P. L. McEuen. Strain solitons and topological defects in bilayer graphene. *PNAS*, 110:11256–11260, 2013.

[101] A. Patil, D. Huard, and C. J. Fonnesbeck. Pymc: Bayesian stochastic modelling in python. *Journal of Statistical Software*, 35(4):1–81, 7 2010.

[102] A. Spisser, R. Ledantec, C. Seassal, J.L. Leclercq, T. Benyattou, D. Rondi, R. Blondeau, G. Guillot, and P. Viktorovitch. Highly selective and widely tunable 1.55 um InP/air-gap micromachined Fabry-Perot filter for optical communications. *Photonics Technology Letters, IEEE*, 10(9):1259–1261, Sept 1998.

[103] T. J. Balle and W. H. Flygare. FabryPerot cavity pulsed Fourier transform microwave spectrometer with a pulsed nozzle particle source. *Review of Scientific Instruments*, 52(1):33–45, 1981.

[104] A. Abramovici, W. E. Althouse, R. W. P. Drever, Y. Gursel, S. Kawamura, F. J. Raab, D. Shoemaker, L. Sievers, R. E. Spero, K. S. Thorne, R. E. Vogt, R. Weiss, S. E. Whitcomb, and M. E. Zucker. LIGO: The laser interferometer gravitational-wave observatory. *Science*, 256(5055):325–333, 1992.

[105] J. R. Williams, T. Low, M. S. Lundstrom, and C. M. Marcus. Gate-controlled guiding of electrons in graphene. *Nat. Nanotech.*, 6:222–225, 2011.

[106] Y. Zhao, J. Wyrick, F. D. Natterer, J. F. Rodriguez-Nieva, C. Lewandowski, K. Watanabe, T. Taniguchi, L. S. Levitov, N. B. Zhitenev, and J. A. Stroscio. Creating and probing electron whispering-gallery modes in graphene. *Science*, 348(6235):672–675, 2015.

[107] N. Gu, M. Rudner, and L. Levitov. Chirality-assisted electronic cloaking of confined states in bilayer graphene. *Phys. Rev. Lett.*, 107:156603, 2011.

[108] W. Liang, M. Bockrath, D. Bozovic, J. Hafner, M. Tinkham, and H. Park. Fabry-perot interference in a nanotube electron waveguide. *Nature*, 411:665–669, 2001.

[109] M. T. Allen, O. Shtanko, I. C. Fulga, A. Akhmerov, K. Watanabi, T. Taniguchi, P. Jarillo-Herrero, L. S. Levitov, and A. Yacoby. Spatially resolved edge currents and guided-wave electronic states in graphene. *Nature Physics*, 12:128–133, 2016.

[110] T. Nishio, T. Kozakai, S. Amaha, M. Larsson, H. A. Milsson, H. Q. Xu, G. Zhang, K. Tateno, H. Takayanagi, and K. Ishibashi. Supercurrent through inas nanowires with highly transparent superconducting contacts. *Nanotechnology*, 22:445701, 2011.

[111] H. I. Jorgensen, K. Grove-Rasmussen, T. Novotny, K. Flensberg, and P. E. Lindelof. Electron transport in single-wall carbon nanotube weak links in the fabry-perot regime. *Phys. Rev. Lett.*, 96:207003, 2006.

[112] V. E. Calado, S. Goswami, G. Nanda, M. Diez, A. R. Akhmerov, K. Watanabe, T. Taniguchi, T. M. Klapwijk, and L. M. K. Vandersypen. Ballistic josephson junctions in edge-contacted graphene. 2015.

[113] M. Ben Shalom, M. J. Zhu, V. I. Fal'ko, A. Mishchenko, A. V. Kretinin, K. S. Novoselov, C. R. Woods, K. Watanabe, T. Taniguchi, A. K. Geim, and J. R. Prance. Proximity superconductivity in ballistic graphene, from fabry-perot oscillations to random andreev states in magnetic field. 2015.

[114] P. Blake, R. Yang, S. V. Morozov, F. Schedin, L. A. Ponomarenko, A. A. Zhukov, R. R. Nair, I. V. Grigorieva, K. S. Novoselov, and A. K. Geim. Influence of metal contacts and charge inhomogeneity on transport properties of graphene near the neutrality point. *Solid State Comm.*, 149:1068–1071, 2009.

[115] A. F. Young and P. Kim. Quantum interference and klein tunneling graphene heterojunctions. *Nat. Phys.*, 5:222–226, 2009.

[116] A. L. Grushina, D. Ki, and A. Morpurgo. A ballistic pn junction in suspended graphene with split bottom gates. *App. Phys. Lett.*, 102:223102, 2013.

[117] P. Rickhaus, R. Maurand, M. Liu, M. Weiss, K. Richter, and C. Schonenberger. Ballistic interferences in suspended graphene. 2013.

[118] M. T. Allen, J. Martin, and A. Yacoby. Gate-defined quantum confinement in suspended bilayer graphene. *Nat. Commun.*, 3:934, 2012.

[119] G. E. Rittenhouse and J. M. Graybeal. Fabry-perot interference peaks in the critical current for ballistic superconductor-normal-metal-superconductor Josephson junctions. *Phys. Rev. B*, 49:1182–1187, 1994.

[120] D. Averin and A. Bardas. Ac josephson effect in a single quantum channel. *Phys. Rev. Lett.*, 75:1831–1834, 1995.

[121] P. Jarillo-Herrero, J. A. van Dam, and L. P. Kouwenhoven. Quantum supercurrent transistors in carbon nanotubes. *Nature*, 439:953–956, 2006.

[122] I. O. Kulik. Macroscopic quantization and the proximity eddect in sns junctions. *Sov.Phys. JETP*, 30(5):944, 1970.

[123] A. V. Svidzinskii. *Spatially Inhomogeneous Problems in the Theory of Superconductivity.* Nauka, Moscow, 1982.

[124] V. Barzykin and A. M. Zagoskin. Coherent transport and nonlocality in mesoscopic sns junctions: anomalous magnetic interference patterns. *Superlattices and microstructures*, 25(5):797–807, 1999.

[125] U. Ledermann, A. L. Fauchere, and G. Blatter. Nonlocality in mesoscopic josephson junctions with strip geometry. *Physical Review B*, 59(14):R9027, 1999.